INFORMATION TO USERS

This manuscript has been reproduced from the microfilm master. UMI films the text directly from the original or copy submitted. Thus, some thesis and dissertation copies are in typewriter face, while others may be from any type of computer printer.

The quality of this reproduction is dependent upon the quality of the copy submitted. Broken or indistinct print, colored or poor quality illustrations and photographs, print bleedthrough, substandard margins, and improper alignment can adversely affect reproduction.

In the unlikely event that the author did not send UMI a complete manuscript and there are missing pages, these will be noted. Also, if unauthorized copyright material had to be removed, a note will indicate the deletion.

Oversize materials (e.g., maps, drawings, charts) are reproduced by sectioning the original, beginning at the upper left-hand corner and continuing from left to right in equal sections with small overlaps. Each original is also photographed in one exposure and is included in reduced form at the back of the book.

Photographs included in the original manuscript have been reproduced xerographically in this copy. Higher quality 6" x 9" black and white photographic prints are available for any photographs or illustrations appearing in this copy for an additional charge. Contact UMI directly to order.

U·M·I

University Microfilms International
A Bell & Howell Information Company
300 North Zeeb Road, Ann Arbor, MI 48106-1346 USA
313/761-4700 800/521-0600

Order Number 9207057

Photoemission and XAS studies of solid oxygen and alkali metal systems

Chen, Jie, Ph.D.

City University of New York, 1991

U·M·I
300 N. Zeeb Rd.
Ann Arbor, MI 48106

PHOTOEMISSION AND XAS STUDIES OF SOLID OXYGEN AND ALKALI METAL SYSTEMS

by

JIE CHEN

A dissertation submitted to the Graduate Faculty in Physics in partial fulfillment of the requirements for the degree of Doctor of Philosophy, The City University of New York.

1991

This manuscript has been read and accepted for the Graduate Faculty in Physics in satisfaction of the dissertation requirement for the degree of Doctor of Philosophy.

2/26/91 — Date

Marten L. denBoer
Chair of Examining Committee

2/26/91 — Date

Joseph Krieger
Executive Officer

Myron Strongin

Ying-Chih Chen

Louis J. Massa

Leonard O. Roellig

Supervisory Committee

The City University of New York

Abstract

PHOTOEMISSION AND XAS STUDIES OF SOLID OXYGEN AND ALKALI METAL SYSTEMS

by

Jie Chen

Advisor: Prof. Marten L. denBoer and Dr. Myron Strongin

Solid oxygen and its interaction with alkali metals have been studied using x-ray absorption spectroscopy (XAS) and photoelectron spectroscopy (PES). The Oxygen K-edge NEXAFS spectrum of solid oxygen shows three main features, and they are assigned to the π^*, σ^* resonance, and Rydberg transitions, respectively. This assignment is supported by the theoretical calculation and high resolution NEXAFS measurements. Compared with the gas phase spectrum, the Rydberg states shift about 1.5 eV to a higher photon energy, which is due to the increase of dielectric constant in the solid. The Auger spectra of both the ionized and excited molecules in solid O_2 shift to a higher kinetic energy relative to the gas phase spectra. The shifts are 10 and 2 eV, respectively. These shifts are explained in terms of solid state final state screening effects. PES studies of the interaction between solid oxygen and alkali metals show that three different oxidation states can coexist at 35 K. Assignments of these features in both the O 1s core level and valence band spectra have been made for O_2^-, O_2^{2-}, and O^{2-} species, which correspond to the formation of superoxide, peroxide, and oxide, respectively. The Cs 3d and the O 1s cross-section ratio obtained from

experimental spectra and this assignment quantitatively agrees with the theoretical value.

We also studied LiO_2, KO_2, and CsO_2 superoxides using NEXAFS and EXAFS measurements. Compared with the solid O_2 NEXAFS spectrum, both the π^* and σ^* resonances in the NEXAFS spectra of all three alkali metal superoxides shift to a lower photon energy due to the transfer of electron to the molecular oxygen. The intensity ratio of these two peaks changes from about 2:1 in solid O_2 to a smaller value in the superoxides because of increased occupancy of the π^* level. The O-O bond length in superoxide deduced from the position of σ^* resonance, agrees well with the previous reported O-O distance in NaO_2 and KO_2. Both the O-O and O-Cs distances obtained from the EXAFS study on cesium superoxide (CsO_2) are in good agreement with previous x-ray diffraction measurements on NaO_2 and KO_2.

ACKNOWLEDGEMENTS

In my graduate career there are many people who have made this experience one in which I will remember forever, and to those people I express my gratitude.

First, I would like to thank Prof. Marten L. denBoer, my thesis advisor and Dr. Myron Strongin, my supervisor. They suggested this project and provided support, help, encouragement, and many ideas throughout the past four years. Most of this work was done at the National Synchrotron Light Source (NSLS) at Brookhaven National Laboratory (BNL). Much help was given to me by the staff in the Physics Department and the NSLS at BNL.

I feel fortunate to have had the opportunity to collaborate with Shenli Qiu and Chyanlong Lin, and Mark Ruckman who are great physicists and who gave me their time and expertise. They were there during a large fraction of late nights giving me much help. I cannot thank them enough for their help. Of course I cannot forget Fran Loeb for his excellent technical support and his friendship.

Special thanks to my parents, Xiuying Wang and Taipeng Chen, my sisters Yan Chen and Li Wang, and my brother Hong Chen for their continuing encouragement and support.

This work was supported in part by U.S. Department of Energy under contract No. DE-AC02-76CH00016.

Table of Contents

List of Abbreviations

AES	Auger Electron Spectroscopy
CMA	Cylindrical Mirror Analyzer
EELS	Electron Energy Loss Spectroscopy
EXAFS	Extended X-ray Absorption Fine Structure
HA	Hemispherical Analyzer
LEED	Low Energy Electron Diffraction
NEXAFS	Near-edge Extended X-ray Absorption Fine Structure
PES	Photoelectron Spectroscopy
PGM	Plane Grating Monochromator
SEXAFS	Surface Extended X-ray Absorption Fine Structure
SR	Synchrotron Radiation
TEY	Total Electron Yield
TGM	Toroidal Grating Monochromator
UHV	Ultra High Vacuum
UPS	Ultraviolet Photoelectron Spectroscopy
XANES	X-ray Absorption Near Edge Structure
XAS	X-ray Absorption Spectroscopy
XPS	X-ray Photoelectron Spectroscopy

List of Tables

List of Figures

Chapter 1. Introduction

1.1. Objective

The purpose of this thesis is to extend our knowledge of solid oxygen and alkali metal systems. By combining various surface sensitive techniques to study the solid oxygen-alkali metal systems and some simple molecular solids, such as O_2, and N_2, we hope to obtain a better understanding of the electronic configuration, oxidation states, ligand field, local geometry, and chemical properties of physisorbed and chemisorbed molecules on metal surfaces at low temperatures. However, to solve these problems completely would require much more experimental and theoretical work. Our present attempt is to use synchrotron radiation (SR) and surface sensitive spectroscopic techniques to systematically study the oxidation process of alkali metals at low temperatures. These simple model systems will contribute to a better understanding of the metal oxidation process for more complex systems.

1.2. Motivation

The investigation of alkali metal and oxygen adsorption is motivated by both technological applications and fundamental scientific interest. Technically, alkali metal oxides can be used as low work function materials in photocathodes. The presence of oxygen, either coadsorbed with alkali or bound in oxide form, is known to accentuate the effect of the alkali metal. The work function of the cesium oxide Cs_2O is considerably lower than that of pure Cs,[1] a fact which plays a role in the activation of photocathodes. Alkali metal oxides are of fundamental interest because of their unique ability to incorporate oxygen in a variety of modifications, *i.e.*, O^{2-}, O_2^{2-}, O_2^-, and O_3^- in the monoxides, the

peroxides, the superoxides, and the ozonide, respectively.[2] In addition, the alkali metal conduction band extends only about 2 eV below the Fermi level, whereas the shallowest core levels appear 12 - 30 eV below E_F. Consequently the oxygen valence states are not obscured in photoemission by overlapping metal features, so that the details of the electronic properties of the oxygen molecule in different charge states can be studied. Oxygen-alkali metal systems provide a unique opportunity for exploring the electronic structure of a series of ionic oxygen species. Moreover, varying the atomic size of alkali metal by substituting various alkali metals does not change the essential nature of the associated chemistry and provides insight into the effect of the ligand field and the Madelung potential on the oxygen valence orbitals.

1.3. Historical Review

Considerable attention has been paid throughout the history of surface science to the oxidation properties of simple metals, *e.g.*, alkali metals that are well described by the free-electron model. In 1969, Smith and Spicer measured energy distribution curves (EDC) of Na and K, and successfully interpreted their data in terms of the three-step model of the photoemission process.[3] Among alkali metal-oxygen systems, the cesium-oxygen system is particularly interesting from the technological point of view, since oxidized thin films of Cs have very low work functions and are therefore used as photocathodes. The photoemission study found that the work function of cesium oxide is 0.7 eV,[4] which is believed to be the lowest work function material known. The cesium-oxygen system has a very complex structural phase diagram with an unusually large number of different structural forms.[5] In 1971, Simon studied the structure of the cesium suboxides and proposed a structural model for $Cs_{11}O_3$.[6] Since then, the electronic properties of the cesium-oxygen system have been

intensively investigated by photoelectron spectroscopy.[7,8] Related systems, such as rubidium-oxygen,[9] potassium-oxygen,[10] sodium-oxygen,[11] and lithium-oxygen[12] systems have also been explored. In earlier room temperature studies, two different phases of oxidation of Cs, Rb, and K were observed, which were interpreted as atomic oxygen incorporated into the top metal layer and the formation of a metal-oxygen surface molecular compound. On the other hand, low temperature (liquid N_2) studies have shown three different oxidation states. In the potassium-oxygen system,[10] these three states were characterized by three O 1s peaks at 528.2, 531.9 and 534.6 eV binding energy, respectively. Recently, three different states of oxygen were found in the photoemission and metastable deexcitation spectroscopy (MDS) studies of the cesium-oxygen system,[13] which were identified as O^{2-}, O_2^{2-} and O_2^-. Most recently, both the occupied and unoccupied electronic levels of NaO_2 and KO_2 have been probed by photoemission spectroscopy (PES), inverse photoemission spectroscopy (IPE), x-ray absorption spectroscopy (XAS), and electron energy loss spectroscopy (EELS).[14,15] An O-O bond length of 1.35 Å was deduced for NaO_2 and KO_2.[14] However, the binding energy of superoxide species in these studies was different from other UPS results obtained from the potassium-oxygen system.[16]

Despite these numerous studies, many questions are not completely answered. Are the observed different oxidation states formed simultaneously, or separately? How do these oxidation states change with temperature? What is the O-O bond length in the peroxide (O_2^{2-}) and superoxide (O_2^-) species? How do the unoccupied states of both oxygen and metal change during the oxidation process? In order to answer these questions, more research and better understanding of oxygen/alkali metal systems are needed.

Chapter 2. Experimental Techniques

2.1. Introduction

In order to understand solid oxygen and alkali metal systems, we have used various surface-sensitive techniques to study the electronic structure, physical structure, and chemical properties of these systems. The experimental program was carried out in two stages. First, the occupied electronic states and the chemical properties of the solid oxygen-alkali metal systems were probed by both synchrotron radiation photoemission and conventional x-ray photoemission at the U7B beam line at National Synchrotron Light Source (NSLS). Second, the unoccupied electronic states and the chemical bonding properties of molecular solids and solid oxygen-alkali metal systems were studied on the x-ray absorption spectroscopy (XAS) system at the NSLS U7A beam line.

The U7A and U7B beam lines at NSLS were designed for ultraviolet photoemission spectroscopy (UPS) and surface extended x-ray absorption fine structure (SEXAFS) experiments, respectively. The U7B plane grating monochromator (PGM) beam line has a optimal energy range from 30 to 150 eV (P3), with a resolving power ($E/\Delta E$) of about 400 and a beam flux of 5 X 10^{10} photon/(sec.Ampere). The U7A toroidal grating monochromator (TGM) beam line has a continuous energy range of 120 - 400 eV using the 400 l/mm grating, and 300 - 1000 eV using the 1000 l/mm grating. The resolving power of U7A is about 750, and the beam flux is 10^{11} photon/(sec.Ampere). The monochromator and the experimental chamber at the U7A TGM beam line is drawn in Fig. 1. The experimental apparatus includes a vacuum chamber with a base pressure of 1 X 10^{-10} Torr, and facilities for cooling a sample to below 20 K. The desired gas is introduced into the chamber through a doser. In the x-ray absorption spectroscopy (XAS) measurements, the

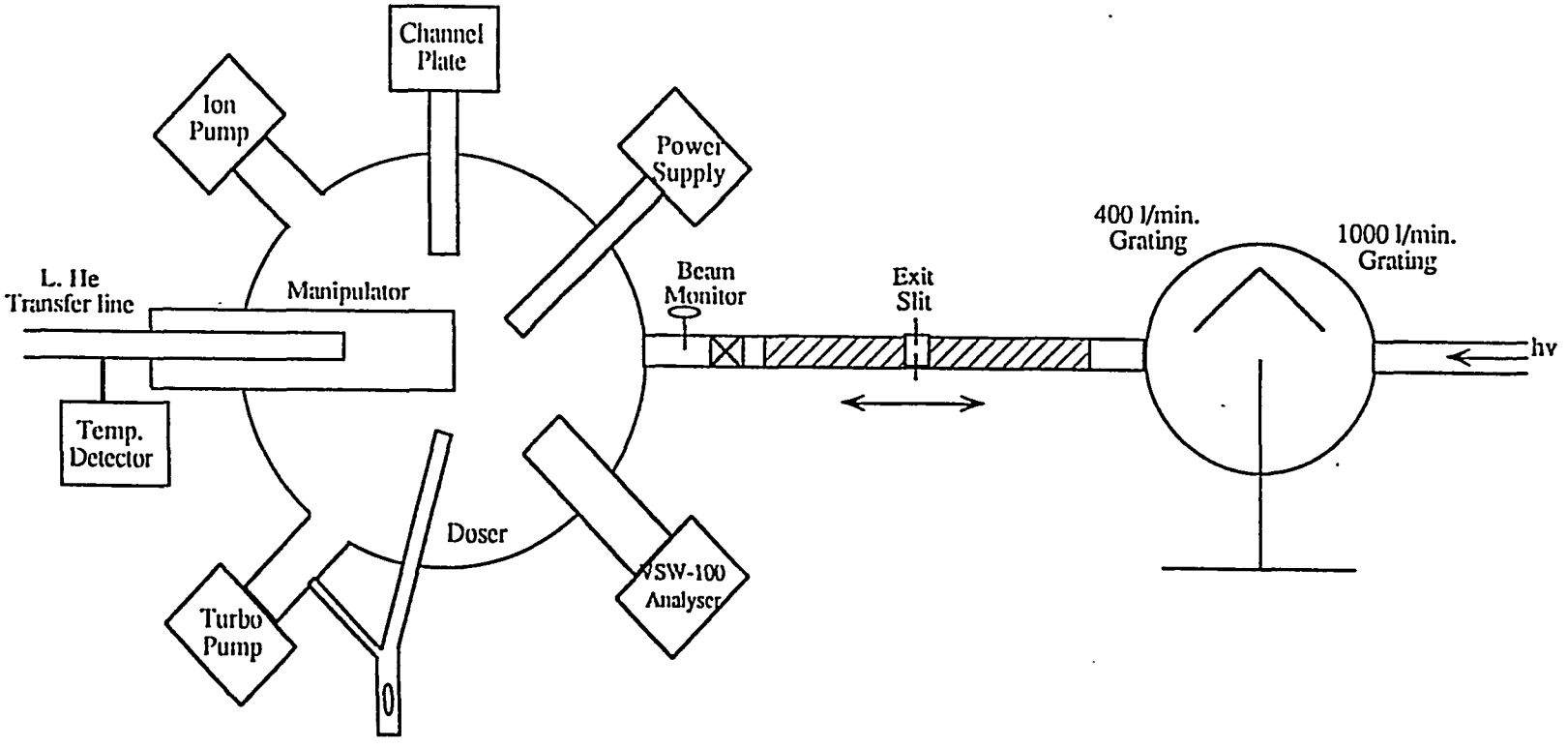

Figure 1. Schematic drawing of the U7A beam line experimental set-up used for low temperatures photoemission at NSLS.

	Sampling depth (Å)	Structure	Composition	Electronic Structure
Low Energy Electron Diffraction (LEED)	10	X		
Auger Electron Spectroscopy (AES)	10		X	X
Ultraviolet Photoelectron Spectroscopy (UPS)	5		X	X
X-ray Photoelectron Spectroscopy (XPS)	15		X	X
Extended X-ray Absorption Fine Structure (EXAFS)	100*	X	X	
Near-edge X-ray Absorption Fine Structure (NEXAFS)	100*	X	X	X

* For total electron yield measurement only.

Table 1. Summary of various spectroscopic techniques used for this thesis.

total electron yield (TEY) is recorded using a channeltron. In the photoelectron spectroscopy (PES) and Auger electron spectroscopy (AES) measurements, photoelectrons and Auger electrons are detected by a Vacuum Science Workshop (VSW) HA-100 hemispherical electron energy analyzer.

In the following sections I will discuss experimental equipment and sample preparation first, and then I will describe the physical principles of and the detailed experimental implementation of the primary surface sensitive techniques used for this thesis. For a summary of the various spectroscopic techniques used for low temperatures studies, see Table 1.

2.2. Experimental Equipment

The hardware required for our experiments consists of three major parts, (1) a source that produces a monochromatic beam of photons; (2) an electron detector, including detection electronics, a facility for energy selection of the emitted electrons; and (3) a vacuum chamber, which holds the sample.

2.2.1. Photon Energy Sources

The prime criteria in the selection of light sources for a experiment are the energy of the photons, the flux at the sample position, the energy band width of the beam, and compatibility with an ultrahigh vacuum system. If the source offers a continuous spectrum, a monochromator is required in order to provide a beam of defined photon energy.

In our photoemission investigation, we employed both a helium discharge lamp, a conventional x-ray source, and a synchrotron radiation light source. The helium gas discharge lamp gives rise to strong emission at photon energies of 21.2 eV (HeI) and 40.8 eV (HeII). The HeI spectral line is due to the 2p to 1s transition of the excited helium atoms and is always stronger than HeII. Besides using a suitable monochromator to separate the two lines, reducing the helium gas pressure in the discharge chamber can effectively increase the HeII spectral line intensity. Since the gas lamp has to be operated at a pressure of several Torr, a differential pump is required in order to install the lamp in an ultrahigh vacuum chamber. Differential pumping enables a pressure of several Torr to be maintained in the lamp while the photoelectron spectrometer is maintained at ultrahigh vacuum.

The conventional x-ray source used in our experiments is the Al K_α ($h\nu$ = 1487.6 eV) line, which is emitted by aluminum when Al anode is bombarded with high energy

electrons. Since no gas is used in the x-ray tube the whole instrument can be installed in an ultrahigh vacuum.

The most powerful photon source covering the whole range from the visible to the x-ray region is the synchrotron radiation light source. It is described in detail in the last section of this chapter.

2.2.2. Detector

We have used two different electron detectors in our experiments. The electron energy analyzer is for photoemission experiments and the channeltron is for x-ray absorption experiments.

A). Electron Energy Analyzers

The most popular analyzers used in photoemission spectroscopy are the cylindrical mirror analyzer (CMA) and the hemispherical analyzer (HA). The hemispherical analyzer (VSW HA100) we used was manufactured by VAS Scientific Instruments Ltd.[17] It consists of a 100 mm mean radius hemispherical electrostatic deflector that disperses the electrons across its exit focal plane according to their energies, and a long input lens that focuses electrons from the sample onto the entrance focal plane of the hemispheres. Normally, the relationship between the applied voltage and the energy of the transmitted electrons is linear and an energy distribution is obtained by sweeping the analyzer voltage.

The energy resolution of the analyzer is approximately given by

$$\Delta E = E_p\left(\frac{d}{2R_0} + \frac{\alpha^2}{4}\right), \qquad (2.2.1)$$

where E_P is the pass energy, d is the entrance slit width, R_0 is the mean radius of hemispheres, and α is the half angle of electrons entering the analyzer at the entrance slit. The analyzer we used is HA100, in which R_0 = 100 mm, d = 4 mm, $\alpha = 4^0$ and operated at E_p = 50 eV. The resolution ΔE calculated from equation 2.2.1 is about 1 eV. Comprehensive reviews of electrostatic analyzers and their performance are given by Sevier[18] and Roy.[19]

B). Channeltron

In our x-ray absorption spectroscopy (XAS) studies, XAS spectra were measured in the total electron yield (TEY) mode. The total electron yield can be recorded either by measuring sample-to-ground current or by using a channeltron. In our measurements, the typical sample-to-ground current was about 7 pA above the O K-edge. We found it difficult to exclude all sources of electrical interference from such low current measurements. In order to reject noise at such low current, we developed a new method to measure the total electron yield using a channeltron which is coupled to a lock-in electron amplifier. The sample mounting was designed so that the ac bias is applied only to the sample. Since the lock-in amplifier only detects the ac component of the photoelectron signal modulated at the reference frequency, the photoyield from the sample surroundings is not detected. This is very useful to eliminate the photoyield from scattered lights. A detailed description of this new technique is found in Ref. 20.

2.2.3. Vacuum System

In order to study the atomic properties of a surface, it is essential to keep a nearly constant composition of the surface during the experiment. This means that the arrival rate of reactive species from the surrounding gas should be low.

The simple kinetic theory of gases gives an expression for the arrival rate (Γ) of atoms or molecules from a gas of density n and with an average velocity v,

$$\Gamma = \frac{1}{4}nv = \frac{P}{\sqrt{2\pi kTm}} = 3.5\times10^{22}\frac{P}{\sqrt{mT}}, \qquad (2.2.2)$$

where P is the gas pressure, k is the Boltzmann constant, T is the temperature, and m is the mass of the molecule. For CO at room temperature,

$$\Gamma \approx 3.7\times10^{5}P\ (ML/s)\ . \qquad (2.2.3)$$

It is clear that reduction of incidental contamination to less than a few percent of a monolayer during an experimental time of 1 hour requires background pressures of 10^{-10} Torr or better.

In a vacuum chamber the volume gas is removed first, followed by outgassing and desorption of adsorbed gases from the inner walls and instrument surfaces, and last, permeation through the chamber wall. All these processes, except volume gas removal, are temperature dependent. At room temperature, it takes a very long time to reach the permeation limit. Thus high temperature baking is necessary to obtain ultrahigh vacuum in a reasonable pumping time. Thus the materials and seals used for construction of chamber walls and internal fixtures must be compatible with this thermal cycling. When our system has been completely assembled, we bake it at 150 °C for 24 hours to remove the surface gases, and 2 X 10^{-10} Torr pressure is achieved after cooling to room temperature. A detailed discussion of UHV techniques can be found in references 21 and 22.

An additional requirement for our experiments is exclusion of electrostatic and magnetic fields because many of the techniques we used involved low energy electrons which are easily deflected by weak electrostatic and magnetic fields. In our chamber, a μ metal shield has been used to screen the external magnetic field.

2.3. Sample Preparation

Many types of sample preparation techniques have been used in surface science studies depending on the nature of the material. In our work, samples have been prepared in the form of thin films in two different ways depending on the nature of the material: metal films and molecular solids.

We used thermal evaporation to prepare metal samples. The starting materials were heated directly by a W filament and the vapor was condensed onto a cooler substrate to yield a thin solid film. For some reactive materials with high vapor pressures below their melting points, such as alkali metals, commercial SAES getter sources were used. By resistive heating of the evaporant wire to high temperature before melting, a relatively constant and repeatable evaporation rate could be achieved. In order to grow clean thin films, the chamber pressure should be in the low 10^{-10} Torr range during evaporation and this requires thorough outgassing prior to evaporation.

Molecular solids were obtained by condensing high purity gases onto a cold substrate maintained below 20 K. At this temperature, where the vapor pressure is below 10^{-10} Torr for the molecules we studied, thick layers of molecular solids can be easily condensed.

Since superoxide species only can be formed in an oxygen-rich regime,[12] it is very difficult to make pure superoxide films. Normally, a huge solid O_2 feature accompanies a much smaller superoxide feature (Fig. 2b). In our experiments, we developed a nice way, namely, the "distillation" method, to prepare pure superoxide samples. Initially, solid O_2 was condensed on a layer of solid Kr. The Kr layer served as a buffer to prevent reaction between the molecular oxygen and the copper cold finger. Alkali metals were then evaporated onto the solid O_2 film. For dilute amounts of alkali metal a single electron was transferred to the O_2 molecule and superoxide was formed (Fig. 3b). Only small changes

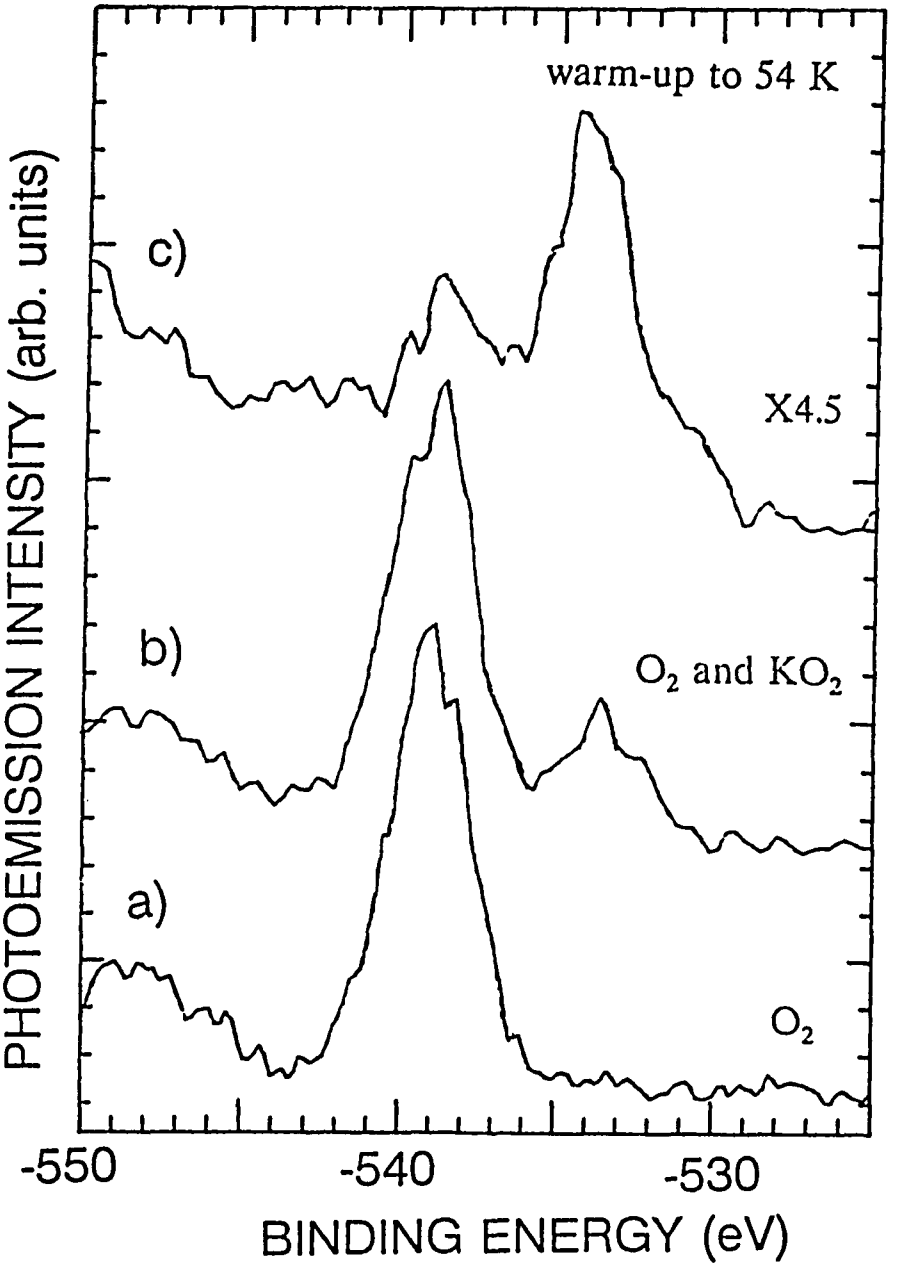

Figure 2. Oxygen 1s XPS spectra of (a) solid O_2 on a layer of solid Kr at 20 K, (b) K/O_2 at 20 K, (c) heating the sample to 54 K and than cooling it back to 20 K.

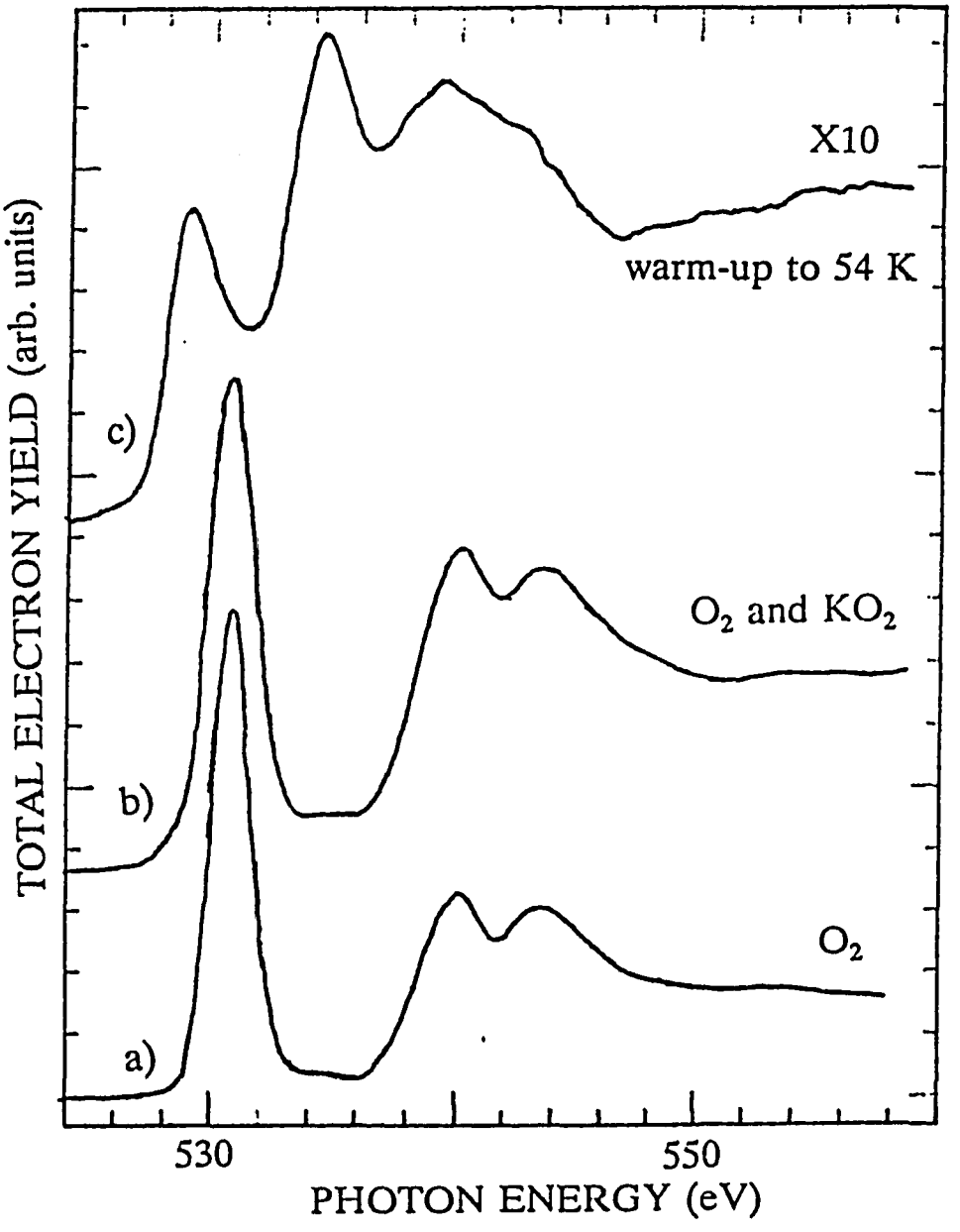

Figure 3. Oxygen K-edge NEXAFS spectra of (a) solid O_2 on a layer of solid Kr at 20 K, (b) K/O_2 at 20 K, (c) heating the sample to 54 K and than cooling it back to 20 K. Note the change of total yield intensity.

were seen in the solid O_2 NEXAFS spectrum as the sample still contains large amounts of molecular oxygen (Fig. 3b). By taking advantage of the melting temperature difference between Kr (T_M = 116 K) and O_2 (TM = 50 K), warming the sample to 54 K "distills" off the O_2 leaving the pure superoxide on the solid Kr (Figs. 3b and 3c). This method works very well if one can precisely control the sample temperature.

2.3.1. Sample Temperature Control

The temperature of the sample is a very important variable which affects the physical and chemical properties in a surface science study. The special requirements desired for surface study are not easily met by commercial units. The low temperature system used in our experiments is a modified Liquid Transfer Refrigeration System (Air Products LT-3B-110) manipulator,[23] in which the temperature of a sample can be varied from 10 K to 300 K in ultrahigh vacuum. Low temperature is achieved by the controlled transfer of liquid helium through a transfer line to a heat exchanger, which is coupled to the sample holder using copper blocks. A needle valve permits control of the flow rate and thus of the sample temperature. The system allows operation at given temperature range with excellent stability. The system also includes a UHV-compatible refrigerator which can be baked to 130 °C. The apparatus provides (1) rapid sample cooling to 20 K (~ half hour); (2) large movement (~ 5 cm) in three perpendicular directions (x,y,z); and (3) full 2 π polar rotation.

2.3.2. Adsorbate Thickness Measurements

It is always difficult to measure the amount of adsorbates accurately. At the early stages of adsorption, the adsorbate atoms may form three-dimensional clusters on the substrate surface. Even for metal overlayers, the thin film surface may not be perfectly

smooth. However, by systematic study and calibration with several surface-sensitive techniques, one can obtain a relatively accurate adsorbate thickness.

For a nonreactive thin film without interdiffusion at the interface, either the attenuation of substrate peaks or the intensity of the overlayer peaks in the photoemission spectrum can be used to estimate the adsorbate thickness. Consider a overlayer with thickness d and electron mean free path λ. The photoelectron intensity can be written as

$$I_S = I_S^o e^{-\frac{d}{\lambda \sin\phi}} , \tag{2.3.1}$$

$$I_o = I_\infty (1 - e^{-\frac{d}{\lambda \sin\phi}}) , \tag{2.3.2}$$

where I_S^0 is the photoemission intensity from the clean substrate, I_∞ is that of a thick overlayer material, and ϕ is the photoelectron emission angle. Normally, the d value determined by the above equations is within a factor of two of the correct value. The major factor limiting the accuracy is the electron mean free path λ.

In gas adsorbate studies, the langmuir (L) unit is widely used for recording gas exposure. A langmuir (L) is defined as

$$1\ L = 10^{-6}\ (Torr)(\text{sec}) . \tag{2.3.3}$$

It should be noted that the recorded langmuir is not the adsorbate thickness because of the sticking coefficient. For a Cu (111) surface, 1 ML = 1.5 X10^{15} atoms/cm^2, 1 L exposure of CO at room temperature corresponds to 0.27 monolayer (ML) if the sticking coefficient is one.

Since the gas exposure in langmuir is measured by recording the pressure and time, one should pay special attention to the pressure reading, especially for a system with a doser. In our chamber, the doser is directly pointed at the sample surface and for

convenience the ion gauge is located some distance from the sample. In this arrangement, during gas exposure the pressure near the sample is about 15 times higher than the ion gauge measured.

2.4. Photoelectron Spectroscopy (PES)

2.4.1. Photoexcitation Process

An electron excited by electromagnetic radiation may escape from the solid if it has sufficient kinetic energy to overcome the work function barrier. This photoelectric effect was described by Einstein in 1905. If the sample is irradiated with monochromatic photons of frequency ν, the energetics of the process are defined by the Einstein relation

$$K.E. = h\nu - \phi - E_B , \tag{2.4.1}$$

where E_B is the binding energy below the Fermi level and ϕ is the work function of the sample.

Before the photoexcited electron reaches the surface it may suffer various kinds of scattering. Quasi-elastic scattering by phonons may affect the direction of the outgoing electron and reduce the electron energy by a few meV. The electron can lose a substantial amount of energy through the creation of electron-hole pairs or the production of collective excitations of the electron gas known as plasmons. The mean free path for inelastic scattering depends strongly on the electron energy. Electrons with kinetic energies in the range 10-1000 eV above the Fermi level are scattered very strongly in solids and to emerge must originate very close to the surface. This is why photoemission is a very surface sensitive probe.

For interpreting the available data, the three-step model has been widely used because of its simplicity and success.[3] This model divides the photoemission process into three distinct steps which are (1) optical excitation; (2) transport of the excited electron to the surface; and (3) transmission of the photoelectron through the surface. Despite the successful prediction of the location of some individual peaks, discrepancies began to appear when the three-step model was used to predict either the intensity or the shape of the

photoemission features.

The most common photoemission technique is the measurement of an energy distribution curve (EDC) of the photoemitted electrons at a fixed photon energy. Below 40 eV photon energy, the EDC is dominated by the joint density of initial and final states. Above this energy, the EDC reflects more closely the local density of states. The tunability of synchrotron radiation makes possible two other techniques, namely, constant final state spectroscopy (CFS) and constant initial state spectroscopy (CIS). In the CFS mode photoelectrons with a fixed kinetic energy are measured while the photon energy is scanned. Hence transitions to the same final state are probed. In the CIS mode both the incident photon energy and the spectrometer window energy (kinetic energy) are synchronously scanned to monitor emission from the same initial state. By using the CIS technique one is able to obtain information on how the cross-section of a particular initial state changes with the photon energy.

2.4.2. Theoretical and Practical Aspects

A). Photoionization Cross-Section

The cross-section for the photoemission process dominates the emission intensity in the photoemission process. According to a first principle theory of photoemission in a single-step model, the differential cross-section for the photoelectron emission is given by the golden rule expression:

$$\frac{d\sigma}{d\Omega} \propto \sum [<\Psi_f \mid P\cdot A + A\cdot P \mid \Psi_f>]^2 \; \delta(E_f - E_f - h\nu) \; , \qquad (2.4.2)$$

where the wave function Ψ_f describes the plane wave state with energy E_f of the outgoing photoelectron. A is the classical magnetic vector potential and P is the momentum operator. The δ-function states that the photoemission process conserves energy.

B). The Electron Mean Free Path

The mean free path for photons in solids is larger than the scattering length of excited electrons for all energies in the PES range, so the electron mean free path is the parameter that limits the escape depth of photoemitted electrons.

The processes that determine the mean inelastic free path of hot electrons are electron-electron and electron-impurity scattering. Electron-electron scattering may lead to pair excitation, a single particle scattering event, or plasmon emission (collective many-body excitation). Both of these processes are accompanied by a relatively large energy transfer, a few eV for pair excitation and on the order of 10 eV for plasmon excitation. Inelastic electrons and secondaries therefore will leave the sample with low energy.

The energy dependance of the electron mean free path is presented in Fig. 4, which shows that photoelectrons in the 20 - 200 eV range have free path lengths comparable to the lattice spacing (~ 5 Å), so up to 30% of the total number of electrons in the spectra are derived from the top layer of atoms. For photoelectron kinetic energies above 200 eV, the electron mean free path increases and the surface sensitivity decreases.

C). Relaxation and Chemical Shift

The energy balance formula for the photoemission process given in Eq. (2.4.1) is only valid for a single particle; this is Koopman's approximation, which assumes that all energy levels are "frozen" during the photoionization process. The simple Koopman model does not accurately describe the experimental data, mainly because relaxation effects are ignored. When the core hole is created by photoionization, the remaining negative charged

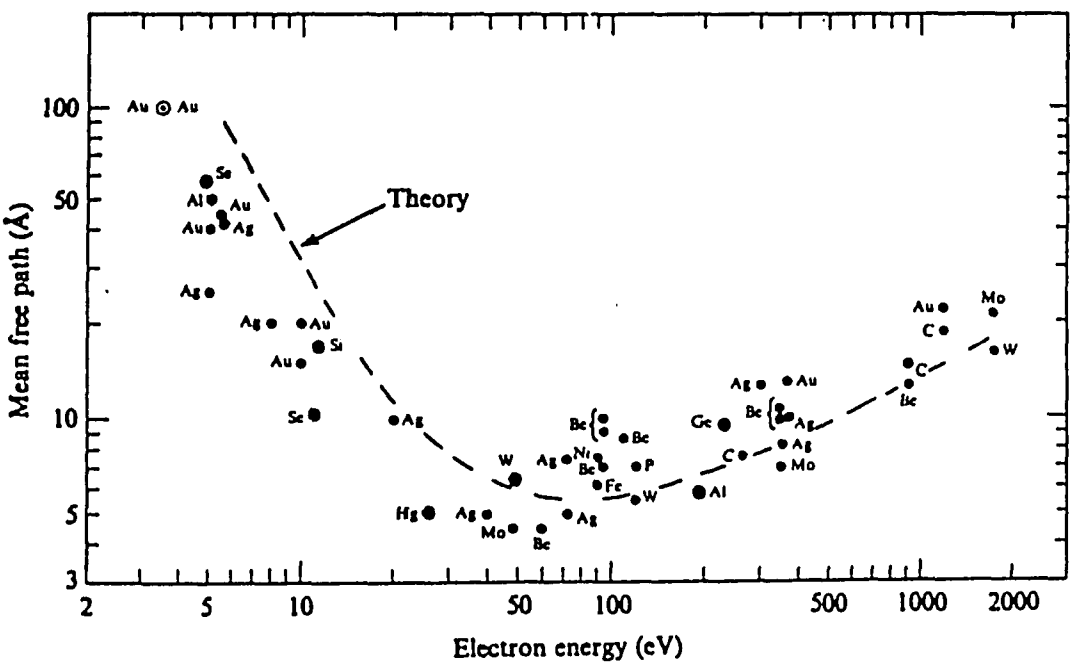

Figure 4. Energy dependance of electron mean free path length λ: experiment[24]; theory[25].

electrons will flow toward the hole in order to screen the suddenly appearing positive charge. The screening lowers the energy of the hole state left behind and therefore lowers the measured binding energy. This binding energy shift is commonly referred to as the relaxation energy E_R.[26] E_R can be partitioned into two components: the intra-atomic relaxation energy and the extra-atomic relaxation energy.

Intra-atomic relaxation or the rearrangement of the electrons on the atom is driven by the difference between the electron states of an N electron system and those of the (N - 1) electron system left behind after the photoemission event. If N is very large, these states will not differ very much, since the self consistent field does not change much when a single electron is removed. This is the case for solids with wide, overlapping bands; but in the case of localized energy levels, as found in small atoms, it is quite different. There the total number, N, of electrons is small enough that the self consistent field is sensitive to the removal of an electron. The orbitals of the remaining electrons adjust to the new field and the atom relaxes toward lower binding energies.

Extra-atomic relaxation refers to the charge flow from neighboring atoms, which occurs when the emitting atom is embedded in a polarizable medium. The local hole created by the photoemission process acts as a local positive charge and attracts screening electrons. The screening results in a lowering of the total energy of the system with the energy difference given to the emitted photoelectron.

Final state effects include intra-atomic relaxation and extra-atomic relaxation, which arises from many body relaxation and polarization effects, respectively. Once these effects are known, the observed kinetic energies of photoemitted electrons can be used to deduce information on the initial state of the system, an intrinsic property of the emitter. The energy of an electron in a tightly bound core state is determined by the attractive potential

of the nuclei and the repulsive Coulomb interaction with all the other electrons. Therefore, a change in the chemical environment of one atom will change the spatial distribution of the valence charge of that atom which implies that the exact value of the binding energy measured for a given element depends on the chemical environment of that element. For example, the 2p level of Al has a binding energy of 72.6 eV in Al metal and an energy of 75.3 eV in Al_2O_3.[27] This 2.7 eV shift is typical of the chemical shifts encountered when the oxidation state of an atom is changed by about one elementary charge. In practice, the chemical shift can be used to identify the chemical environment of an element by comparison with the binding energies of a set of reference compounds involving the same element. This fingerprinting technique is of considerable value in a variety of applications ranging from catalysis to environmental studies.

2.5. Auger Electron Spectroscopy

2.5.1. Introduction

When a hole is produced in a core subshell by an incident photon as in our case, or by an incident electron of sufficient energy, a decay or deexcitation of the system can occur via the emission of x-ray fluorescence or the emission of a secondary electron in a radiationless manner. These competing processes are dominated by the photon emission only when the initial core hole is deeper than about 10 keV. Indeed, this is the physical process used in a conventional laboratory x-ray generator. The alternative radiationless electron emission via the latter process is the Auger effect, named after its discoverer, Pierre Auger.[28]

Figure 5 shows a schematic of the two processes. In the case of photon emission we have

$$h\nu = E_A - E_B , \tag{2.5.1}$$

and in the case of Auger electron emission

$$K.E. = E_A - E_B - E_C . \tag{2.5.2}$$

In each case the emitted particle is characteristic of some combination of the atomic energy levels of the emitter and so forms the basis of a core level spectroscopy. However, core level fluorescence is of little interest in surface science because of the relatively long mean free path of a photon in solids. By contrast, an Auger electron has a short mean free path, making AES a surface sensitive probe.[29]

2.5.2. Deexcitation

As mentioned before, excited atoms created either by an incident photon, or by an

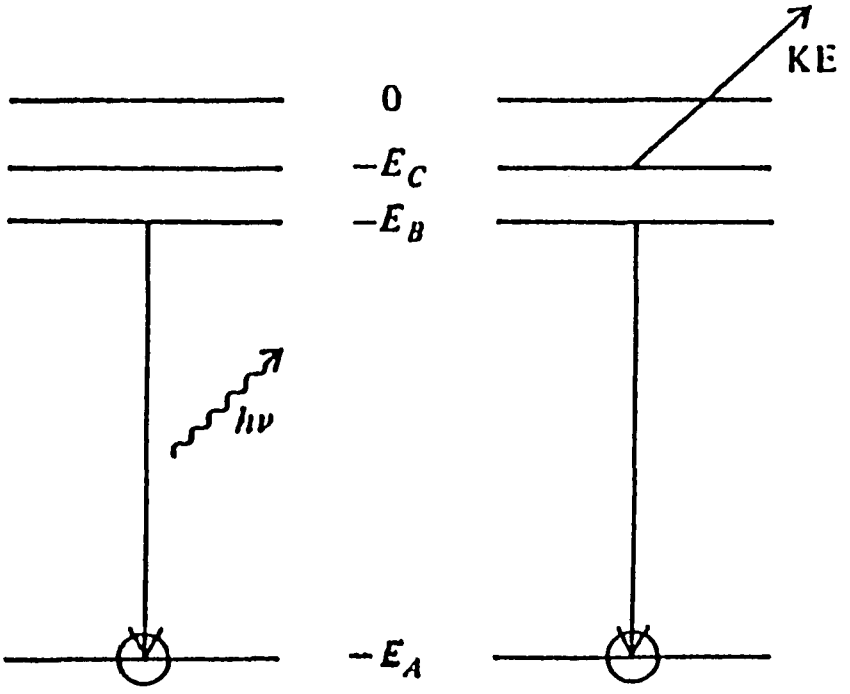

Figure 5. Energy level diagram showing the filling of a core hole in level A, giving rise to photon emission on the left, or Auger electron emission on the right. The levels are labelled with their binding energies.

incident electron, can relax to the ground state radiatively or, more commonly at the low binding energies of low-Z atoms, by electron emission. For ionized atoms, this is simply a conventional Auger electron process. For an excited neutral atom, an autoionization process occurs which is similar to an Auger decay, but modified by the presence of the promoted electron. This electron may participate in the Auger process or simply remain present as a "spectator." These two channels give rise to distinctly different final states of the atom, which may be distinguished experimentally by the different kinetic energies of the ejected electrons.

In order to determine the final states which may be reached, we first describe the excitation process. When the atom is ionized, the excitation may be written as

$$A + M \rightarrow M^{+}[c] + e \,, \tag{2.5.3}$$

where A represents the incident excitation, which may be an electron, photon, or other projectile, M represents the molecule of which the atom is part, $[c]$ denotes a core hole associated with the atom, and e the ejected core electron. Similarly, an excitation event is

$$A + M \rightarrow M[c](s) \,, \tag{2.5.4}$$

where (s) represents the electron promoted from the core level, but not ejected from the atom. The ions produced by process (2.5.3) may relax by a normal Auger process:

$$M^{+}[c] \rightarrow M^{++}[vv'] + e \,, \tag{2.5.5}$$

in which $[vv']$ represents the two valence holes that are produced and e the electron that carries off the energy. The excited neutral atoms produced in the process (2.5.4) may relax to fill the core hole in a transition involving the promoted electron,

$$M[c](s) \rightarrow M^{+}[v] + e \,, \tag{2.5.6}$$

which results in a singly ionized state of the atom. This may be compared with a direct valence photoemission (PES) process. Despite the expected coincidence in energy, the peak intensities for process (2.5.6) and the photoemission process are quite different due to the different matrix elements governing the two processes. The matrix element in process (2.5.6) is a Coulomb matrix element between the core hole excited state as the initial state and the valence hole plus ejected electrons as the final state, and therefore should be similar to the matrix element in the Auger process.

The excited neutral atoms produced in process (2.5.4) may also relax to fill the core hole, in a transition involving two other electrons, while the promoted electron is a passive spectator of the event:

$$M[c](s) \rightarrow M^{+}[vv'](s) + e \ . \qquad (2.5.7)$$

It should be noted that, although the ion resulting from process (2.5.7) also has two valence holes, and in that sense is similar to that produced in process (2.5.5) (normal Auger process), its energy, and hence the energy of the electron e, is different due to the presence of the spectator electron s.

2.6. X-ray Absorption Spectroscopy (XAS)

2.6.1. Introduction

When the energy of an x-ray photon is sufficient to excite a bound electron, the absorption coefficient μ shows a sudden increase. Atomic theory predicts a smooth decrease ($1/E^3$) in the absorption coefficient as the photon energy is increased above the edge. However, there are often some near-edge structures appearing either as sharp peaks in the absorption or as small bumps within 30 eV above the edge, and some oscillatory features superimposed on the smooth absorption coefficient which extend approximately from 30 to 1000 eV above the edge. Traditionally, the structure in the vicinity (~ 30 eV) of the edge is named the near-edge x-ray absorption fine structure (NEXAFS)[30] and the features further above the edge (30 - 1000 eV) are called the extended x-ray absorption fine structure (EXAFS).[31]

2.6.2. Basic Theory of EXAFS

Extended x-ray absorption fine structure (EXAFS) refers to the oscillations in the x-ray absorption coefficient spectrum as a function of photon energy in the energy range from about 30 eV to as far as 1000 eV above the absorption edge in an x-ray absorption spectrum. Since multiple scattering of the photoelectron is not important at this energy range,[32] a simple single scattering model of EXAFS has been formulated theoretically.[33,34]

In this simple single scattering model, EXAFS is a final state interference effect involving scattering of the outgoing photoelectron from the neighboring atoms (Fig. 5). In the absence of neighboring atoms, a photoelectron ejected by an x-ray photon will travel as an outgoing spherical wave with a wavelength $\lambda = 2\pi/k$, where

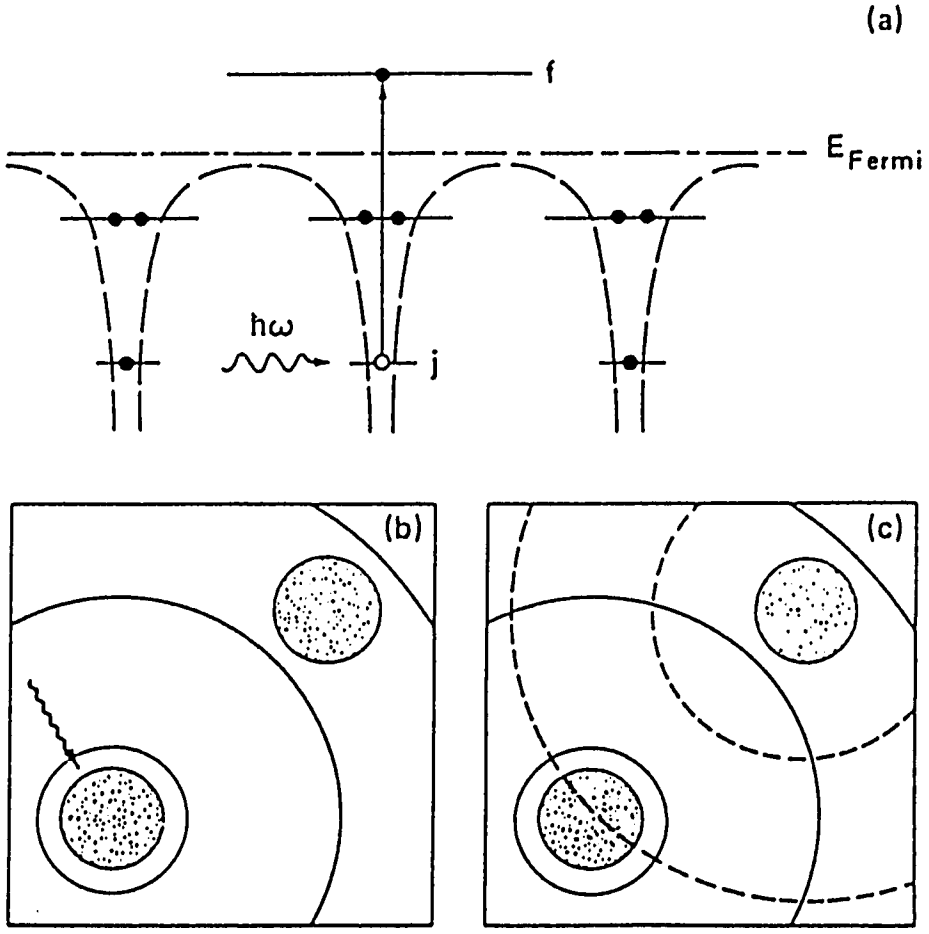

Figure 6. The origin of the extended x-ray absorption fine structure, or EXAFS. (a) An x-ray photon is absorbed by an atom through the excitation of an electron from a core state j to an unoccupied continuum state f. (b) The photoexcited electron waves propagate outward from the excited atom. (c) A scattered wave from a neighboring atom interferes with the outgoing wave at the excited atom, modulating the absorption cross section.

$$k = \sqrt{\frac{2m}{\hbar^2}(E - E_0)} \,. \tag{2.6.1}$$

Here E is the incident photon energy and E_0 is the energy threshold of the particular absorption edge involved. In the presence of neighboring atoms, this outgoing photoelectron can be backscattered from the neighboring atoms. This produces an incoming wave which can interfere either constructively or destructively with the outgoing wave near the origin, resulting in an oscillatory modulation of the absorption rate (μ). The amplitude and frequency of the sinusoidal modulation of μ as a function of E depends on the type (and bonding) of the neighboring atoms and their distances from the absorber.

If one uses Fermi's Golden Rule and the dipole approximation and only considers single scattering events, one can show

$$\chi(k) = \sum N_j \, S_i(k) \, F_j(k) \, e^{-2\sigma^2 k^2} \, e^{-2r_j/\lambda(k)} \, \frac{\sin(2kr_j + \phi_j(k))}{kr_j^2} \,, \tag{2.6.2}$$

where $\chi(k)$ is defined as

$$\chi(k) = \frac{\mu(k) - \mu_0(k)}{\mu_0(k)} \,. \tag{2.6.3}$$

$\mu(k)$ being the observed absorption for the material and $\mu_0(k)$ is the smooth, isolated atom-like absorption. Equation (2.6.2) describes the change in the absorption process due to the scattering of the photoelectron by N_j neighbors located at a mean distance r_j with a Gaussian distribution of standard deviation σ_j. $F_j(k)$ is the backscattering amplitude for the neighbor of type j. The total phase shift contains the geometric contribution $2k_j$ and a phase shift $\phi_j(k)$ due to the absorbing and backscattering atoms. $S_i(k)$ is the amplitude reduction factor due to many-body effects such as shake-up and shake-off processes at the central

atom.

By experimentally comparing the EXAFS spectrum of an unknown compound to a model compound, one can determine the coordination number N_j of the absorber, the bonding length r_j between the absorber and its neighboring atoms and the Debye-Waller factor σ_j which accounts for thermal vibrations and static disorder of the central atoms. Since each element has a characteristic x-ray absorption edge energy, the EXAFS at a particular edge reflects the average distribution of atoms around that particular kind of atom in the material. Thus EXAFS can be used to obtain information about the average near-neighbor coordination for each kind of atomic species in the material. Unlike x-ray diffraction, which is sensitive to long-range order, the EXAFS technique probes the local environment of the absorbing atom. Therefore, this technique can be applied to the study of the microscopic structure of disordered materials, such as polycrystals. The availability of intense and highly collimated x-ray beams from electron and positron storage rings has initiated the rapid development of x-ray absorption spectroscopy (XAS) and its widespread application in physics, chemistry, biology, and materials science.

Traditionally, the x-ray absorption spectrum is measured by recording the partial absorption cross section $\mu(k)$ for a specific core level excitation. In order to enhance the surface sensitivity, x-ray absorption spectrum can be carried out by monitoring the total electron yield (TEY).[35] Besides the TEY technique, several partial electron yield techniques, such as elastic Auger yield (EAY), partial Auger yield (PAY), and secondary electron yield (SEY) have also been employed for surface extended x-ray absorption fine structure (SEXAFS) studies. It has been shown theoretically[36] that the (S)EXAFS signals measured by these different electron-yield detection modes exhibit identical phase and thus will yield identical neighbor distances. The amplitudes derived from the spectra, however,

may be quite different since the inelastic and secondary photoelectron channel which contributes for some detection modes does not contain extended x-ray absorption fine structure (EXAFS) information.

2.6.3. Data Analysis for EXAFS

Data analysis in EXAFS is relatively complex. The EXAFS data is converted into $\chi(k)$ versus k, where $k = [(2m/h^2)(E-E_0)]^{1/2}$ is the wave vector of the outgoing electron, by normalizing the pre-edge background using the expression $\chi(E) = [\mu(E)-\mu_0(E)]/\mu_0(E)$. Then the Fourier transform technique is used to convert the fine structure oscillation spectrum $k^n\chi(k)$ in momentum (k) space into the radial distribution function $\rho_n(r)$ versus r in distance space.

A). Flux Normalization

The monochromator transmission function has a great influence on EXAFS spectra.[37] The C and O K-edge regions are most problematic because they exhibit the largest flux modulations due to the absorption of carbon and oxygen contamination on the optical surfaces of the beam line.[38] In our measurements, the beam flux was monitored by collecting the electron yield from a 90% transmission Au metal grid mounted in the incident beam well removed from the sample region. Figure 7a shows the absorption spectrum of solid NH_3 and O_2 recorded with the U7A TGM monochromator (1000 lines/mm grating) in the total electron yield (TEY) mode. The same spectrum after flux normalization is shown in Fig. 7c. The measured incident photon beam intensity is displayed in Fig. 7b.

B). Removal of Background Absorption

It is convenient to regard the total experimental absorption cross section as the sum

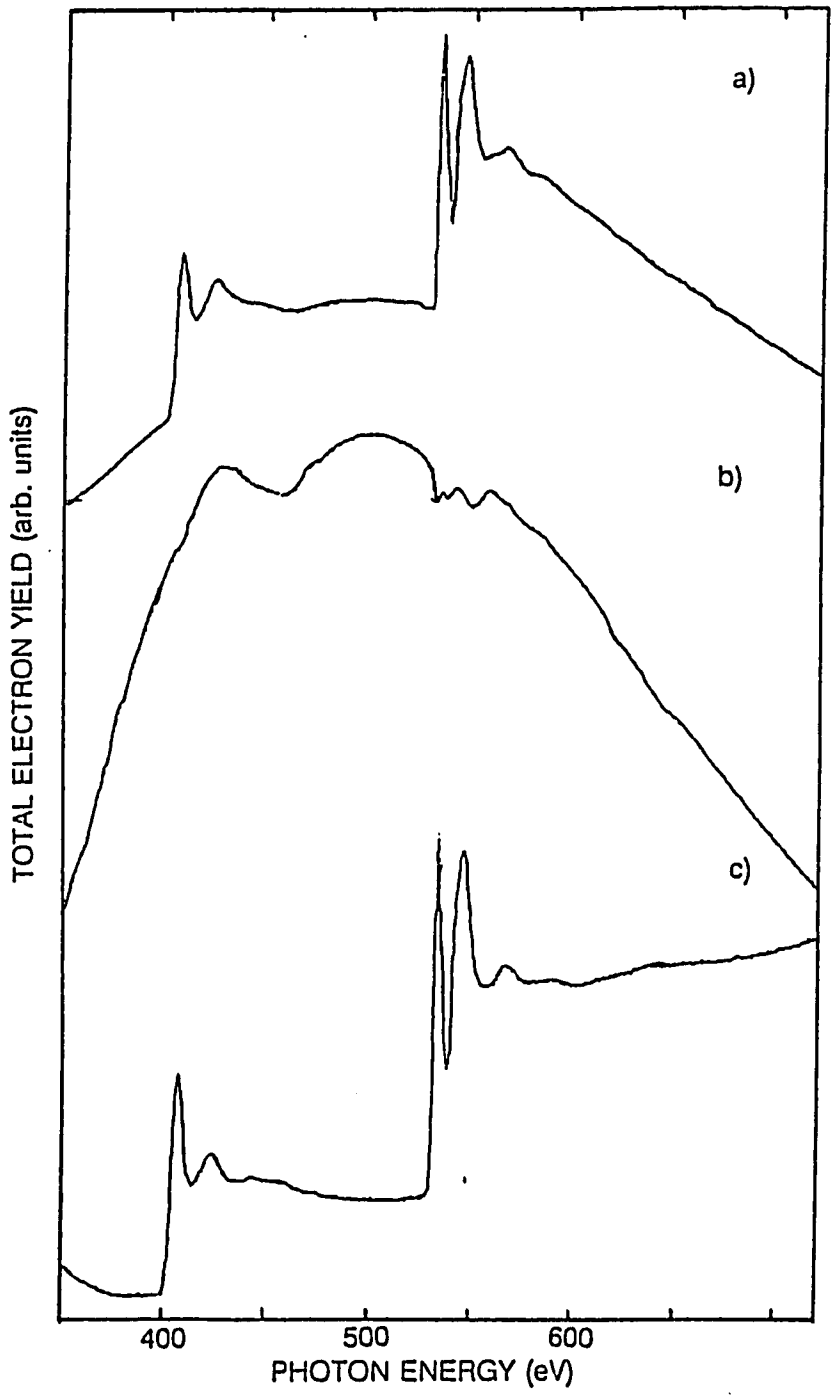

Figure 7. The absorption spectra of solid NH_3 and O_2 mixture recorded at 20 K with the U7A TGM monochromator (1000 lines/mm grating) by the total electron yield (TEY) mode. (a) before, and (c) after being normalized to the monochromator output (b).

of two distinct contributions: the K-shell absorption cross-section μ, which contains the EXAFS information, and a slowly varying background absorption μ_{bg}. This background absorption is due to the photoexcitation of all those electrons in the system which are less tightly bound than the K electrons of interest in the example. The first step in data reduction is often to fit a functional form to this quantity and to subtract the result from the measured spectrum. In our case, the pre-edge continuum background μ_{bg} was approximated by fitting the pre-edge part of the spectrum to a line. After subtracting this background, the spectrum was then normalized to the edge jump.

C). Extraction of EXAFS χ

The next step in data reduction is to find $\mu_0(k)$, where $k = (E - E_0)^{1/2}$, and thereby extract χ(k) using Eq. (2.6.3). In many cases it is possible to extract the needed μ_0 from a separate measurement of the x-ray absorption spectrum of atom species in a monatomic gas phase. There are, however, several complications: (a) It would be necessary to shift the photon energy to account for changes in the initial- and final-state energies; (b) the low energy portion of the continuum of final states in the solid is replaced with discrete bound states in the free atoms; and (c) it is necessary to rescale the overall strength of μ_0 to account for the differing number of absorbing atoms in the two experiments. Owing to these problems, the usual procedure for obtaining μ_0 is to extract it from the data set by fitting a slowly varying functional form to μ above the absorption edge. In our approach, μ_0 is approximated by fitting the high energy part of the spectrum by a polynomial function of k. E_0 is the threshold energy, determined by extrapolating the absorption from below and above, but excluding the contribution of the threshold spike.

D). Fourier Transform into r Space

In transforming the EXAFS into r space, there is a problem of minimizing the

undesirable effects of the limited data range available for the transform. The low-*k* cutoff is the more persistent problem in EXAFS analysis, arising from the necessity of avoiding the threshold spike. In the absence of a reliable method for removing that spike, the EXAFS data set must be terminated in the region of 2 - 3 $Å^{-1}$, where the EXAFS signal is usually strong. The large-*k* cutoff is much less of a problem, since it typically results from the EXAFS signal being reduced in strength to the noise level. In our data analysis, the Fourier transform was done over a limited *k* range from 2 to 8 $Å^{-1}$.

2.6.4. Introduction to NEXAFS

The NEXAFS region (near-edge x-ray absorption fine structure), which also is referred as XANES (x-ray absorption near-edge structure), extends approximately 30 eV on either side of the ionization edge. It is distinguished from the higher energy EXAFS regime by stronger scattering of the excited electron by the surrounding atoms. In this case two effects combine to enhance the contribution of multiple electron-atom scattering. Firstly, multiple scattering is important in the energy region near the edge, where the electron mean free path length is much longer than in the EXAFS region.[39] Secondly, electron-atom scattering becomes more isotropic at lower energies. This increases the intensity of large angle scattering which is necessary for multiple scattering. This low energy region is also complicated by the onset of shake up (off) transitions, which is inaccessible to the simplest single scattering EXAFS analysis. For all the above reasons, the features in the NEXAFS region are more difficult to analyze quantitatively. Therefore, in this energy range, it is more appropriate to regard the electron as being excited into a localized antibonding state of the system (Figure 8) rather than to describe it as an outgoing plane wave as described in EXAFS.

For low-Z atoms, K-edge NEXAFS spectra normally are dominated by resonance features. These resonances typically result from transitions to partially filled or empty states (bound state resonance) or to continuum states with a large scattering amplitude (shape resonance). Below the ionization edge, features in the absorption spectra called bound state resonances, are due to transitions of the core electron to a valence or a Rydberg orbital or an appropriate linear combination of them. Above the ionization edge, the NEXAFS features are due to transitions to quasi-bound molecular orbitals (also called shape or continuum resonances). Shape resonances result from the shape of the molecular potential, which temporarily traps the outgoing electron.

Since the shape resonance arises from a multiple scattering (MS) process along the internuclear axis, its energy position is sensitive to the internuclear distance.[40] Thus NEXAFS can reveal the presence of different types of bonds[41] and can serve to identify chemical reactions occurring on surfaces. A quantitative correlation between the energy of the resonances and bond lengths has been noted.[42] It has been found that there is a simple linear correlation between the σ^* resonance position and the intramolecular bond length for gas phase molecules.[43]

2.6.5. Polarization Dependence of the Near-edge Spectrum

Because of multiple scattering it is difficult to establish a clear model of NEXAFS theoretically, but the probability of photon-excited transitions from an initial state to the unoccupied molecular states is nevertheless governed by dipole selection rules:

$$P \propto |\langle \Psi_f | E \cdot P | \Psi_i \rangle|^2 . \qquad (2.6.4)$$

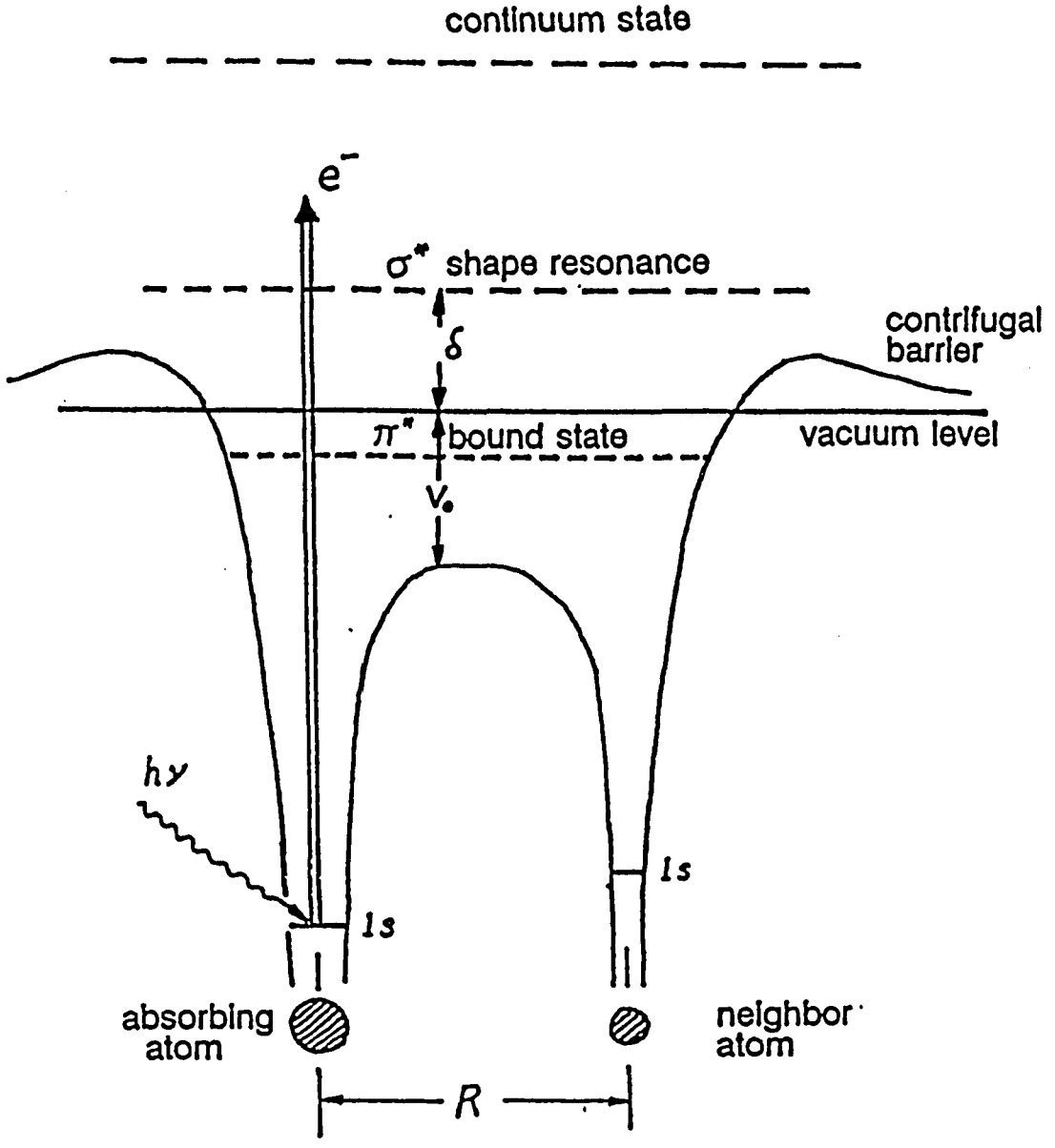

Figure 8. Schematic diagram of the π^* and σ^* resonances in a diatomic molecule with an intermolecular bond length R. The π^* resonance corresponds to a transition of a core electron to an empty or partially filled molecular orbital (bound state). The σ^* shape resonance involves a quasi-bound state in the continuum.

For a σ or π symmetry of the final state, the transition probability depends on the orientation of the electric field E of the photon with respect to the molecular axis.[44] It has been calculated that the transition probability from the initial state to a final state of σ symmetry is proportional to $\cos^2\theta$, where θ is the angle between the polarized E vector and the molecular axis, and the π symmetry state is proportional to $\sin^2\theta$ as:

$$N_\pi = \left(\frac{3N_0}{8\pi}\right) \sin^2\theta \ . \qquad (2.6.6)$$

$$N_\sigma = \left(\frac{3N_0}{4\pi}\right) \cos^2\theta \ , \qquad (2.6.5)$$

By taking advantage of the polarization of synchrotron radiation in the horizontal plane, the near-edge spectrum can be used to probe the orientation of the molecule relative to the surface by varying the angle between the E vector and the molecular axis.

2.7. Synchrotron Radiation Photoemission

2.7.1. Introduction

Synchrotron radiation is electromagnetic radiation emitted by charged particles moving in circular orbits with highly relativistic velocities. The outstanding properties of synchrotron radiation include:[45]

a) Continuous spectrum from the infrared to the x-ray region.

b) High intensity of photon flux.

c) Collimation of the emitted radiation in the instantaneous direction of flight of the emitted particles.

d) Linear polarization with electric vector parallel to the plane of the orbit.

e) Circular polarization above and below the plane of the orbit.

f) Time structure with pulse lengths down to 100 ps.

g) High vacuum environment.

2.6.2. Storage Rings

The basic element of the synchrotron radiation source is an electron storage ring which consists of an array of bending magnets that make the electron travel in circular arcs producing synchrotron radiation.[46] A variety of equipment is required to make a functional storage ring, such as quadrupole magnets to provide the focusing that keeps the electron beam transverse dimensions small, sextupole magnets that compensate for certain effects due to the energy spread in the electron beam, beam position monitors and steering coils used to correct deviations from the design orbit, and a computer control system. In order to store the electron beam for a longer time, the average pressure must be in the 10^{-9} Torr to minimize encounters between stored electrons and the residual gas. It is quite

VUV Storage Ring Parameters as of June 1987	
Parameters	VUV Storage Ring
Normal Operating Energy	0.750 GeV
Design Current (multibunch operation)	1.0 amp (1.1×10^{12} e^-)
Circumference	51.0 meters
Number of Beam Ports on Dipoles	17
Number of Insertion Devices	2
Maximum Length of Insertion Devices	~3.00 meters
$\lambda_c(E_c)$	25.3 Å (486 eV)
$B(\rho)$	1.28 Tesla (1.91 meters)
Electron Orbital Period	170.2 nanoseconds
Damping Times	$\tau_x \simeq \tau_y \simeq 17$ msec; $\tau_\epsilon \simeq 9$ msec
Touschek lifetime dependent on current/bunch and vertical emittance	
Lattice Structure (Chasman-Green)	Separated Function, Quad, Doublets
Number of Superperiods	4
Magnet Complement	8 Bending (1.5 meters each) 24 Quadrupole (0.3 meters each) 12 Sextupole (0.2 meters each)
Nominal Tunes ν_x, ν_y	3.12, 1.17
Momentum Compaction	0.023
R.F. Frequency	52.887 MHz
Radiated Power	14.7 kW/amp of Beam
R.F. Peak Voltage	100 kV
Design R.F. Power	50 kW
ν_s (Synchrotron Tune)	0.002
Natural Energy Spread (σ_ϵ/E)	4.5×10^{-4}
Natural Bunch Length (2σ)	7.6 cm ($I < 20$ mA)
Horizontal Damped Emittance (ϵ_x)	1.5×10^{-7} meter-radian
Vertical Damped Emittance (ϵ_y)	$\geq 2.8 \times 10^{-10}$ meter-radian (adjust.)
Power per Horizontal milliradian, 1A	2.3 Watts
Source Size: σ_h, σ_v	0.5 mm, > 0.06 mm

Source of Data: NSLS Parameters, January 1983, compiled by A. van Steenbergen; updated values provided by Gaetano Vignola (NSLS).

Table 2. VUV storage ring parameters at NSLS.

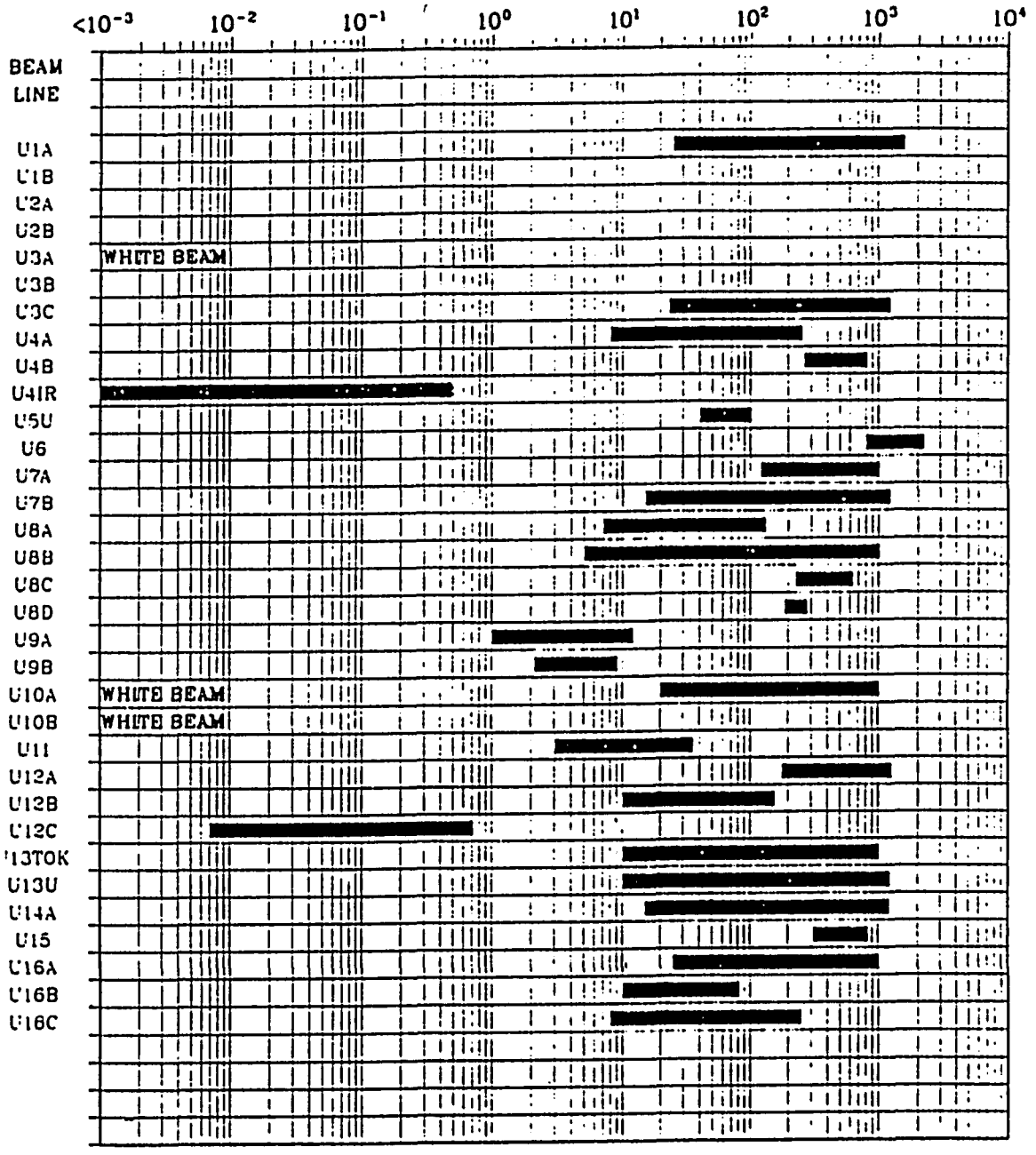

Figure 9. VUV beam line energy ranges (eV) at NSLS.

straightforward to achieve a base pressure in the 10^{-9} - 10^{-10} Torr range even in such a large system as a storage ring. However, in the presence of 100 kW or more of synchrotron radiation the gas desorption is large, and this determines the average pressure of the storage ring. To minimize gas desorption, special care needs to be taken in the fabrication, assembly, cleaning, baking, and installation of storage ring vacuum components.

In the National Synchrotron Light Source (NSLS), the electron current in the 750 MeV electron storage ring can reach one Ampere within several minutes, with a typical electron beam life time of several hours. Table 2. lists the parameters for the VUV storage ring at NSLS.

2.6.3. Monochromators

Most synchrotron radiation experiments need a particular wavelength selected from the continuum and to scan over a range of wavelengths, a suitable device has to be used to monochromatize the radiation and tune the energy. Thus a tunable monochromator becomes very important. For the hard x-ray region a crystal monochromator is used because the photon wave length is comparable with the crystal lattice parameter at this energy range. In the VUV region, many different types of photon energy band-pass filters are used for different photon energy regions. The energy ranges for all the beam lines at NSLS are shown in Figure 9. The monochromators installed in the U7B and U7A beam lines are the plane grating monochromator (PGM) and the toroidal grating monochromator (TGM), respectively. Since our experiments were performed at these beam lines, the following is a brief discussion of these two monochromators.

The general information and theoretical basis of the plane grating monochromator (PGM) for use with synchrotron radiation has been well reviewed and discussed by

Peterssen.[47] A standard PGM requires three reflections and the source is effectively the entrance slit so that its size and distance from the instrument determine the resolution. In principle, the wavelength range of a PGM is about 10 - 1000 Å ($h\upsilon \sim 10$ - 1000 eV) and its scan can be achieved by a simple mechanism. The U7B PGM is a grazing incidence plane grating monochromator which consists of two 600 groove/mm ion etched gratings, four focusing mirrors and one parabolic collimating mirror. The optimal energy range of the U7B PGM beam line is from 30 to 150 eV (P3). The resolving power of U7B is about 400 and the beam flux is 5×10^{10} photon/(sec.Ampere).

Since incident light undergoes three reflections in a PGM, both intensity and resolution are limited. Theoretically, using a concave grating, one can achieve collimation, dispersion, and focussing simultaneously in one element with one reflection. This desirable result is achieved by the toroidal grating monochromator (TGM). The toroidal grating relies on approximate focussing and is perhaps the simplest type of a grazing incidence monochromator. A typical TGM has the advantages of high flux, mechanical simplicity, and low cost. The toroidal grating monochromator installed in the U7A beam line consists of a toroidal focusing mirror, two gold coated gratings, one with 1000 groove/mm grating and one with 400 grooves/mm grating, and a movable exit slit. The U7A TGM beam line has a continuous energy range of 120 to 600 eV (400 line/mm grating) and 300 to 1200 eV (1000 line/mm grating) with a resolving power of about 750; the beam flux is 2×10^{11} photon/(sec.Amp.). Detailed information on the design and alignment of these monochromators can be found in references 48 and 49, respectively.

The monochromator output energy needs to be calibrated in order to accurately measure the energy position of absorption features. In our experiments, the photon energy of the monochromator was calibrated by comparing the solid O_2 spectrum with previously

reported data on gas phase O_2[50,51] and solid O_2.[52] We believe the absolute photon energy scale to be correct to better than 0.5 eV in the 350 - 700 eV energy range used here. This energy uncertainty is less than the energy resolution of the monochromator.53

Chapter 3. XAS and AES Studies of Molecular Solids

3.1. Introduction

The photoelectron spectra of both gas phase and solid phase molecules have been studied for many years.[54] Previous near-edge and extended x-ray absorption fine structure (NEXAFS and EXAFS),[55] and electron energy loss spectrum (EELS)[51] studies on these systems have revealed a wealth of spectroscopic detail in the region around the onset of inner-shell ionization. For low-Z atoms, these measurements focus on the K ($1s$) absorption edge, which is dominated by resonance features. NEXAFS studies of the K-edge absorption spectra of chemisorbed diatomic molecules have found absorption resonances similar to those found for gas phase molecules.[56] These studies show that the polarization dependence of the resonance intensity and their energy position relative to that observed in the gas phase can provide valuable information about the molecular orientation, the charge transfer upon chemisorption, and the intramolecular bond length.[57]

Solid N_2 and O_2 have been studied using photon stimulated ion desorption (PSID).[52] These studies show that the excitation spectra of molecular solids are reminiscent of that of the isolated molecule with small perturbations induced by the intermolecular bonding. Previous NEXAFS studies show that the Rydberg excitations observed in the K-shell excitation of water in the gas phase are severely perturbed and broadened in the solid due to the interaction between hydrogen atoms on different water molecules.[58] It is the goal of this study to elucidate these perturbations by presenting the NEXAFS spectra of molecular solids recorded by total electron yield (TEY) detection, and comparing these spectra with the NEXAFS spectra of the gas phase molecules. In addition, we will use the measured EXAFS signal of solid O_2 to determine the O-O bonding length. In order to

understand the changes in the NEXAFS spectra, we have also studied the various Auger electron spectra (AES) of solid O_2, which result from the electronic decay of the O 1s core hole from various excited states of solid O_2.

3.2. NEXAFS Study of Solid O_2 and N_2

3.2.1. Solid Oxygen

The ground electronic state of the oxygen molecule has the electronic configuration:

$$(1s\sigma_g)^2(1s\sigma_u)^2(2s\sigma_g)^2(2s\sigma_u)^2(2p\sigma_g)^2(2p\pi_u)^4(2p\pi_g)^2 \ .$$

Transitions involving the promotion of a 1s electron to $2p\pi_g$, $2p\sigma_u$ and *np* Rydberg orbitals are electric dipole allowed. In general, the promotion of a core electron to discrete levels results in a number of possible final states for a given electron configuration.[50]

The K-edge absorption spectrum of condensed molecular oxygen is shown in Fig. 10. The spectrum is qualitatively similar to previously reported photon stimulated ion desorption (PSID) and total electron yield (TEY) spectra on solid O_2.[52] Peak 1 and 2 at 530.8 and 539.7 eV are assigned to transitions from the 1s core level to the $2p\pi^*$ ($1\pi_g$) and $2p\sigma^*$ ($3\sigma_u$) orbital, respectively. The σ^* peak at 539.7 eV is 0.5 eV higher than that of O_2 in the gas phase spectrum.[51] The feature marked 3 at 543.4 eV is tentatively assigned to Rydberg transitions. It is much broader and more intense than would be expected for such transitions, suggesting a large mixing of the Rydberg and the $2p\sigma_u$ valence orbitals in this energy region. Relative to the gas phase O_2 spectrum,[51] this peak is shifted to about 1.5 eV higher photon energy. The assignment of peak 3 to a shape resonance, and its movement to higher energy, was recently used by Rosenberg *et al.*[52] to argue that the bonding length in the molecule is shorter in the solid phase due to condensation. This peak was also assigned to the spin exchange splitting of the σ^* resonance by Wurth *et al.*[59] The broad feature marked 4 at 564.1 eV, which was not observed in the gas phase spectrum, may be the first peak of the extended X-ray absorption fine structure (EXAFS) oscillations.

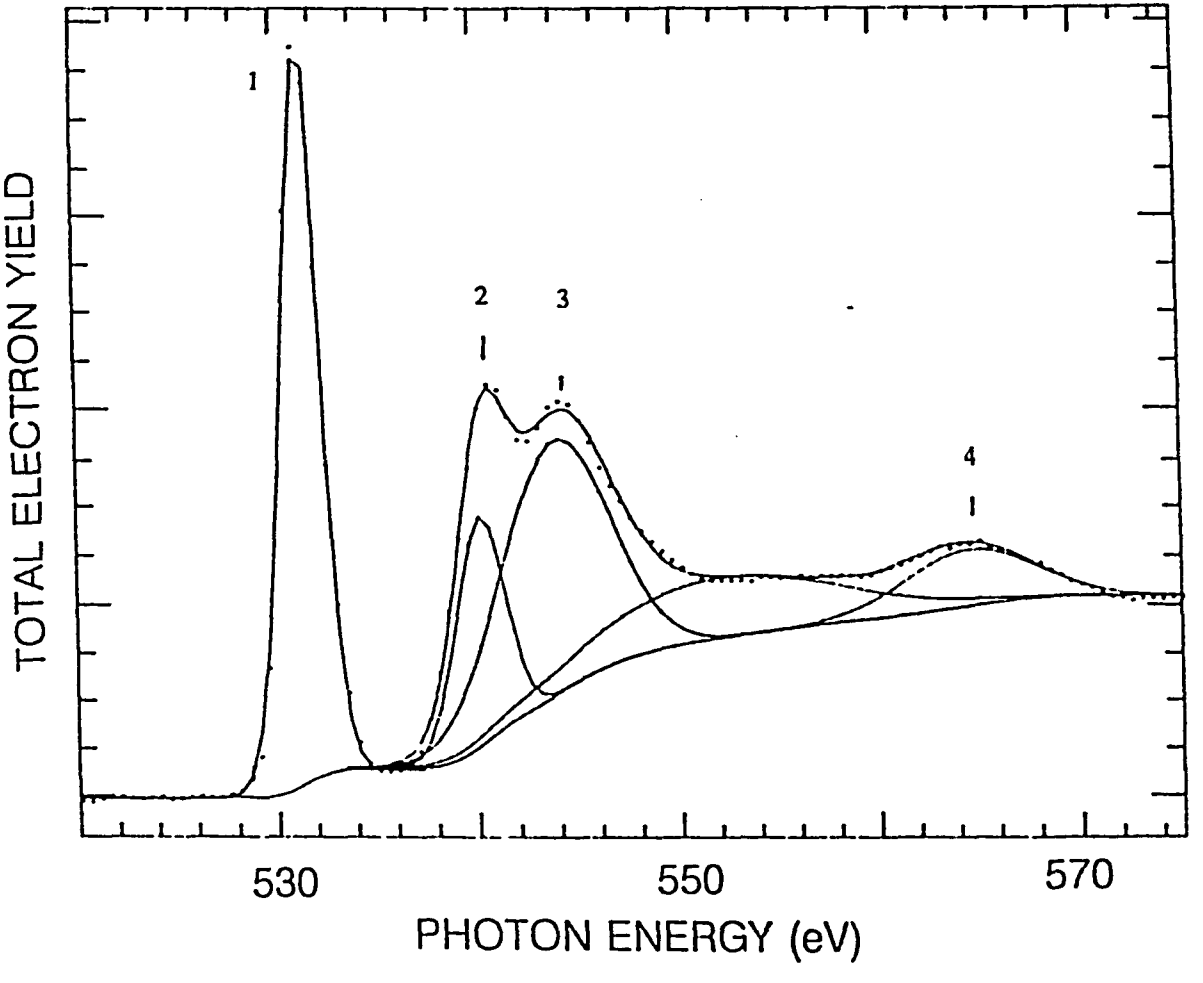

Figure 10. The O 1s near-edge x-ray absorption fine structure (NEXAFS) spectrum of solid oxygen. The energy was calibrated by lining-up with the gas phase O_2 π^* peak (Ref. 51).

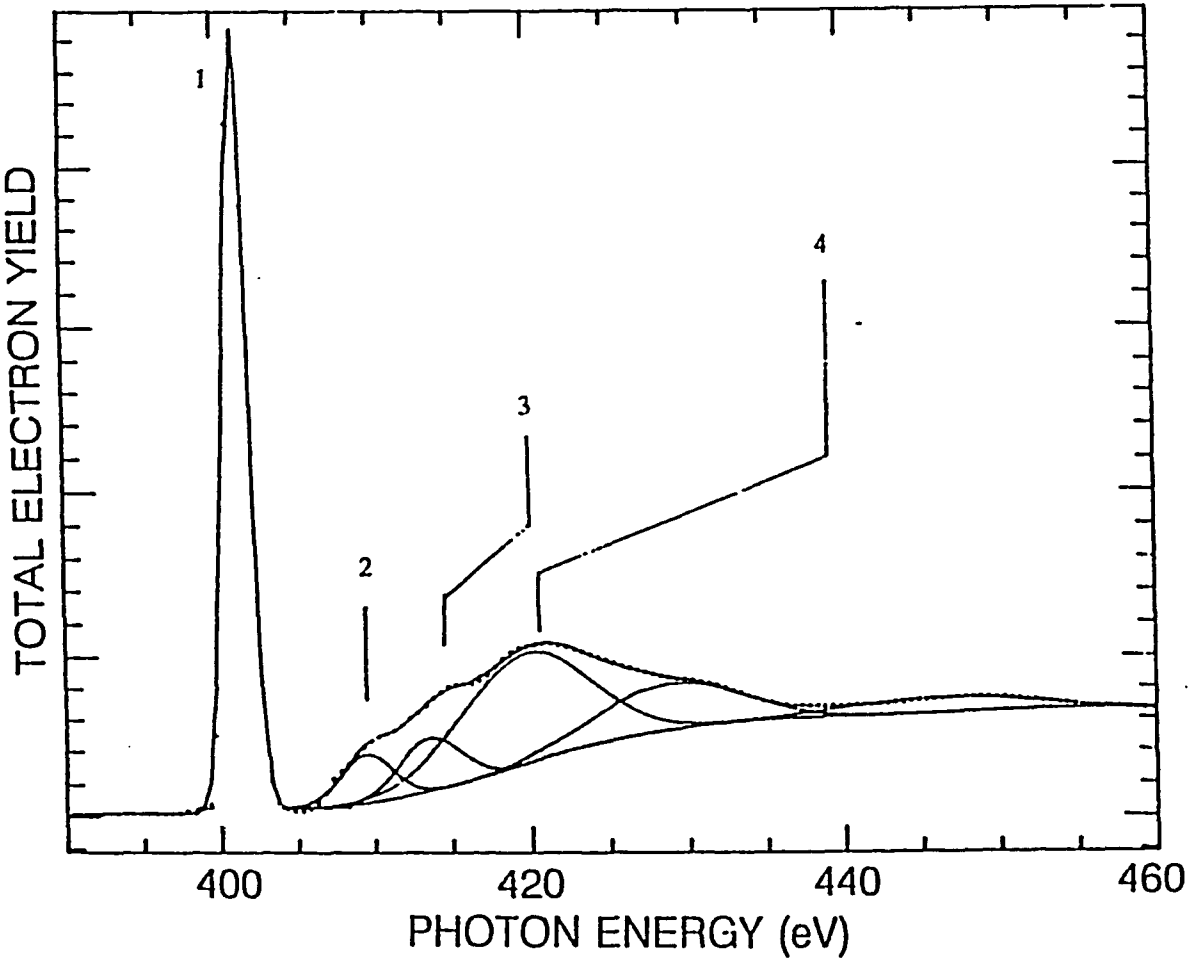

Figure 11. The N 1s near-edge x-ray absorption fine structure (NEXAFS) spectrum of solid nitrogen. The energy was calibrated by lining-up with the gas phase π^* peak (Ref. 51).

3.2.2. Solid Nitrogen

The ground electronic state of nitrogen has the electronic configuration:

$$(1s\sigma_g)^2(1s\sigma_u)^2(2s\sigma_g)^2(2s\sigma_u)^2(2p\sigma_g)^2(2p\pi_u)^4 \ .$$

Transitions involving the promotion of a 1s electron to $2p\pi_g$ and *np* Rydberg orbitals are electric dipole allowed.

Figure 11 shows the total electron yield NEXAFS spectrum of solid nitrogen. Similar to the published EELS spectrum of gas phase N_2 and TEY spectrum of solid N_2,[51,52] the measured NEXAFS spectrum is dominated by a sharp π^* resonance peak at 400.8 eV which is due to the transition from the N 1*s* core level into the unoccupied $1\pi_g$ molecular orbital. The features in the spectrum between 401 and 415 eV have been previously observed in the gas phase and have been assigned to various discrete excitations of the N 1s electrons.[60] This includes transitions into a Rydberg-type orbital (peak 2), the continuum threshold, and double excitations (peak 3). Peak 4 at 420.3 eV is due to a final state continuum shape resonance of σ_u symmetry, which arises from a multiple scattering process along the internuclear axis. Compared with the gas phase N_2 spectrum,[60] this peak is shifted about 1.5 eV to higher photon energy.

3.2.3. A Comparison between the Gas Phase and the Solid Phase Spectra

Comparing Fig. 10 and Fig. 11 with the previously reported electron energy loss spectra (EELS) of gas phase molecules,[51] it is evident that the spectra of the molecular solid closely resemble those of the gas phase molecule. This is, of course, expected as molecular solids are made up of individual molecular units bonded via a weak van der Waals force. However, there are some deviations from the gas phase spectra.

First, the π^* peak (marked 1) in the solid phase spectra is much broader than the

corresponding feature in the gas phase. The full width at half maximum (FWHM) of the π^* resonance peak in gas phase N_2 and O_2 is 0.85 and 1.5 eV, respectively, as measured in EELS.[51] More recently, the 1*s* absorption spectrum of molecular N_2 and O_2 has been measured using a very high resolution monochromator.[61] The π^* resonance peak in gas phase N_2 spectrum was resolved into at least eight vibrational levels; the FWHM of the 0→0 vibrational level ν_{00} was 132 meV. The combined FWHM of the π^* resonance peak was less than 0.6 eV; on the other hand, the measured FWHM of the π^* resonance in gas phase O_2 was about 1.5 eV, the same as the earlier EELS measurements.[51] This broadening in width was explained in terms of unresolved vibrational levels with frequency comparable to the O 1s core hole lifetime.[61] In our measurements, the observed FWHM of π^* resonance peak is 1.6 eV for solid N_2 and 2.0 eV for solid O_2. This is substantially larger than the monochromator resolution, which at $h\nu$ = 400 and 500 eV is 0.5 and 0.8 eV, respectively.[53] Thus the π^* peak is not resolution limited. Previous NEXAFS studies in the K-shell excitation of ice showed the same effects compared to the gas phase water molecules, and this broadening was explained in terms of the interaction between hydrogen atoms on the different water molecules.[57] Relative to the gas phase, the observed Rydberg excitations are also broadened in the solid and are shifted to higher energy. Similar broadening and shifts have also been observed in the photon stimulated ion desorption (PSID) spectra and the total electron yield (TEY) spectra of solid N_2, O_2, CO and NO.[52] As in the present case, this broadening is not due to experimental resolution; rather, these features are intrinsically wider, presumably due to intermolecular interactions in the solid and possibly the Franck-Condon effect.

Second, the energy position of the third peak is shifted: for both O_2 and N_2 the separation between the π^* and the third feature is 1.5 eV larger than in the gas phase. In

a previous study, the shift on solid O_2 was explained as a decrease in the intermolecular bond length.[52] However, x-ray diffraction studies did not show any change in spacing.[62] Also, physically it is hard to believe that the weak van der Waals force (roughly corresponding to 10 meV bonding energy) can change the length of the strong O-O bond (the bond energy is 2.5 eV)[63] significantly. Recent NEXAFS measurements on the O K-edge for physisorbed solid and oxygen bound in two different surface states on Pt(111) done by Wurth *et al.*[59] showed that the spacing of peak 2 and 3 changes in each case. They argue that peaks 2 and 3 are due to magnetic exchange splitting and the interaction of O_2 with a metal quenches this splitting. Their self-consistent-field $X\alpha$ multiple scattering calculation gives a value for the splitting of 1.2 eV, which is much smaller than the measured 2.5 eV separation in the gas phase spectrum. Based on this fact and the fact that the splitting changes from 2.5 eV in the gas phase to about 3.5 eV in the solid phase, Akimov *et al.*[64] rejected the conclusion that exchange is solely responsible for the splitting. They pointed out that, as one examines the molecular sequence N_2-NO-O_2, one notices the shape resonance shifts from the continuum region to the discrete region as the σ shape resonance crosses the ionization potential. Hence, they argue this somehow changes the nature of the features in the threshold region. It is believed that oxygen should have a large shape resonance near 540 eV, and its core level has an intense shakeup satellite about 10 eV from the primary 1s peak due to the shakeup from the $1\pi_g$ to the $3\sigma_u$.[65]

Most recently, Dunlap[66] did theoretical calculations of O_2. The calculations were performed using the X_α method previously used to compute the O_2 Auger spectrum.[67] The total energy was computed for different ionization states. For example, the O_2 1s ionization threshold for the $^4\Sigma$ final state is the difference between the energy of the triplet ground state and the energy of the configuration with a 1s electron with spin-up removed.

This can be repeated for final states where the 1s electron is put in the unoccupied π^* or σ^* orbitals. Note that this is the proper way of calculating an exchange splitting because such splitting are not additive as assumed in Ref. 59.

The O_2 molecule was calculated using O-O distance R = 1.21 Å. The calculated results show that the separation between the π^* resonance and the 1s ionization potential are 12.3 and 13.2 eV for the quartet and doublet final states, respectively. These numbers are in excellent agreement with the measured value of 12.3 and 13.4 eV by EELS[51] and XAS.[61] However, the σ^* resonance spin splitting obtained from the same calculation is only 0.5 eV (Fig. 12), which is much smaller than the observed 2.5 eV separation. This implies that peaks 2 and 3 are not due to exchange splitting; rather, this suggests that only peak 2 is the σ^* resonance. We believe peak 3 is due to unresolved Rydberg structures. This assignment is supported by the (previously mentioned) high resolution gas phase O_2 spectrum of Ma *et al.*, in which nine Rydberg peaks are clearly resolved in the peak 3 region.[61] The identification of peak 3 as an unresolved Rydberg series also provides a straight-forward means of explaining the disappearance of peak 3 when O_2 is absorbed on the Pt(111) surface. The interaction of O_2 with the metal atom suppresses the Rydberg transitions. Similar effect was observed in NO spectra by Roncin.[68]

As we suggested in a previous paper,[69] the peak shift in the solids is probably due to a solid state effect, namely a dielectric constant effect. Because molecules are highly polarizable in solid, condensed layers of molecules have a larger dielectric constant ($\epsilon > 1$) than in the gas phase ($\epsilon \approx 1$). Since the separation between the vacuum level and Rydberg states is inversely proportional to the dielectric constant ϵ, the large dielectric constant in the solid will tend to shift the Rydberg states closer to the vacuum level than in the gas phase. Another factor is the wave function overlap of molecular orbitals of adjacent

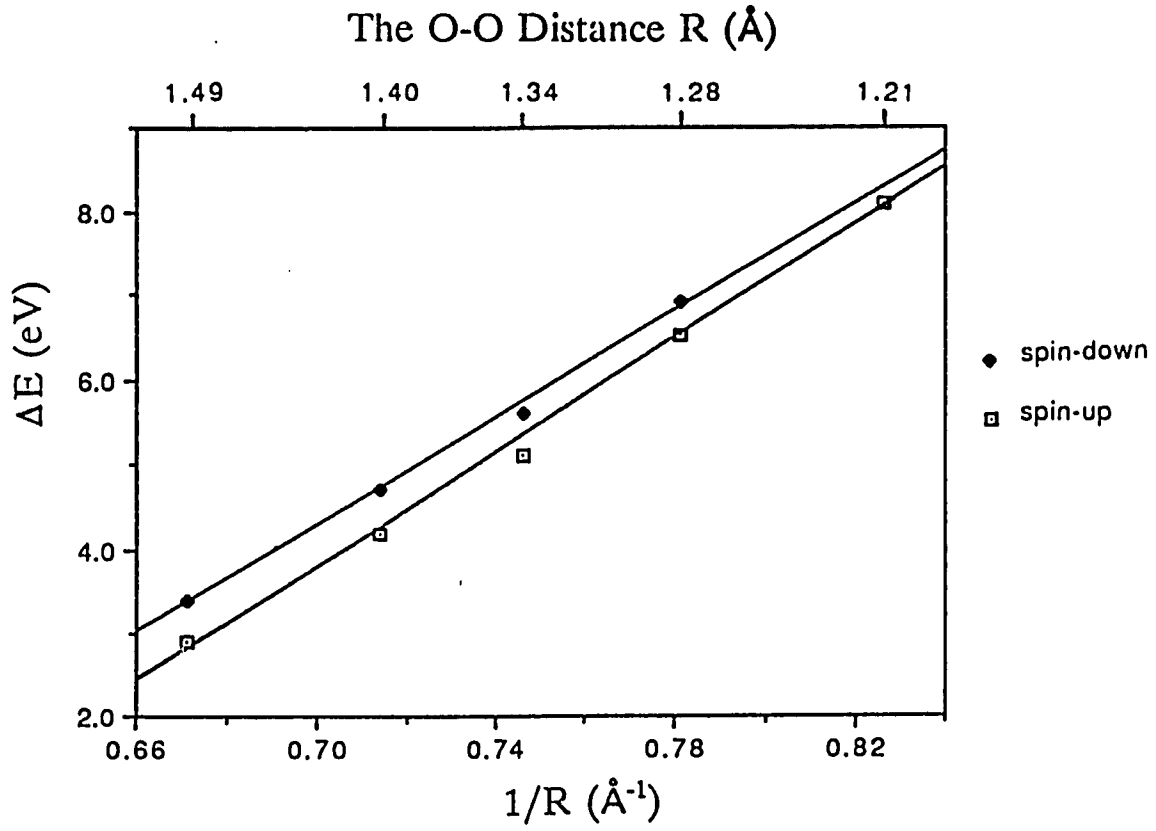

Figure 12. The correlation between the O-O bond length in the gas phase O_2 and the calculated energy separation of the π^* and σ^* resonances in the NEXAFS spectrum. Two sets of data correspond to exciting spin-up and spin-down 1s electron, respectively. The data is plotted as ΔE verses 1/R, where R is the O-O distance. (Ref. 68)

molecules in the solid state, which will tend to raise the energy. There is another effect which also can shift these peaks, namely intermolecular charge transfer between the molecules in the solid.[70] In the solid, some molecules can weakly couple into pairs, or dimers, which can produce different ionic states from the monomer when ionizing a molecule. The observed 1.5 eV shift is much larger than the energy of formation of the dimer (<300 meV)[71] so that the shift cannot be accounted for by this effect.

The energy position of peaks in NEXAFS spectra of solid O_2 and N_2, and their comparison with the gas phase molecules are summarized in Table 3.

In conclusion, we have measured the x-ray absorption spectra of condensed molecular oxygen and nitrogen. We found significant deviations from the gas phase spectra. In the solid O_2 case, compared with the gas phase spectrum, the Rydberg states shift about 1.5 eV to higher photon energy. We argue that this shift is due to an increase in the dielectric constant in the solid. This argument is also supported by recent high resolution NEXAFS measurement[61] and theoretical calculations.[66]

	O_2			N_2		
Peak	Solid(eV)	Gas(eV)	ΔE(eV)	Solid(eV)	Gas(eV)	ΔE(eV)
1	530.8	530.8	0	401.0	401.0	0
2	539.7	539.2	0.5	410.2	409.8	0.4
3	543.4	541.8	1.6	414.8	414.7	0.1
4	564.1			420.5	418.9	1.6

Table 3. Comparison of the energy position of peaks in NEXAFS spectra between solid and gas phase molecules. ΔE is the energy difference between the feature in the solid phase spectra and the corresponding feature in the gas phase spectra.

3.3. EXAFS Study of Solid O_2

As a powerful technique for the study of short-range order structure (local structure), EXAFS has been employed effectively to investigate amorphous materials, catalysts, and various types of materials of interest in solid state physics. But two factors have limited the application of EXAFS analysis to simple molecular systems.[72] First, the backscattering amplitude $F(k)$ in Eq. (2.6.2) decays rapidly with k when changing from a larger atomic number Z to a smaller Z.[73] Second, the frequency of the oscillatory modulation in the EXAFS spectrum is inversely proportional to the interatomic distance, and hence the shorter the bond length, the fewer the number of oscillations in a given energy range. These combined effects make it difficult to get good EXAFS spectra in simple molecular systems.

The total electron yield EXAFS spectrum at the O K-edge in solid O_2 is shown in Fig. 13a. In order to normalize the incident photon flux and the monochromator transmission function the ratio of the total electron yield to the incident photon flux is presented. The spectrum is qualitatively similar to the published total electron yield spectrum on gas phase O_2.[74] This is, of course, expected as molecular solids are made up of individual molecular units bonded via a weak van der Waals force. However, there are some deviations from the gas phase spectrum. The striking difference is that there is a relatively strong peak at about 565 eV photon energy in the solid O_2 spectrum, which is absent from the gas phase O_2 spectrum. We believe that this peak is an EXAFS feature, which is due to the presence of neighboring molecules.

After removing the background, the spectrum is then normalized to the edge jump and presented in Fig. 13b, where the smooth atomic absorption μ_0 is obtained by fitting the spectrum at high energy range with a polynomial function. The fine structure oscillations

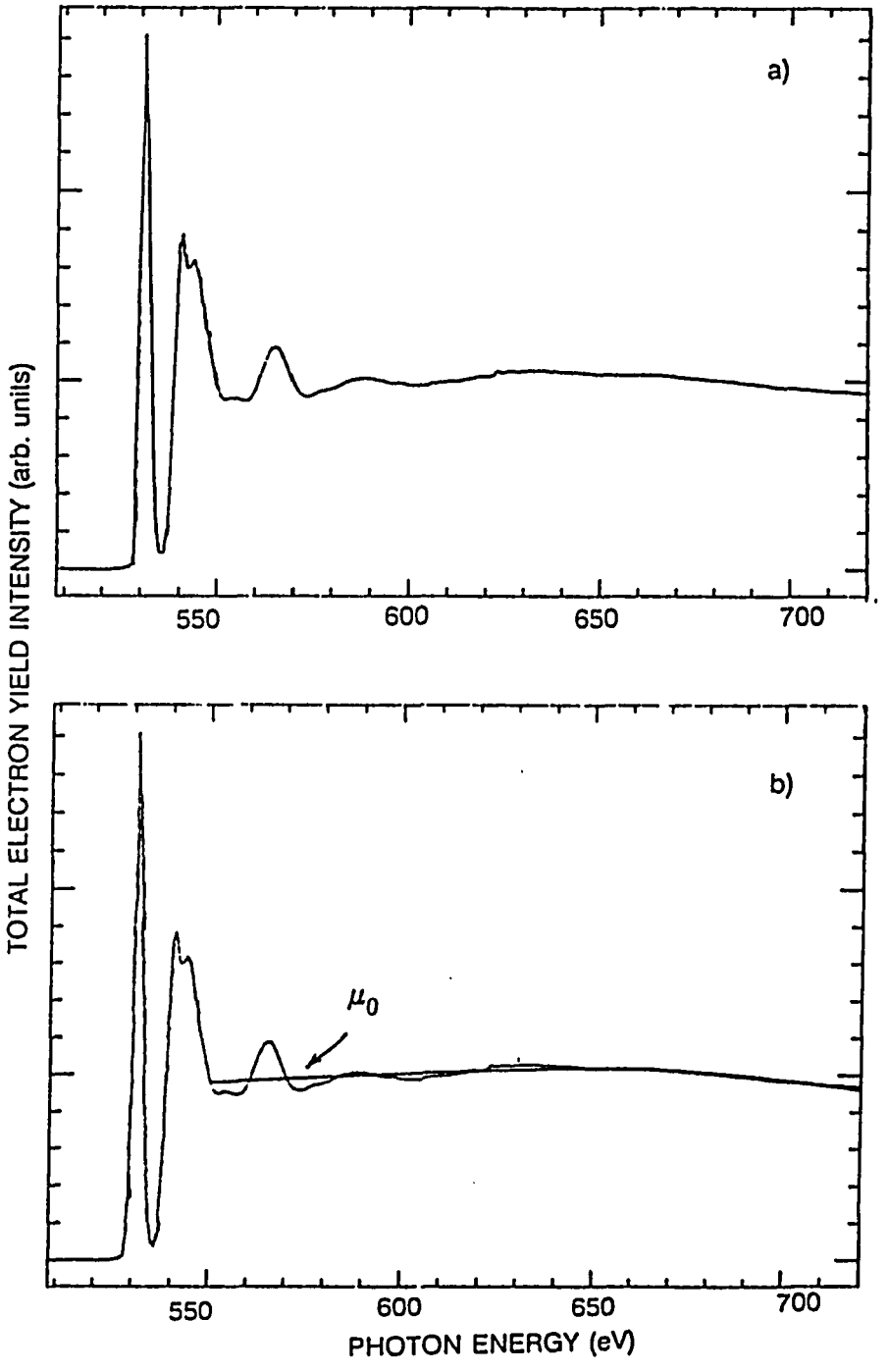

Figure 13. (a) Total electron yield EXAFS spectrum of solid O_2 at 20 K. (b) After normalized to the monochromator output, the curve $\mu_0(E)$ is the best fit to the experimental curve.

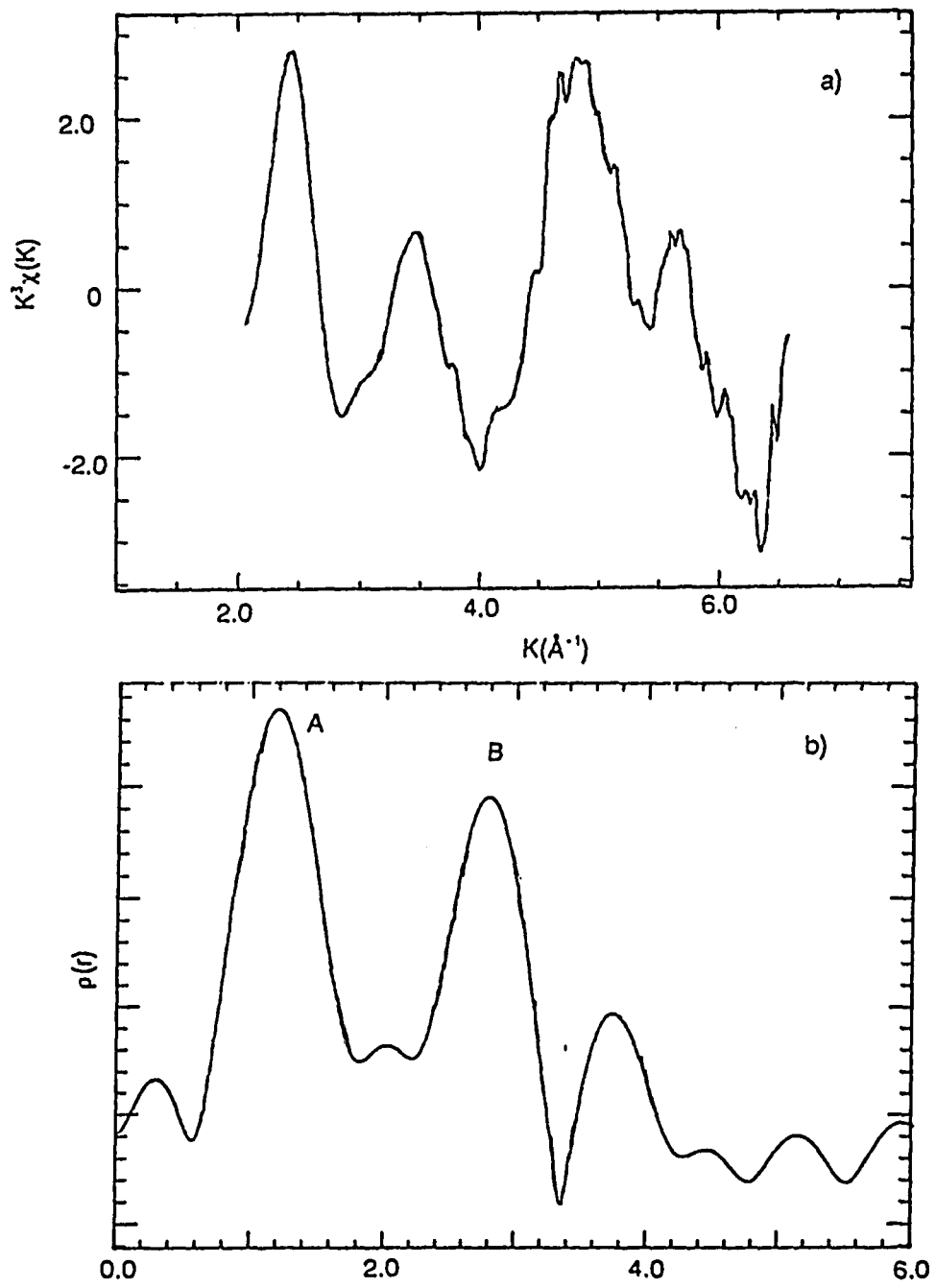

Figure 14. (a) EXAFS ($k^3\chi(k)$) in k-space, where $\chi(k)$ is defined in equation (2.6.3). (b) The Fourier transformed experimental data in r-space.

in k-space (from 2 to 8 $Å^{-1}$) are shown in Fig. 14a, where the $\chi(k)$ is multiplied by a factor of k^3, in order to enhance the oscillations at high k value. The Fourier transformed result in r-space is shown in Fig. 14b. The two prominent peaks at around 1.25 and 2.51 Å correspond to the intramolecular bond length and the intermolecular distance of O_2, respectively. Taking into account the limited wave vector k range and limited knowledge about the phase, this result agrees with previous neutron diffraction (1.23 ± 0.03 Å)[75] and x-ray diffraction measurements (1.15 - 1.22 Å)[62] on solid oxygen. This also agrees with intramolecular bond length (1.207 Å)[76] of gaseous oxygen.

3.4. AES Study of Solid O_2

3.4.1. Results and Discussion

We have studied solid O_2 using x-ray absorption spectroscopy, and found that the spectrum of solid O_2 is different from that of O_2 in gas phase. To have a better understanding, we also measured the Auger electron spectra of solid O_2.

In Fig. 15 we show the AES spectra of solid phase O_2 measured at photon energies of (a) 530.8 eV, (b) 540.3 eV, (c) 547.7 eV, and (d) 557.7 eV, which correspond to promoting the oxygen 1s electron to (a) the π^* resonance, (b) the σ^* resonance, (c) and (d) the ionization continuum, respectively.

The peak marked S in Fig. 13a is due to the participatory Auger process, in which the 1s core electron promoted to the partially filled π^* level participates in the deexcitation, as has been previously demonstrated by Sambe and Ramaker.[77] As mentioned, the final state resulting from this decay, a one-hole (π_g) state, is the same as that produced in the photoemission process, and it should have the same energy. Photoemission measures the binding energy, E_B, of an electronic level, given by

$$E_B = E_0 - E_K , \tag{3.4.1}$$

where E_0 is the exciting photon energy and E_K is the measured electron kinetic energy. In the case of Auger decay, E_0 is just the photon energy required to excite the levels, since the excess energy is carried away by the departing electron. For the π^* resonance, this is 530.8 eV; thus we predict for peak S that E_B = 530.8 - 520.1 = 10.7 eV. This is in good agreement with the 2π binding energy (11.0 eV) of condensed molecular oxygen as measured in photoemission.[78] Compared with the gas phase photoemission spectrum,[79] the 2π peak is shifted about 2.1 eV to lower binding energy. This shift is exactly the same as the shift of the one hole final state Auger peaks in the solid O_2 spectrum relative to the

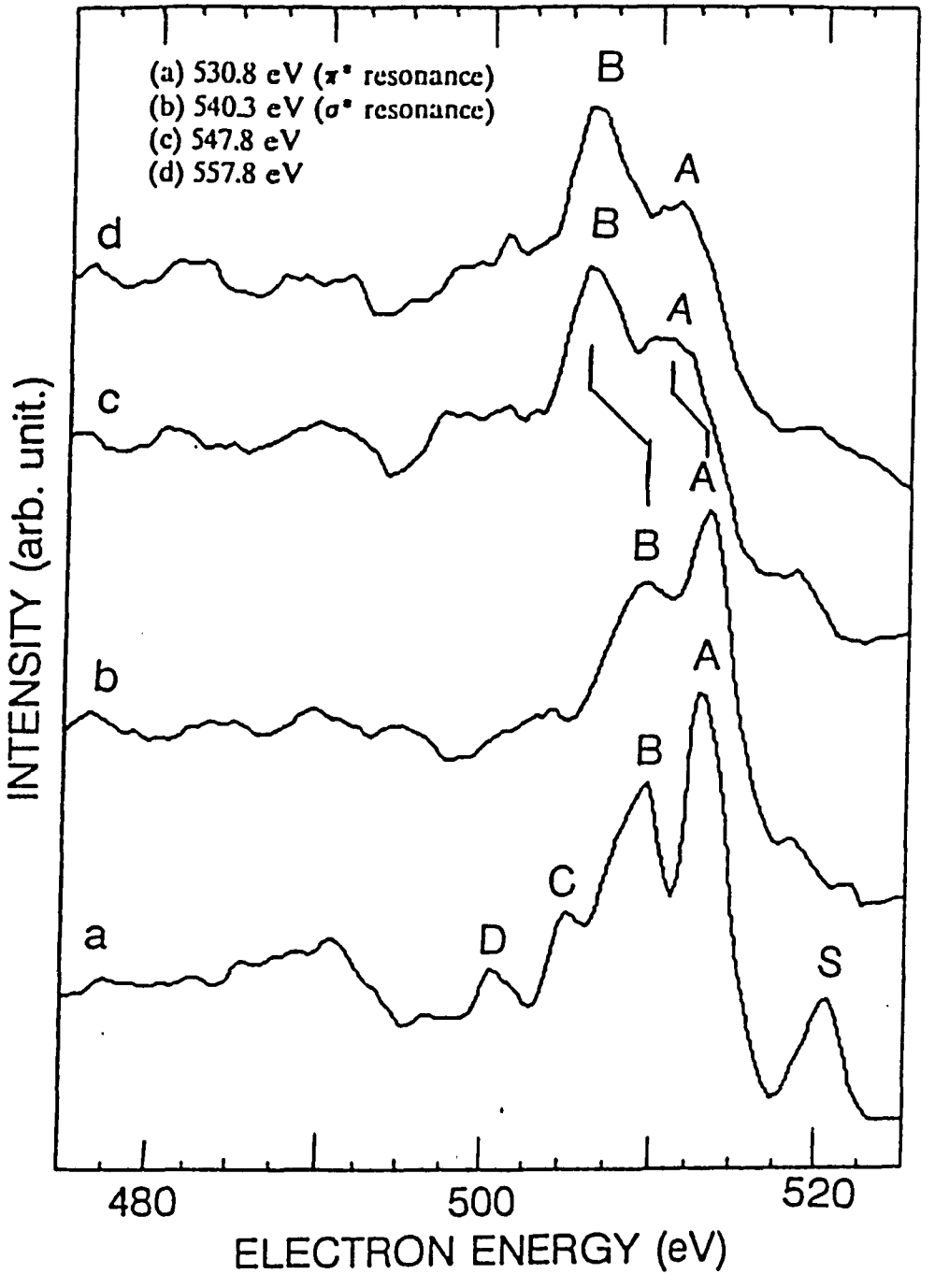

Figure 15. Electron energy spectra measured at 30 K with the incident photon energy set at (a) 530.8 eV (π^* resonance), (b) 540.3 eV (σ^* resonance), (c) 547.8 eV and (d) 557.8 eV.

gas phase spectrum (Table 4). We explain this shift as being due to the final state screening effect in solid O_2 layers. In the solid, when the molecule is photoionized, the neighboring O_2 molecules will polarize to the O_2^+ and screen its charge. The screening results in a lowering of the total energy of the system, with the energy difference given to the emitted photoelectron. Thus the measured photoelectron kinetic energy will be higher in the solid case than that in the gas phase O_2. A similar shift was reported for other molecules.[80] This assignment is also supported by the fact that this peak is absent (Fig. 15b) in our σ^* resonance spectrum and in the high photon energy excitation spectra, in which the 2π level cannot be excited, but is present in the electron impact excitation spectra,[77] as is expected, since the impact electron can give up only a part of its kinetic energy to the absorbing atom.

The other predominant features (labeled A, B and C in Fig. 15a) are due to the spectator Auger process, in which the excited 1s core electron remains in a π^* state as a spectator and a two-hole one-electron final state is reached. Compared with the gas phase O_2 π^* autoionization spectrum,[81] all three peaks are shifted about 2 eV to higher kinetic energy, which is caused by solid state screening effects. Theoretically, this shift should be the same as the shift in photoemission measurements because they have the same final state. In fact, the 2 eV shift observed in our experiment is very close to the 2.1 eV shown in photoemission experiment.[80]

The σ^* resonance decay spectrum is shown in Fig. 15b. Compared with the π^* spectrum of Fig. 15a, the σ^* resonance decay spectrum is similar to the π^* spectrum except that the participatory Auger feature S is absent. In particular, no new features are apparent, indicating that the participatory Auger process does not contribute significantly to the decay of the σ^* resonance. The similarity of the spectra also implies that the autoionization decay channels available to a π^* excited state are similar to those available to the σ^* excited state.

This is reasonable in view of our observation that participatory processes do not play an important role in these decays.

The conventional Auger electron spectra resulting from the Auger decay of the ionized atom are shown in Fig. 15 (c) and (d) at two different photon energies. Within the experimental accuracy, no significant changes in peak positions and intensities are observed in the Auger spectra excited by 547.8 and 557.8 eV photon energies. This similarity shows that excitation at different energies in the continuum do not measurably affect the Auger decay channels. Similar results have recently been observed for gas phase O_2.[81] On the other hand, there are major differences in both peak intensity and position between the AES (Figs. 15c and d) and the autoionization spectra (Figs. 15a and b). Some of the intensity changes may be due to multilayer screening effects. Compared with the gas phase O_2 AES spectrum,[81] peaks are shifted about 10 eV to a higher kinetic energy, which is about five times as large as the corresponding differences in the autoionization spectra. This larger shift maybe understood using a point charge image potential model in which the screening of the (two hole) Auger final state differs from the screening of the (two hole, one electron) autoionization final state. This model predicts that the hole relaxation shift of a localized two hole state is three times larger than that of a one hole state.[82] This is less than what we observed and is possibly due to initial state effects, which are however much smaller than final state effects in this case. This result is similar to the previous measurements on other systems such as $Cr(CO)_6$ studied by Plummer[83] *et al.* and Xe studied by Kaindl[84] *et al.*

Peak positions and assignments (final hole state) of the electron energy distributions are summarized in Table 4.

		Autoionization			Auger		
Label	Final state	Gas(eV)	Solid(eV)	ΔE(eV)	Gas(eV)	Solid(eV)	ΔE(eV)
S	π_g	518.0	520.1	2.1			
A	π_g, π_u	511.0	512.7	1.7	501.0	510.5	9.5
B	π_u, π_u	506.6	508.7	2.1	496.0	506.1	10.1
C	π_g, $2\sigma_u$	503.3	505.0	1.7			

Table 4. Comparison of the electron energies for peaks in the Auger electron and autoionization spectra of solid oxygen and gas phase O_2. ΔE is the energy difference between the feature in the solid oxygen spectrum and the corresponding feature in the gas phase O_2 spectrum.

3.4.2. Summary

In conclusion, we have studied the Auger electron spectra of condensed molecular oxygen for the first time. The Auger spectra of gas phase molecular oxygen have been reported previously and the observed peaks have been assigned.[85] Compared with the spectra of gas phase O_2, the Auger spectra of solid O_2 for both the ionized and excited molecules shift to a higher kinetic energy; for the ionized molecules the shift is ~ 10 eV, while for excited molecules the shift is ~ 2 eV. This may be understood in part by different final state screening effects.

Chapter 4. PES and XAS Studies of Oxygen and Alkali Metal systems

4.1. Introduction

The interaction of oxygen with alkali metals has been studied for many years.[7,8,13,86,87] Since oxygen-alkali metal interaction can form a series of ionic oxygen species, *i.e.*, O^{2-}, O_2^{2-}, O_2^-, and O_3^-, considerable efforts have been made to identify the different oxidation states in the valence band for oxygen adsorbed on alkali metals by using both UPS and XPS.[7,8,13,88,89] In UPS studies on the oxygen/cesium system three different states of oxygen were observed in the valence band and were identified as O^{2-}, O_2^{2-} and O_2^-, respectively.[7,13] The XPS data on the same system show two types of oxidation states which were characterized by two O 1s peaks at 527.5 and 531.5 eV binding energy, respectively. From the shape and position of the Cs peaks and the Auger parameter, these two peaks were assigned to oxygen in $Cs_{11}O_3$ and CsO_2.[90] However, these two peaks were assigned differently to oxygen in CsO_2 and Cs_2O_2 in recent XPS studies.16

Most recently, both occupied and unoccupied electronic levels of NaO_2 and KO_2 have been probed by photoemission spectroscopy (PES), inverse photoemission spectroscopy (IPE), x-ray absorption spectroscopy (XAS), and electron energy loss spectroscopy (EELS).[14,15] An O-O bond length of 1.35 Å is derived for NaO_2 and KO_2.[14] However, the superoxide species in these studies are inconsistent with other UPS results obtained from the potassium-oxygen system[16] and the lithium-oxygen system.[12]

We have investigated in detail the adsorption of oxygen on alkali metals at low temperatures employing both PES and XAS. The PES studies have enabled us to identify the different ionic oxygen species, such as O^{2-}, O_2^{2-} and O_2^-, in both oxygen 1s core level studies and in valence band studies. The derived 1.36 Å O-O bond length in alkali metal

superoxides from the XAS study agrees with previous reports.[14]

4.2. PES Study of Oxygen and Alkali Metal Systems

4.2.1. Solid Oxygen/Cesium System

A.) Results and Discussion

1) Valence Band

A series of valence band photoemission spectra taken at hν = 95 eV for various oxygen exposures are shown in Fig. 16. The spectrum of clean Cs (curve a) shows two sharp, well resolved $5p_{3/2}$ (12.0 eV) and $5p_{1/2}$ (13.9 eV) peaks. The spin orbit splitting of the 5p components is 1.9 eV. The FWHM's (without corrections for instrumental broadening) are estimated to be 0.5 and 1.3 eV for the $5p_{3/2}$ and $5p_{1/2}$ peaks, respectively. The considerable broadening of the $5p_{1/2}$ peak relative to the $5p_{3/2}$ is caused partly by surface and bulk plasmon losses from the $5p_{3/2}$ peak and by intrinsic effects, including Coster-Kronig process. The difference in intrinsic line width between the two 5p levels may not be as drastic as suggested by Simon.[91] The spectrum is in complete agreement with literature data,[86] except that the valence band appears with much lower intensity, which is due to the smaller cross-section for the excitation of the Cs 6s electrons at this photon energy.

Admission of 0.05 L oxygen (curve b) leads to the appearance of a sharp peak at 2.6 eV binding energy, and two shoulders at E_B = 11.4 and 13.0 eV. This three-peak structure, especially the sharp peak at 2.7 eV binding energy, is characteristic of the $Cs_{11}O_3$ suboxide[88]. The appearance of this structure in Fig. 14b indicates that 0.05 L oxygen exposure leads to the formation of some $Cs_{11}O_3$ clusters in the Cs film. A simple bond model has been derived for a $Cs_{11}O_3$ cluster by Ebbinghaus and Simon:[8] 6 of the 11 electrons from the cesium cluster atoms are transferred to the 3 oxygen atoms, leaving 5 electrons for the metallic bonding of the clusters. The compound $Cs_{11}O_3$ is formulated as

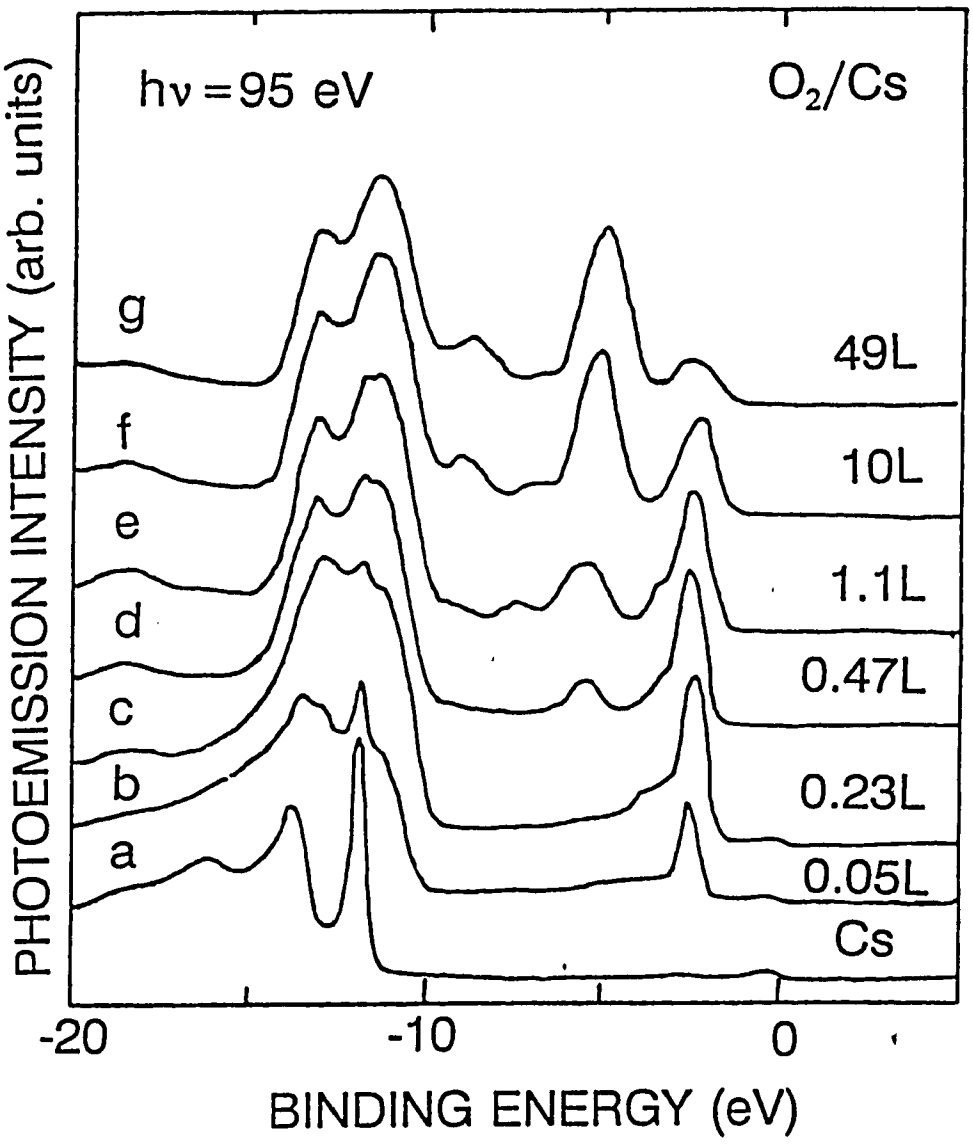

Figure 16. Valance band photoemission spectra of O_2/Cs taken at hν = 95 eV for various oxygen exposures at 35 K. The energy is referenced to the Cs Fermi level. The number represents the oxygen exposure in langmuirs.

a $[Cs_{11}O_3]^{5+}$ ion and five electrons ($5e^-$). Because of the large distance between the O^{2-} ion and Cs^+ ion, the oxygen in $Cs_{11}O_3$ behaves as a weakly stabilized, nearly "gas-like" O^{2-} ion. This nature of the O^{2-} ions explains the small half width of the O 2p band. From the relative intensities of the $Cs_{11}O_3$ features (11.4 and 13.0 eV) and the metallic Cs 5p peaks (12.0 and 13.9 eV), we know that there are more metallic Cs atoms than Cs in the cluster at his oxygen coverage.

As the oxygen exposure increases, the intensity of the 5p peaks from metallic Cs decreases while two shoulders at 11.4 and 13.0 eV develop into full peaks, but the emission from metallic Cs still can be seen after 1.1 L oxygen exposure (curve e). This indicates that the surface stays in the metallic state even after 1.1 L oxygen exposure. Similar results have previously been reported on the same system at 140 K.[4] Metastable deexcitation spectroscopy (MDS)[13] exhibited no peak at E_B = 2.7 eV at the early oxidation stage while this peak was present in the UPS spectrum. Since MDS is extremely surface sensitive and UPS has a finite sampling depth, this experiment showed that the O^{2-} ions are located below the first layer of Cs atoms. This assignment is in agreement with the structure of the $Cs_{11}O_3$ unit (Fig. 17), in which the O^{2-} ions are completely surrounded by Cs.[92]

At this coverage, the 2.6 eV peak becomes broader (curve c) than in curve b. It was reported that the photoemission spectrum of Cs_2O is similar to that of $Cs_{11}O_3$, but the width (1.5 eV) of the O 2p peak at 2.7 eV binding energy in Cs_2O is much larger than the width (0.6 eV) in $Cs_{11}O_3$.[8] In our experiment, the measured full width at half maximum (FWHM) of 2.7 eV peak changes from 0.7 eV (curve b) to 1.2 eV (curve e) as oxygen exposure is increased from 0.05 L to 10 L. This result suggests that initial oxygen exposure on the cesium surface leads to the formation of $Cs_{11}O_3$ clusters and additional oxygen exposure leads to the formation of Cs_2O. It is worthwhile to point out that there is another

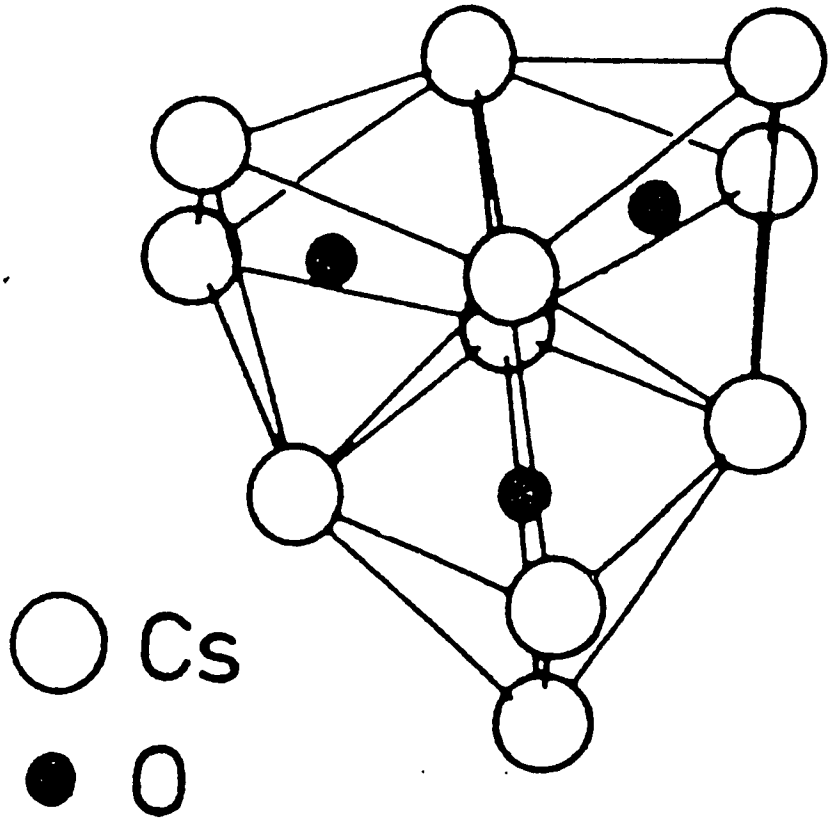

Figure 17. The structure unit of $Cs_{11}O_3$ (Ref. 92).

Fermi level, while Cs_2O only shows one broad valence band.[4] Because the photoemission cross-section of the Cs 6s conduction band is very small at the photon energy used it is hard way to distinguish whether the O^{2-} ion is in a $Cs_{11}O_3$ or in a Cs_2O complex. Since cesium suboxides are metallic while Cs_2O is a semiconductor, $Cs_{11}O_3$ will have a filled conduction band and thus have a sharp to see this change in Fig. 16.

As the oxygen exposure is increased, two additional peaks appear at E_B = 5.6 and 7.5 eV (Fig. 14d). Simultaneously the peak at 2.7 eV broadens and shifts to 3.5 eV. Compared with the peak position of peroxide species (O_2^{2-}) in the Cs_2O_2 complex reported by Woratschek *et al.*[13] (3.2, 6.1 and 7.5 eV) and Su *et at.*[7] (3.3, 6.4 and 7.8 eV), it is evident that the end product at this oxidation stage is cesium peroxide (Cs_2O_2).

After 10 L O_2 exposure, a new feature appears at 9.0 eV binding energy (curve f) and shifts to a lower binding energy as increasing the O_2 exposure. At 49 L O_2 exposure this feature is at 8.6 eV, and the peaks which were at 7.5 and 5.6 eV shift to 6.6 and 4.8 eV, respectively. Su *et al.* identified the superoxide ion O_2^- with peaks at 4.7, 5.8, 6.2, 8.5 and 10.7 eV binding energy. Because the 10.7 eV peak overlaps with the Cs 5p emission, it is hard to see the 10.7 eV feature in our case. Comparing our data and the data reported by Su *et al.*, it is evident that 10 L O_2 exposure leads to the formation of O_2^- state which corresponds to the transition from Cs_2O_2 to CsO_2. The features at 3.5 and 7.5 eV are characteristic of O_2^{2-}. The intensity of these peaks decreases with increasing oxygen coverage, but they can still be seen even after 49 L O_2 exposure. This indicates that no complete transformation into CsO_2 takes place under our conditions.

2) Core Level

The O 1s core level XPS spectra taken at hν = 1486.7 eV for various oxygen exposures are shown in Fig. 18. At low oxygen coverage, we see one prominent peak at

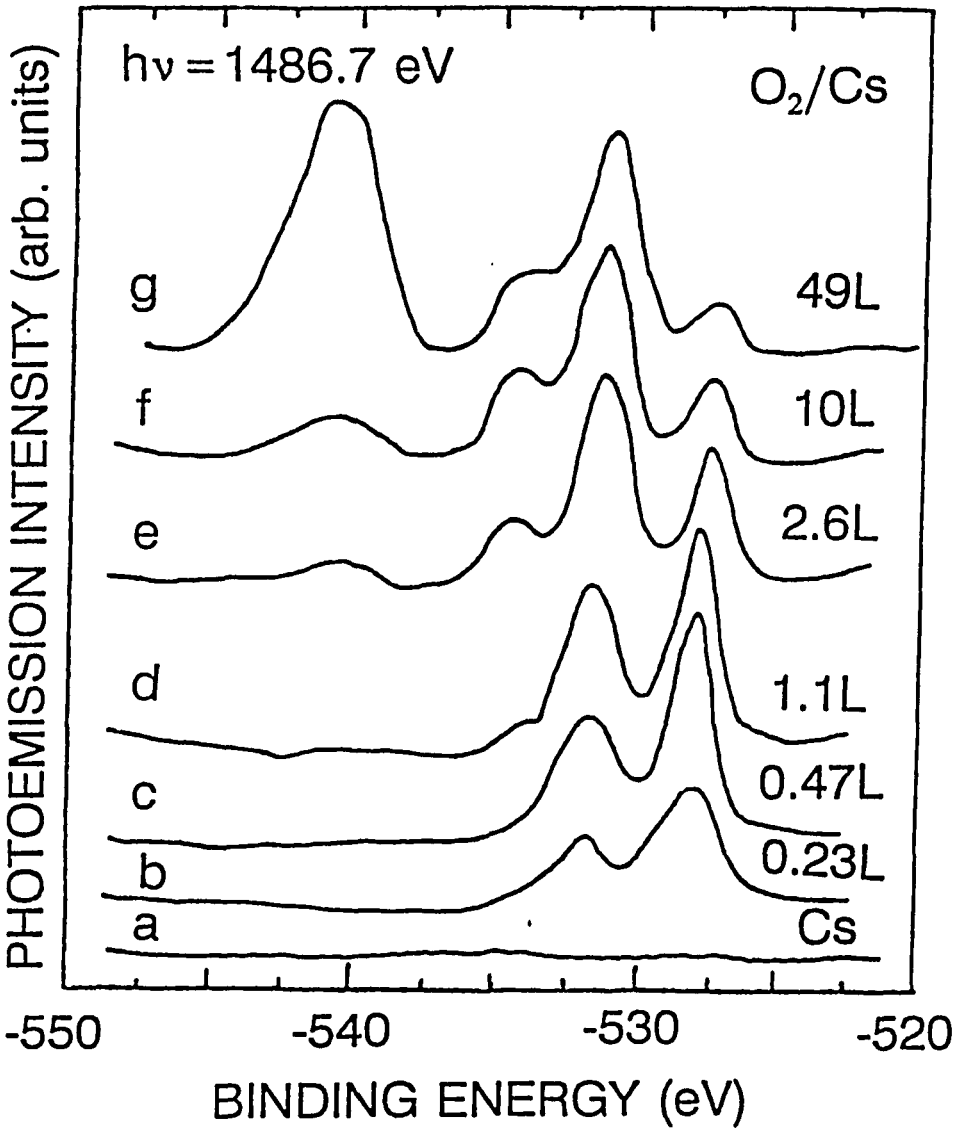

Figure 18. The O 1s core level XPS spectra of O_2/Cs taken at hν = 1486.7 eV for various oxygen exposures at 35 K. The energy is referenced to the Cs Fermi level. The number represents the oxygen exposure in langmuirs.

528.0 eV, and a shoulder at 532.5 eV binding energy (curve b). From the previous UPS discussion, we know that at this initial oxidation stage subsurface O^{2-} is the dominant product. We therefore identify the 528.0 eV feature as O^{2-}. This assignment is in agreement with previous x-ray photoemission studies on the Ag-O-Cs system[90] and O-K system,[10] in which peaks at 527.5 and 528.2 eV binding energy were attributed to oxygen in Cs_2O and K_2O, respectively. The stable oxide feature, with a formal valence state of O^{2-}, is generally at about 530.0 eV,[16] but in our case this feature appears at 528.0 eV. We believe that this peak is due to incorporated O^{2-} ions located below the top layer of Cs atoms, as previously mentioned. It is reasonable that these ions would be screened more effectively and therefore have a smaller binding energy. This argument is also consistent with the valence band result: the O^{2-} feature is at 2.6 eV binding energy for cesium oxide and potassium oxide as compared to 5.5 eV in the case of lithium oxide, where the O 1s core level binding energy is 530.5 eV.[12]

From the previous UPS discussion, we assign the 532.5 eV feature to a peroxide feature in Cs_2O_2 complex. The fact that the relative intensity of this peak and the oxide feature both increase with increasing oxygen exposure (curve b-d), which is expected from the normal trend of the cesium oxidation process supports this assignment.[6] The value of 532.5 eV observed here is in agreement with other estimates for peroxide studies in other alkali metal systems.[12,93] In the study of the Ag-O-Cs system a peak at 531.5 eV was observed and was assigned to chemisorbed oxygen.[90] We believe this is a peroxide.

As oxygen concentration increases, the 532.5 eV peak intensity increases, and finally becomes the dominant feature after a 2.6 L oxygen exposure. By this exposure, two new peaks appear at 534.5 and 540.0 eV binding energy (curve e and f). One can easily assign the 540.0 eV peak to solid molecular O_2. Since the work function of Cs is about 1.5 eV, the

molecular oxygen peak would be about 541.5 eV when referenced to the vacuum level, which is smaller than the measured value (543.1 eV) for gas phase O_2.[79] We believe that the 1.6 eV difference is due to screening effect in solid O_2 as discussed in the previous chapter. The screening effect from the metal surface may also cause shift, especially in the case of submonolayer oxygen coverage.

The feature at 534.5 eV has been previously observed when lithium was deposited on solid oxygen, in which this feature was identified with the superoxide (O_2^-).[12] By analogy, we assigne this feature to O_2^- in a CsO_2 complex. Physically a superoxide should appear between the molecular feature at 540.0 eV and the peroxide feature at 532.5 eV. If one adopts the ideal model, namely 0, 1 and 2 charge per atom for O_2, O_2^{2-} and O^{2-} ion, respectively, from the plot of the oxygen charge number verses the corresponding O 1s binding energy, one can extrapolate that 535 eV corresponds to half oxygen charge, named superoxide. Thus we assigne 534.5 eV peak to superoxide. This assignment is also supported by the fact that the Cs 3d and the O 1s cross-section ratio obtained from the experimental spectra and this assignment quantitatively agrees with the theoretical value. This is discussed in detail below.

In Fig. 19 we show the Cs 3d core level x-ray photoemission spectra as a function of oxygen exposure. The clean Cs (curve a) shows two sharp peaks at 726.6 and 740.5 eV binding energies, which arise from the Cs $3d_{5/2}$ and $3d_{3/2}$ core levels, respectively. The position of these peaks are in good agreement with previous reported values.[94]

Two broad asymmetric peaks at about 730 and 743 eV correspond to energy loss due to the creation of surface and bulk plasmons. These plasmon-loss peaks are quickly quenched by a small coverage of oxygen (Fig. 19 curve b). After oxygen exposure, the Cs 3d peaks broaden and shift to lower binding energy by about 1 eV. The shift to lower

binding energy is in contradiction with simple charge transfer arguments. Ayyoob and Hegde[95] reported similar results on the co-absorption of oxygen and alkali metal (K or Cs) on silver surface, in which the shift was explained in terms of the surface-to-bulk transport of alkali metal. This certainly is not the case in our experiment. Although the real cause of this shift is still unclear, the directions of the shifts in our experiment and in Ayyoob's work are the same. The peak broadening observed in our experiment may be due to the co-existence of different oxidation states.

B.) Calculation

In order to verify our assignment, we calculated the O 1s and the Cs 3d photoemission cross-section from this assignment and the measured XPS spectra (Figs. 18 and 19).

It is known that the photoemission intensity is related to the photoionization cross-section σ_i through[96]

$$I_i = F N_i \sigma_i \theta_i \lambda_i TDG , \qquad (4.2.1)$$

where F is the photon flux, N_i is the atomic density, θ_i is the asymmetry factor, which depends on the angle between the incident photon and the emitted electron, and λ_i is the mean free path length of the photoelectron. T, D and G are the transmission, detection and geometry matrixes, respectively. For a fixed sample and light source,

$$I_i = C N_i \sigma_i \lambda_i , \qquad (4.2.2)$$

where C is a constant. Since the mean free path lengths of Cs 3d (E_K = 760 eV) and O 1s (E_K = 950 eV) photoelectrons are almost identical at 1486.7 eV photon energy, we can neglect the difference in mean free path length λ. Thus the photoelectric cross-section ratio R of the Cs 3d and the O 1s is simply:

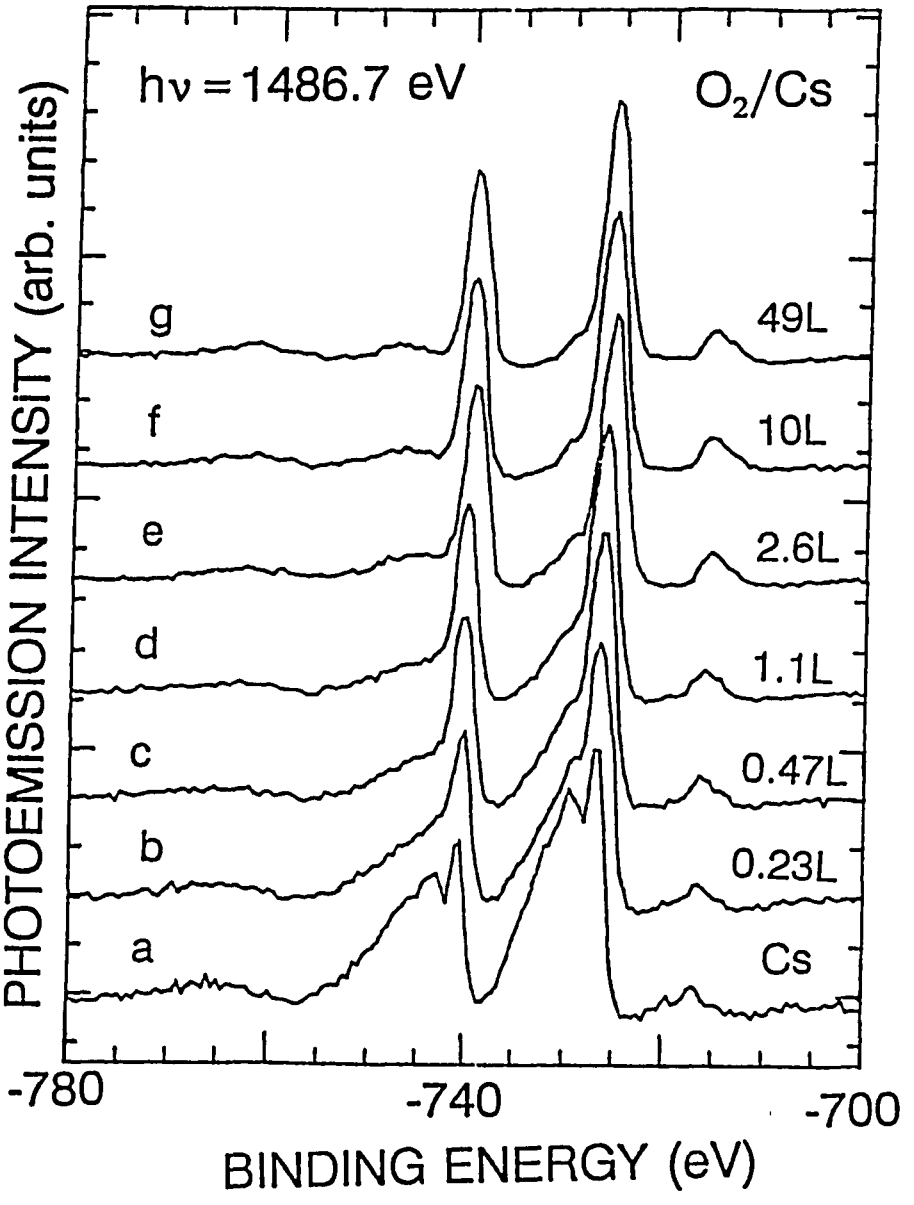

Figure 19. The Cs 3d core level XPS spectra of O_2/Cs taken at hν = 1486.7 eV for various oxygen exposures at 35 K. The energy is referenced to the Cs Fermi level. The number represents the oxygen exposure in langmuirs.

$$R = \frac{\sigma_{Cs}}{\sigma_O} = \frac{I(Cs)N_O}{I(O)N_{Cs}}, \tag{4.2.3}$$

or

$$I(Cs) = R\,\frac{N_{Cs}}{N_O}\,I(O). \tag{4.2.4}$$

We can rewrite equation (4.2.4) in terms of different oxygen species by taking account of atomic density N

$$I(Cs3d)_{total} = I_{Cs} + I_{CsO_2} + I_{Cs_2O_2} + I_{Cs_2O}$$

$$= I_{Cs} + R\left(\frac{N_{CsO_2}}{N_{O_2^-}}\,I(O_2^-) + \frac{N_{Cs_2O_2}}{N_{O_2^{2-}}}\,I(O_2^{2-}) + \frac{N_{Cs_2O}}{N_{O^{2-}}}\,I(O^{2-})\right). \tag{4.2.5}$$

Solving for R, we find

$$R = \frac{I(Cs3d)_{total} - I_{Cs}}{AI(O_2^-) + BI(O_2^{2-}) + CI(O^{2-})},$$

where

$$A = \frac{N_{CsO_2}}{N_{O_2^-}},$$

$$B = \frac{N_{Cs_2O_2}}{N_{O_2^{2-}}},$$

and

$$C = \frac{N_{Cs^+O}}{N_{O^{2-}}} . \qquad (4.2.6)$$

A, B, and C are the atomic ratios of cesium and oxygen in superoxide, peroxide and oxide complexes, respectively, and I(i) is the measured photoemission intensity of the i^{th} species. For superoxide CsO_2 and peroxide Cs_2O_2 complexes, A and B are 0.5 and 1, respectively. Previous studies[4,13] and our UPS discussion suggests that there are at least two types of cesium oxides ($Cs_{11}O_3$ and Cs_2O) in the early oxidation stage of cesium, and hence two different C values are used: 2 for the Cs_2O complex and 11/3 for the $Cs_{11}O_3$ complex.

According to equation (4.2.6), R should be a constant, independent of oxygen exposure. The obtained fraction for various oxygen exposures are summarized in Table 5. Note that the theoretical cross-section of the Cs 3d and the O 1s at hν = 1486.7 eV is 6 and 0.4 Mb[97], respectively, thus the ratio expected theoretically is 15. Because of the overlap of oxygen peaks in O 1s spectra (Fig. 18), it is difficult to measure the intensity accurately for all oxygen species. The estimate error is 15%. Considering this, apparently our results are in good agreement with published theoretical data.

It can be seen from Table 5 that in the low oxygen exposure range (0.2 to 0.5 L), the R value (43 at 0.2 L and 27 at 0.5 L) is much larger than the theoretical value, even assuming the oxide is entirely $Cs_{11}O_3$. This discrepancy is mainly due to the excess Cs intensity arising from the metallic Cs atoms. Since in Fig. 19 what we measured is the total photoemission intensity of the Cs 3d core level, we cannot separate I_{Cs} from $I(Cs3d)_{total}$. Thus the R value obtained from equation (4.2.6) is expected to be larger than the real value. After 1 L oxygen exposure, the R value is 19 assuming that the oxide is in $Cs_{11}O_3$ complex. This value is quite close to the theoretical value. This result indicates that about 1 L O_2

O_2 Exposure	R	Stage
0.2 L	43 ($Cs_{11}O_3$)	
0.5 L	27 ($Cs_{11}O_3$)	
1 L	19 ($Cs_{11}O_3$)	$Cs_{11}O_3$
2.6 L	17 ($Cs_{11}O_3$) 23 (Cs_2O)	Mixed
5.6 L	17 ($Cs_{11}O_3$) 23 (Cs_2O)	
10 L	21 (Cs_2O)	
13 L	20 (Cs_2O)	Cs_2O
49 L	20 (Cs_2O)	

Table 5. The intensity ratio of the Cs 3d core level and the O 1s components obtained from the measured spectra and proposed assignment for various O_2 exposures.

exposure on Cs will convert the surface region as probed by XPS into $Cs_{11}O_3$.

In the medium oxygen exposure range (2.6 to 5.6 L), the R value for the two different oxide complexes ($Cs_{11}O_3$ and Cs_2O) is 17 and 23, respectively. The average value of 20 is very close to the R value obtained for 1 L oxygen exposure. We conclude that two types of cesium oxide complex coexist at this oxidation stage. This result supports the domain growth mechanism proposed by Woratschek *et al.*:[13] Once $Cs_{11}O_3$ nuclei take up additional oxygen they transfer into Cs_2O_2 with Cs_2O as intermediate, while the rest still remains as $Cs_{11}O_3$. These conclusions are also in agreement with the finding by Su *et al.*,[7] who found that the formation of Cs_2O_2 starts long before saturation with O^{2-} is reached.

In the high oxygen exposure range (10 to 49 L), R is almost constant (~20) assuming that the oxide is in a Cs_2O complex. This can be understood as meaning either $Cs_{11}O_3$ has been converted to Cs_2O, or that if there are any $Cs_{11}O_3$, it is too deep at this oxidation stage and cannot be probed by XPS.

C.) Conclusion

In conclusion, we have studied the O_2/Cs system at 35 k using photoemission. Both UPS and XPS results show that three different oxygen species coexist at this temperature, depending on the oxygen exposure. Assignments of these features in both the O 1s core level and valence band spectra have been made for O^{2-}, O_2^{2-}, and O_2^- species, which corresponds to the formation of oxide, peroxide, and superoxide, respectively. Small O_2 exposure leads to the incorporation of oxygen species, O^{2-} ions, under the cesium surface, and to the formation of $Cs_{11}O_3$.[13] After completion of the $Cs_{11}O_3$ layer, additional oxygen exposure makes $Cs_{11}O_3$ transform into Cs_2O_2 and CsO_2, with Cs_2O as an intermediate. No complete transformation into CsO_2 takes place under our conditions. We also calculated the photoelectric cross-section ratio of Cs 3d and O 1s core levels from measured

photoemission spectra and our assignment for the superoxide, peroxide, and oxide oxygen species. The obtained results quantitatively agree with theoretical values.

4.2.2. Solid Oxygen/Potassium System

Figure 20 shows valence band photoemission spectra taken at 80 eV photon energy for O_2/K at different oxygen exposures. The corresponding O 1s core level spectra for the same oxygen exposures are shown in Figure 21. A sharp peak at 18.3 eV binding energy in the clean K spectrum (Fig. 20a) is the K 3p peak. A broad feature at about 22 eV is attribute to surface and bulk plasmon-loss in the metal. Both the 18.3 eV binding energy of the K 3p and the 3.7 eV plasmon-loss energy are in good agreement with previously published data.[10]

Admission of 0.03 L oxygen (Fig. 20b) leads to the appearance of a peak at 2.7 eV and a shoulder at about 5.6 eV binding energy. Similar to the oxygen/cesium system, this small oxygen exposure causes the reduction of the plasmon-loss feature intensity, which in fact is completely invisible after 0.15 L oxygen exposure. The 2.7 eV feature in the valence band was previously observed in the same system at 90 K,[10] and was assigned to O 2p derived band associated with potassium oxide. Correspondingly, we assign the 2.7 eV peak to O^{2-} in a K_2O complex.

As the oxygen exposure is increased, the 5.6 eV peak intensity grows rapidly relative to the 2.7 eV feature (Fig. 20c), and both peaks gradually shift to 6.3 and 3.0 eV (Fig. 20d). The corresponding O 1s core level spectrum shows a double structure with peaks at 528.0 and 532.0 eV (Fig. 21b and c). This double structure indicates the existence of oxygen in two distinctly different chemical environments. Petersson and Karlsson observed a similar double structure when oxidizing potassium at 90 K, where the two features were at 528.2

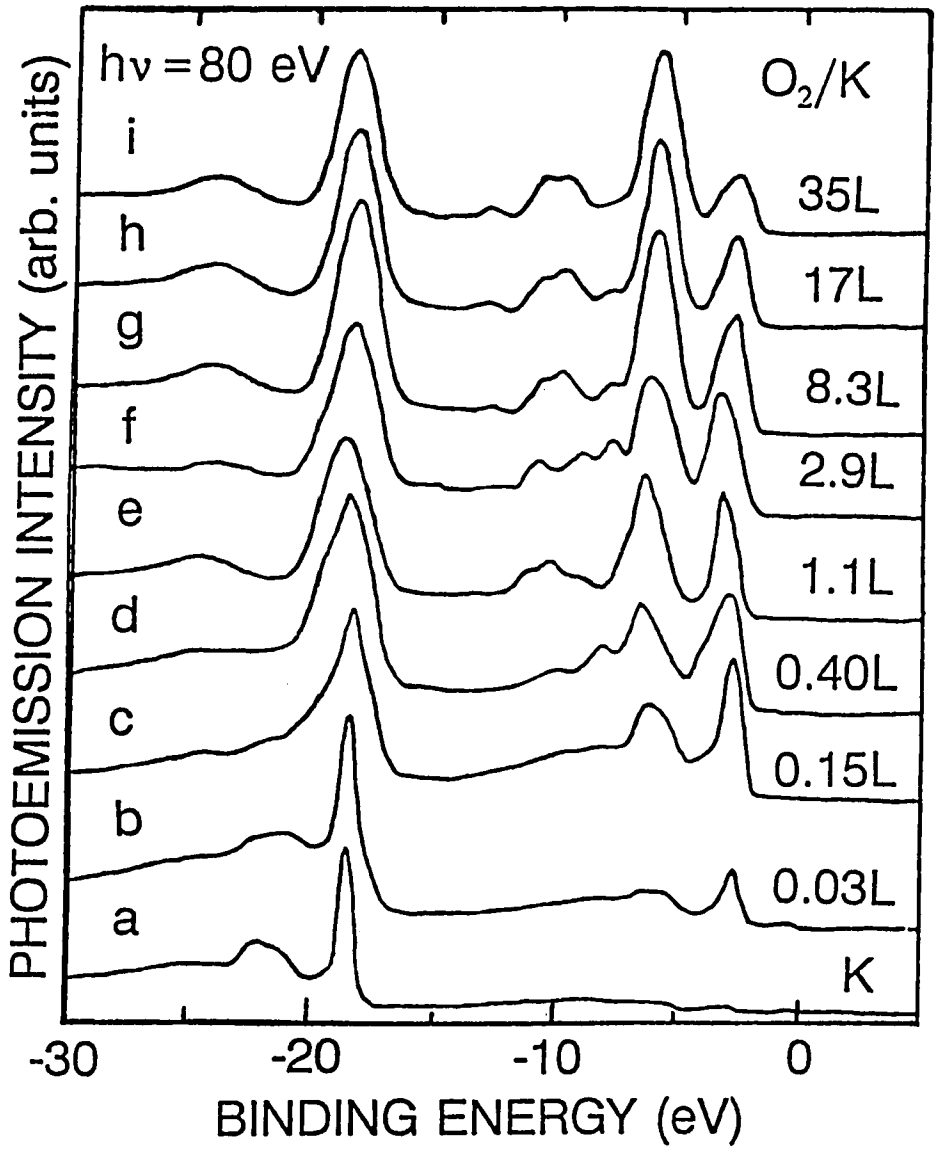

Figure 20. Valence band spectra of O_2/K taken at hν = 80 eV for various oxygen exposures at 35 K. The energy is referenced to the Cs Fermi level. The number represents the oxygen exposure in langmuirs.

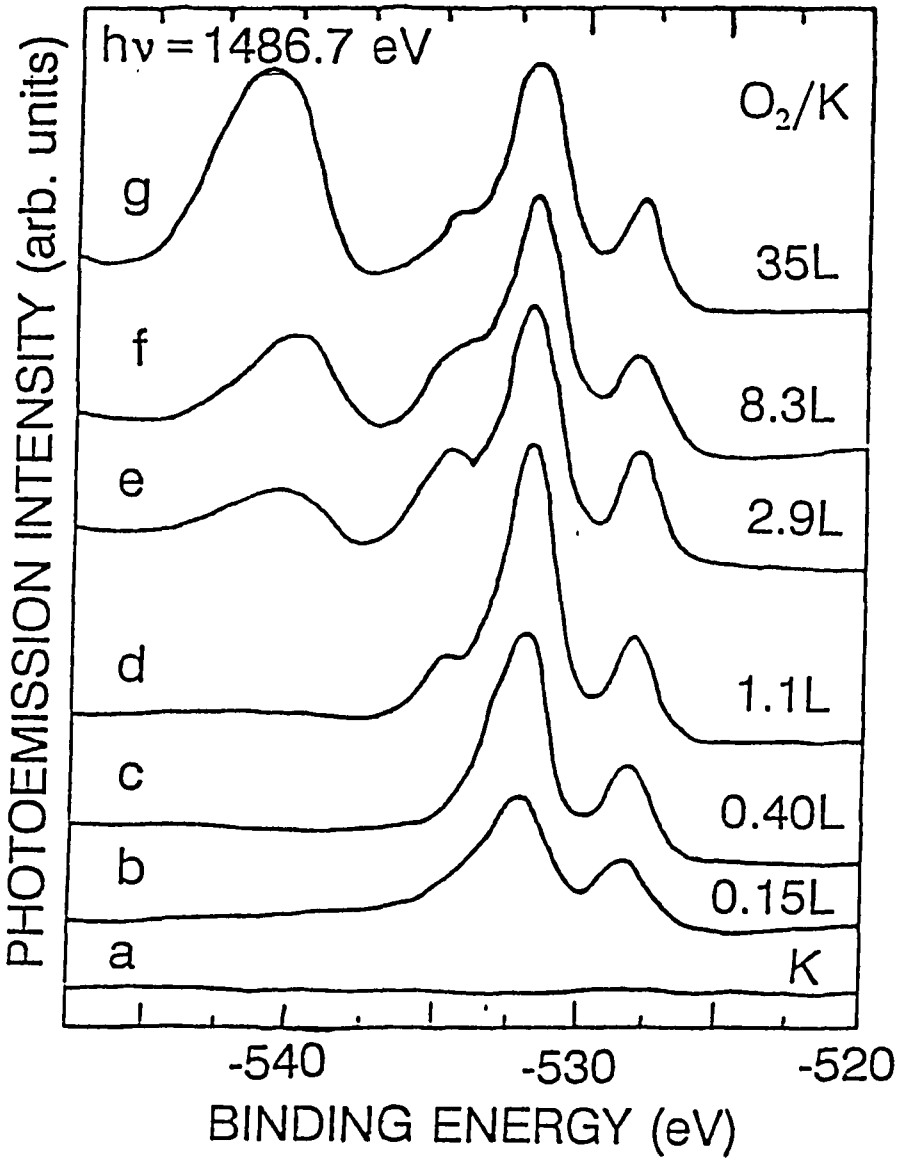

Figure 21. The O 1s core level XPS spectra of O_2/K taken at hν = 1486.7 eV for various oxygen exposures at 35 K. The energy is referenced to the Cs Fermi level. The number represents the oxygen exposure in langmuirs.

and 531.9 eV.[10] They assigned the 528.2 eV peak to the oxygen in an oxide form and the 531.9 eV peak to physisorbed oxygen on the potassium oxide. Clearly, the assignment for 531.9 eV peak is incorrect since the melting point of solid O_2 is only 50 K, while the 531.9 eV feature still exists even after heating the sample to 255 K. Note that we saw physisorbed oxygen at 540 eV (Fig. 21e). Recently, the interaction of solid oxygen with various metals has been studied[16] and the feature at about 531.5-533.0 eV was identified as a peroxide species where two electrons were donated to an oxygen molecule. We identify the 532.0 feature as the peroxide species in a K_2O_2 complex, and the 528.0 eV as an oxide species in a K_2O complex.

As more oxygen is condensed, the intensities of both the 6.3 eV feature in the valence band spectrum and the 532.0 eV peak in the core level spectrum increase rapidly relative to the 3.0 eV feature and 528.0 eV peak. Thus, it is evident that the 3.0 eV feature is related to the 528.0 eV peak, while the 6.3 eV feature is related to the 532.0 eV peak. After 1.1 L oxygen exposure, a new peak appears at about 10.0 eV binding energy in the valence band spectrum (Fig. 20e). The corresponding core level spectrum (Fig. 21d) shows a new feature at 534.5 eV binding energy. Recent photoemission studies[16] show that a feature near 535.0 eV in the O 1s core level spectra was observed when Li, K, Cs, and La were deposited on solid oxygen, and this feature was identified with one electron being donated to an oxygen molecule, *i.e.*, the superoxide species (O_2^-). We correspondingly identify the 534.5 eV feature as a superoxide species in KO_2 complex. Petersson and Karlsson observed the same feature at 534.5 eV when exposure O_2 on potassium surface at 90 K.[10]

Further oxygen exposure leads to the appearance of a peak at 540 eV which is due to molecular O_2. Compared with the gas phase O_2 ionization potential (543.1 eV), there

is about 1 eV shift after correcting for the potassium work function (2.2 eV). This shift is due to the effect of screening as discussed before.

As noted in Fig. 20 that both the shape and position of the K 3p peak change during the oxidation process. Firstly, there is a striking increase in the intensity of the K 3p peak. Secondly, there is a rapid increase in the width of the K 3p core level. After correcting for instrumental resolution, the full width at half maximum (FWHM) of the clean K 3p peak is 0.6 eV and the FWHM of the "potassium oxide" K 3p peak is about 1.9 eV. An increase in intensity and a threefold broadening of K 3p peak were observed when potassium reacted with CO.[98] Similar results were reported in oxidation of Na; the increasing width was interpreted in terms of a shortened lifetime of the core hole due to a faster interatomic Auger decay process.[11] We believe that the intensity increases because oxygen suppresses the energy loss processes that remove intensity from the K 3p level. This is supported by the fact that plasmon-loss features decrease as increasing the oxygen exposure. An additional contribution to this intensity increase may be due to the increase in alkali metal atomic density when passing from the metal to a polycrystalline oxide.[99]

We conclude our discussion by comparing our present data with previous results. Good agreement is found with the photoemission data from oxidized potassium as reported by Petersson and Karlsson.[10] They observed two different oxidation states in both UPS and XPS spectra at 90 K. The observed oxide species (O^{2-}) in K_2O, which was characterized by a single peak at 2.7 eV in the valence band spectrum and a feature at 528.2 eV binding energy in the O 1s core level spectrum, is in good agreement with the present study (Fig. 20b and 21b). The other oxidation state observed in their spectra, which was characterized by a triplet structure (peaks at 3.8, 7.0, 8.3 and a shoulder at 10.5 eV) in the valence band spectrum and a peak at 531.9 eV in the XPS spectrum, also agrees with our data (Fig. 20d

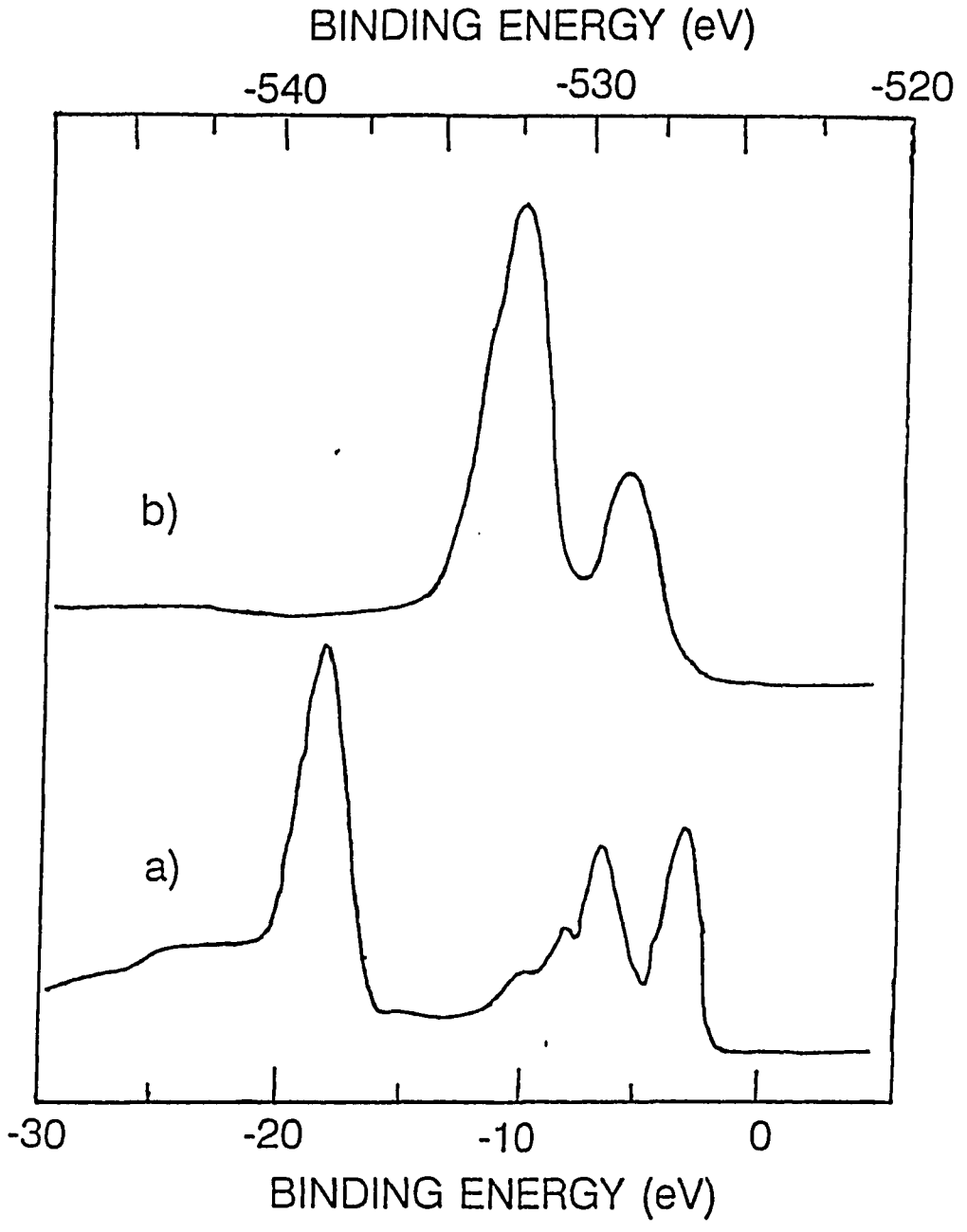

Figure 22. (a) Valence band and (b) the O 1s core level photoemission spectra taken after 0.4 L oxygen exposure on patassium at 35 K.

and 21c). For a better comparison, the valence band spectrum for 0.4 L oxygen exposure on potassium in Fig. 20d is reproduced in Fig. 22 (curve a). The corresponding O 1s core level spectrum is also shown in Fig. 22. The triplet structure (peaks at 2.9, 6.3, 8.0 and ashoulder at 9.8 eV) is clearly seen in Fig. 22a. This result indicates that the initial oxidation process is the same at two different temperatures (35 K and 90 K).

Surprisingly, the spectrum in Fig 22a is almost identical to the KO_2 valence band spectrum reported by Bertel *et al.*[14], where the potassium was deposited in an ambient oxygen atmosphere of ~ 3 X 10^{-7} Torr oxygen and a 30-50 Å oxide film was obtained. In their spectrum, four peak positions are at 2.4, 5.5, 6.9 and 9.3 eV.[14] Compared with present data (Fig. 22a), all spectra features are shifted consistently by 0.5 to 1.0 eV toward lower binding energy. This difference seems to be in the positioning of the Fermi level rather than in the actual binding energies because the K 3p binding energy in our spectrum is 18.3 eV; while Bertel *et al.* report a K 3p binding energy of 17.3 eV.

Bertel *et al.* claimed that all the observed photoemission features in the valence band spectrum are due to superoxide. Our measurements show that at this oxidation stage, there are two peaks (528.0 and 532.0 eV) in the O 1s XPS spectrum (Fig. 22b); no superoxide or molecular oxygen species are observed at this oxygen exposure. Clearly features in the valence band spectrum at this oxygen coverage are not due to superoxide; rather they must be mainly due to the peroxide, or possibly a mixture of peroxide and oxide.

The comparison of valence band states of this work and previous studies for both cesium-oxygen and potassium-oxygen complexes is summarized in Table 6.

4.2.3. Solid Oxygen/Lithium System

Photoemission studies of solid oxygen with lithium at 35 K has been reported by S.L.

	E_B (eV)		E_B (eV)		E_B (eV)	Reference
	4.8, 6.6, 8.6		3.5, 6.6, 8.6		2.7	a
CsO_2	4.7, 5.8, 8.5	Cs_2O_2	3.3, 6.4, 7.8	Cs_2O	2.7	b
	4.5, 5.6, 8.6		3.3, 6.1, 7.5		2.8	c
	~ 10		3.0, 6.3		2.7	a
KO_2	2.4, 5.5, 12.0, 14.3	K_2O_2		K_2O		d
			3.8, 7.0		2.7	e

a: This work.
b: Su *et al.*, ref. 7.
c: Woratschek *et al.*, ref. 13.
d: Bertel *et al.*, ref. 14.
e: Petersson and Karlsson, ref. 10.

Table 6. The comparison of valence band states between this work and the previous studies on cesium-oxygen and potassium-oxygen complexes. The binding energy is referenced to the substrate Fermi level.

Qiu *et al.*[12] and Strongin *et al.*[100], and at room temperature by Zavadil *et al.*[101] The data from Ref. 12 are reproduced in Figs. 23 and 24. At low oxygen exposure the O 1s core level spectrum shows a single peak at 530.5 eV, as shown in Fig. 23a. A similar feature at 530.8 eV was observed in the oxidation of Li at room temperature.[101] In their case, this feature was identified as a O^{2-} feature in the formation of Li_2O. Note that this is the most Li-rich compound, as is expected for a Li substrate with small amounts of oxygen. Compared to our results, we find that the binding energy of oxygen in the Li case is about 2 eV deeper than in the Cs and K cases. We believe that this is due to the combined effect of atomic size and screening. The atomic size of the Cs (3.34 Å) and K (2.77 Å) is considerable larger than Li (2.05 Å), and we have already suggested that in the Cs and K, the oxygen penetrates below the surface, which leads to better screening of the O 1s core hole.[16] This may not be possible in the case of Li because of the smaller atomic size. In addition, the extra-atomic relaxation energy is larger in Cs (or K) due to the large, and hence more polarizable Cs^+ (or K^+) ions. This also explains why the corresponding valence band feature is at 5.5 eV in the Li case (Fig. 24a), instead of at about 3 eV for the K and Cs cases.

More oxygen exposure leads to the next most oxygen-rich compound, signaled by a peak at 532.5 eV (Fig. 23c). By analogy with the K and Cs cases, we assign this feature to the peroxide species, in which two electrons are donated to the oxygen molecule rather than the atom, and form a Li_2O_2 complex. The corresponding valence band spectrum shows a feature at about 8.5 eV (Fig. 24c). However, the emerging features of the solid oxygen begin to make the identification of peroxide difficult in the valence band spectrum. In recent room temperature oxidation studies of Li,[101] only a small shoulder was observed in the O 1s XPS spectrum. This observation is contradictory to thermodynamic parameters

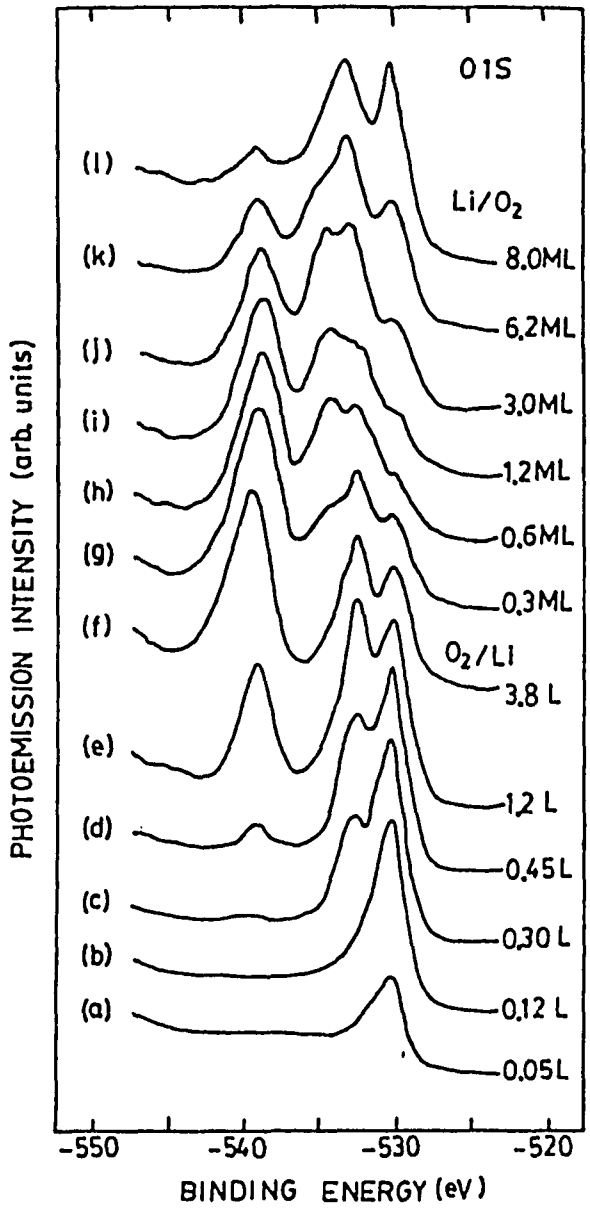

Figure 23. The O 1s core level photoemission spectra of oxygen-lithium system taken at 1486.7 eV photon energy.

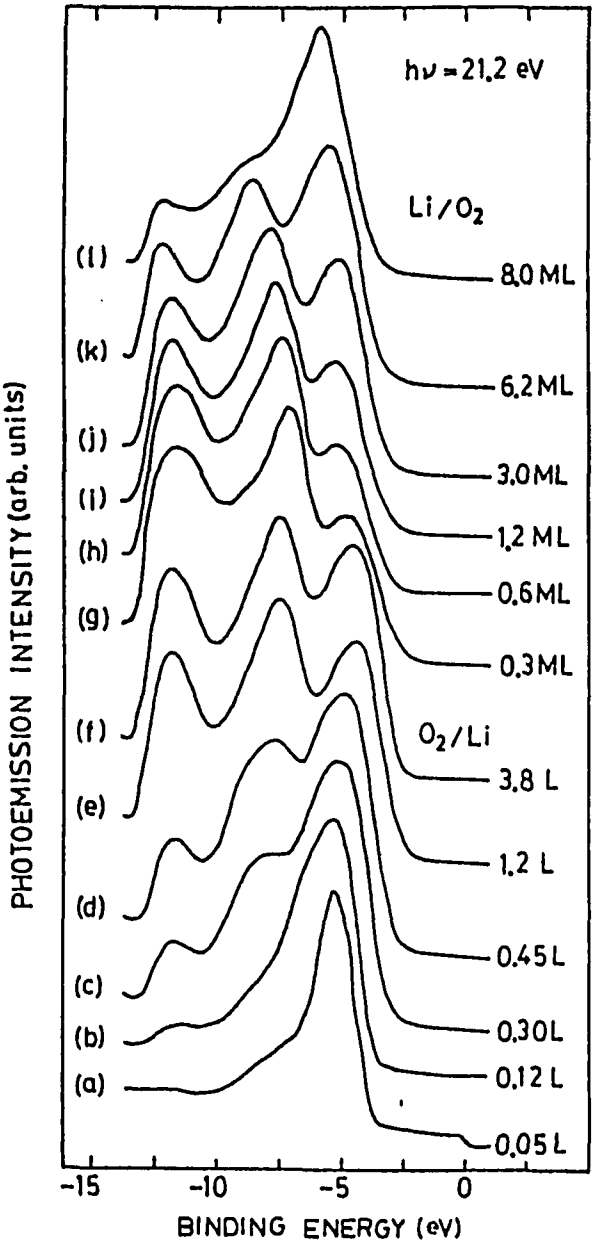

Figure 24. Valence band photoemission spectra of oxygen-lithium system taken at 21.2 eV photon energy.

on lithium peroxide and lithium oxide,[99] which favor the formation of lithium peroxide, because the heats of formation of Li_2O and Li_2O_2 are -143.1 and -151.2 kcal/mol, respectively. This disagreement is probably due to the effect of temperature. At low temperatures, as in our case, oxygen can be easily condensed. It is easy to have a local oxygen-rich region on the Li surface and form Li_2O_2. On the other hand, at room temperature, gas phase O_2 molecules cannot easily adhere to the metal surface, it is hard to have any local oxygen-rich region, and thus most oxygen molecules dissociate and form Li_2O.

As the oxygen exposure is increased, a new peak at about 539 eV in the O 1s region becomes visible (Fig. 23d), which we assign to molecular oxygen. Because the work function of Li is about 2.4 eV, the solid O_2 peak would be about 541.4 eV referenced to the vacuum level. As with Cs and K, there is about 1.7 eV final state screening energy compared with the gas phase O_2 ionization potential (543.1 eV). At the coverage at which the O 1s spectrum shows a significant feature due to solid O_2 (Fig. 23e), molecular oxygen features also dominate in the valence band spectrum (Fig. 24e). Two peaks at 7.5 and 12 eV are due to the molecular O_2 $2p\pi^*$ and $2p\pi$ orbital, respectively. Note that in previous work where solid oxygen is condensed on Al or Ta these levels occur at about 5.5 and 10 eV below E_F.[102,103] The 2 eV shift to higher binding energy in this work is due to the smaller work function of Li and the alignment of the molecule species (O_2) to the substrate vacuum level.

Unlike the case of Cs and K, we did not see superoxide at this point. In order to understand this, we deposited Li onto solid oxygen. In Fig. 23g we show the O 1s spectrum when Li is deposited on solid oxygen. Underlying features are still seen from the substrate, but a new feature appears at 534.5 eV. We identify this feature with the "superoxide" O_2^-

in a LiO_2 complex, noting that this is the most oxygen-rich regime, that is, dilute Li atoms in a "sea" of solid oxygen, and each Li atom donates just one electron to the oxygen molecule. Correspondingly, in the valence band spectra (Fig. 24g and h) a feature at 11.5 eV from E_F developes. The overlapping of this superoxide feature and the solid oxygen feature near 12 eV makes a broad peak around 11.5 eV.

It is seen in Figs. 23 and 24 that more Li deposition leads to a peak again at about 533 eV in the O 1s region (Fig. 23k) and at 7.5 eV in the valence band (Fig. 24k), which indicates that peroxide is formed. Finally, as more Li is deposited, the oxide feature appears at 530 eV in the O 1s spectrum and at about 5.5 eV in the valence band spectrum. At this stage, there are enough electrons transferred from Li to the oxygen layer that the molecules dissociate and Li_2O is formed.

4.2.4. PES Study of Alkali Metal Superoxides

According to our previous experiments,[12,16] the superoxide feature can only be observed in the most oxygen-rich regime. We are interested in the superoxide. Therefore in the experiments discussed here, we evaporated a small amount of alkali metal into a thick layer of solid oxygen which was supported by a Kr film. The Kr film served as a buffer to prevent reaction between the molecular oxygen and the metal substrate.

The valence band and the O 1s core level photoemission spectra of solid oxygen after Cs, K and Li evaporation taken at $h\nu$ = 200 and 650 eV are shown in Figs. 25 and 26, respectively. The spectra of solid oxygen are also shown in Figs. 25 and 26 for reference. The binding energy in Figs 25 and 26 was calibrated to previously reported gas phase O_2 spectra[79] and is referenced to the vacuum level. The lowest binding energy peak in the valence band O_2 spectrum (Fig. 25) is the emission from the antibonding π_g orbital. The

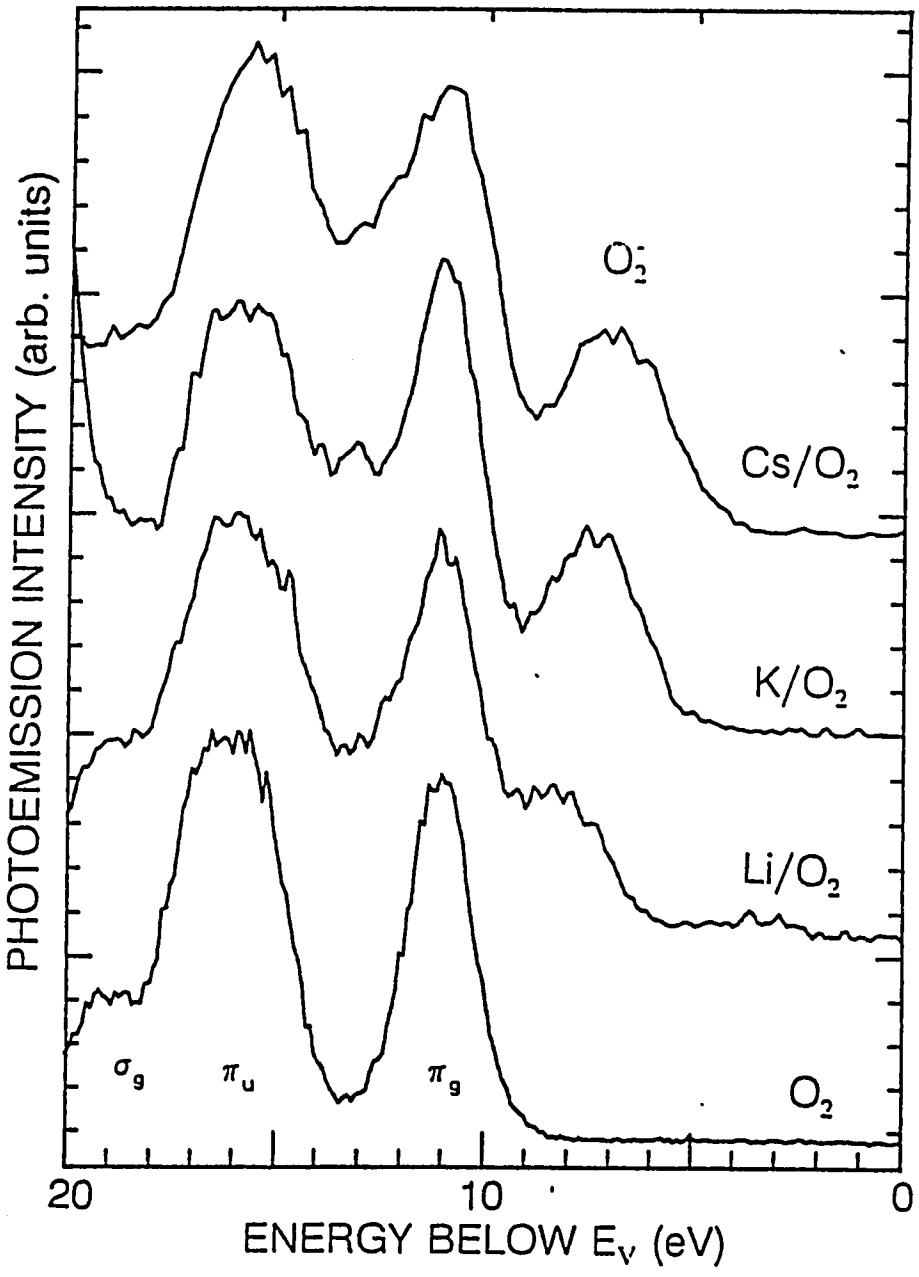

Figure 25. Valence band PES spectra of solid oxygen and alkali metal superoxide complex taken at hν = 200 eV. The binding energy is referenced to the vacuum level and the energy is calibrated by lining up the peak with the gas phase O_2 peak.[79]

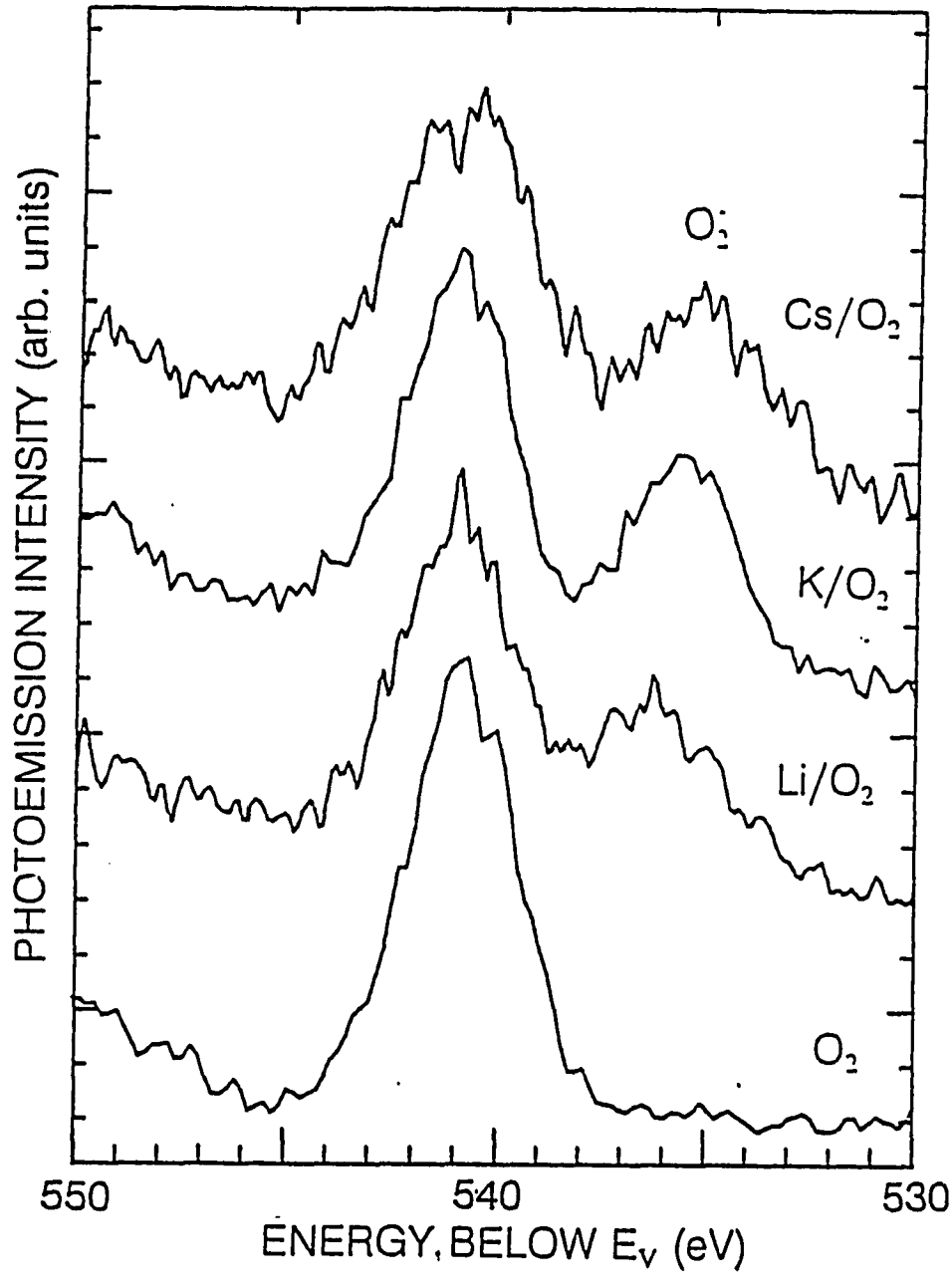

Figure 26. The O 1s PES spectra of solid oxygen and alkali metal superoxide complex taken at hν = 650 eV. The binding energy is referenced to the vacuum level and the energy is calibrated by lining up the peak with the gas phase O_2 peak.[79]

higher binding energy features arise from the bonding π_u orbital and the σ_g orbital, respectively, as indicated in Fig 25.

After deposition of the alkali metal, both the valence band and the core level spectra show a new feature at lower binding energy. From the position of the peak in the O 1s spectrum (Fig. 26),[16] we can deduce that the new feature is due to superoxide. This demonstrates that we can indeed make the pure superoxide by this method.

Figure 25 shows that the separation between the molecular O_2 and superoxide features increase by about 1 eV in the sequence Li, K and Cs. The same trend is seen in the O 1s core level spectra (Fig. 26). Quantitatively, the separation between the solid O_2 feature and the superoxide feature is 2.9, 3.6 and 3.9 eV in the valence band spectrum (Fig. 25), and 4.6, 5.3 and 5.6 eV in the core level spectrum (Fig 26) for LiO_2, KO_2 and the CsO_2 complex, respectively.

A simple charge transfer model predicts that the chemical shift $\Delta E = E_B(O_2) - E_B(O_2^-)$ is proportional to the charge transfer number *n*. The O-O bond in solid O_2 is totally covalent because it is formed by two identical oxygen atoms, so that the charge transfer number is 0, or equivalently the fractional ionic character *f*, is 0. On the other hand, the bond between alkali metal and oxygen in alkali metal superoxides should be largely ionic because of the large electronegativity difference between alkali metals and oxygen. Assuming that the Cs-O bond in CsO_2 is totally ionic, we plot the relation between the fractional ionic character *f* and the chemical shift ΔE in Fig. 27. From this figure and the measured ΔE values, we deduced that the fractional ionic character *f* for LiO_2 and KO_2 is 82% and 95%, respectively. This result is consistent with electronegativity arguments. The Pauling electronegativity of Cs, K and Li is 0.79, 0.82 and 0.98, respectively. In the presence of oxygen, a Cs atom will give up one electron more easily than a K or Li atom,

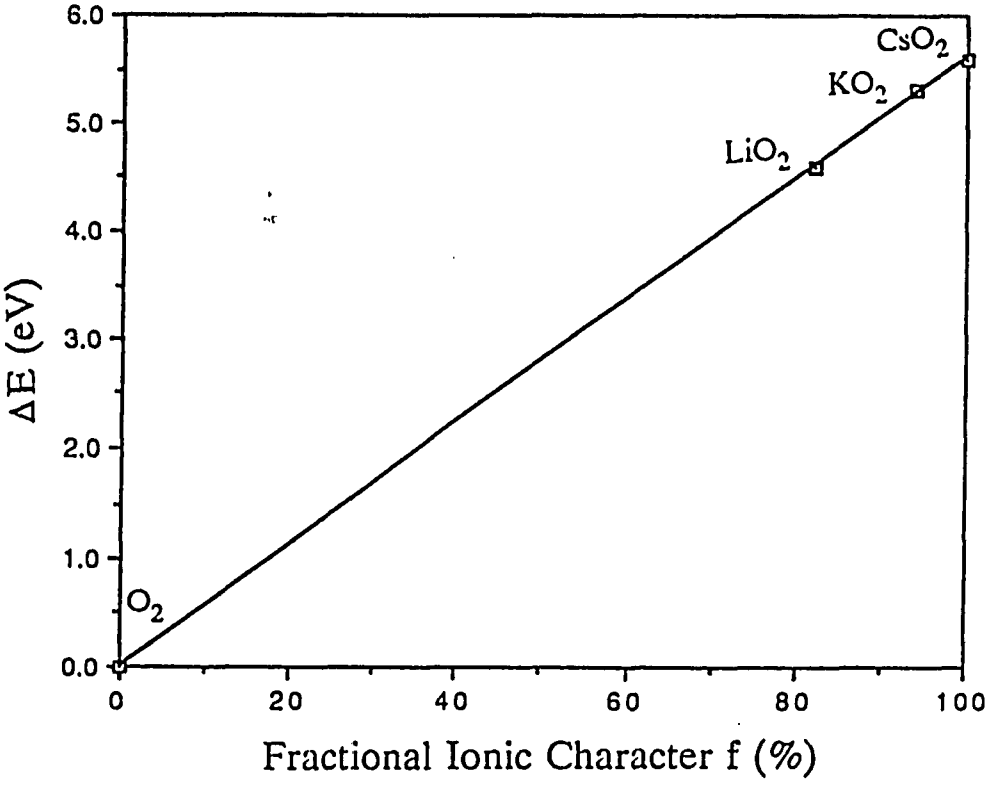

Figure 27. The correlation between the fractional ionic character *f* and the energy separation ΔE. The fractional ionic character of Cs in CsO_2 is assumed to be 100%.

and hence form a more ionic bond. The obtained ionic character also agrees with the results calculated from a semiempirical theory on other alkali compounds, which gives the *f* value of 0.92, 0.94 and 0.96 for LiF, NaCl and RbF, respectively.[104] Because the Pauling electronegativity of fluorine is larger than oxygen the Li-F bond should be more ionic than the Li-O bond.

This result is also supported by the ionic potential (*IP*) argument. The physical basis for the ionic potential is, that cations with a large ionic potential have considerable polarizing power to attract neighboring electrons towards them which induces partial covalence. Consequently, comparison of ionic potentials allows us to make qualitative comparisons of degrees ofcovalence. The ionic potential is defined as[105]

$$IP = \frac{z_c}{r_c} \tag{4.2.7}$$

where z_c is the ion charge expressed as an integral multiple of e, the electron charge, and r_c is the ionic radii. It is known that the average ionic radii for Li^+, K^+ and Cs^+ is 0.68, 1.33 and 1.67 Å, respectively.[105] The *IP* for Li^+, K^+ and Cs^+ is 1/0.68, 1/1.33 and 1/1.67, or 1.47, 0.75 and 0.60. Thus CsO_2 is expected to be more ionic than KO_2 and LiO_2.

It is noted that both solid O_2 and the superoxide features are shifted with the substrate work function and keep the same separation (we did the same experiments on different metal substrates, including Cs, Cu, Fe, K, and Li). This is different from our earlier photoemission experiments, where all the oxygen species except molecule O_2 feature lined up with the substrate Fermi level. This discrepancy is due to the presence of a Kr layer, which blocks the charge transfer between the substrate and the oxygen species.[106]

4.2.5. Summary

In summary, the interaction of solid oxygen with Li, K, and Cs has been studied using photoemission spectroscopy. This study shows that three different oxidation states can coexist at 35 K. Assignment of these features in both O 1s core level and the valence band spectra has been made for O_2^-, O_2^{2-}, and O^{2-} species, which correspond to the formation of superoxide, peroxide, and oxide, respectively. The Cs 3d and the O 1s cross-section ratio obtained from XPS measurements and this assignment quantitatively agrees with the theoretical value. The smaller size of the Li atom makes the initial oxidation of Li significantly different from Cs or K. The observed binding energy of oxide species is at 528.0 eV for K and Cs, while the same feature is at 530.0 eV for Li. In the case of K or Cs, the oxygen atom can penetrate below the metal surface because the large lattice parameter leads to better screening of the oxygen species. On the other hand, in the case of Li, the oxide formed on the surface make it unfavorable for the oxygen to be interstitial in the bulk because of the small Li lattice parameter. The results are summarized in Table 7.

Although the bond between oxygen and alkali metal is almost ionic there is a slight difference in the fractional ionic character for different oxygen-alkali metal bonds. The fractional ionic character deduced from our PES spectra agrees with the calculation from a semiempirical theory.

		Formal Valence Charge of Oxygen Atom	O 1s Peak Position from E_F (eV)
Oxide	Li	-2	530.5
	K		528.0
	Cs		528.0
Peroxide	Li	-1	532.5
	K		532.0
	Cs		532.5
Superoxide	Li	-1/2	534.5
	K		534.5
	Cs		534.5
Solid O_2	Li	0	539.0
	K		539.7
	Cs		540.0

Table 7. Identification of various oxygen and alkali metal complexes.

4.3. NEXAFS and EXAFS Studies of Oxygen and Alkali Metal Systems

4.3.1. Introduction

When diatomic molecules, such as O_2, N_2, CO, or NO, are chemisorbed on metal surfaces, the K-edge absorption spectra are dominated by a bound state transition to an antibonding orbital of π symmetry. This orbital is formed from the unfilled or partially filled 2π molecular orbital and substrate metal states of π symmetry. The intensity of this transition may be expected to be correlated with the details of the metal to molecule (2π) charge transfer.[107,108] As suggested by Blyholder[109], such a charge transfer decreases the intramolecular bond strength leading to an increase of the bond length and to a softening of the intramolecular stretching mode.[110] Previous NEXAFS studies of K-edge absorption spectra of chemisorbed diatomic molecules shown that the energy position of the resonance relative to that observed in the gas phase spectrum can provide valuable information on the charge transfer and the intramolecular bond length upon chemisorption.[43,57]

In this section, we describe our NEXAFS study of alkali metal superoxides. We compare the measured resonance energies to a theoretical calculation.[66] We found that the O-O bond length deduced from the σ^* resonance energy agrees well with previous reports.[14]

4.3.2. NEXAFS Study of Alkali Metal Superoxides

The O 1s K-edge NEXAFS spectra from LiO_2, KO_2 and CsO_2, prepared using the method described in the sample preparation section, are shown in Figure 28. The solid O_2 spectrum is also shown in Fig. 28 for comparison. We emphasize that both XPS and near-edge spectroscopy were done consecutively during the runs when the data shown in Fig. 28 was obtained and the characteristic superoxide core level feature at about 534 eV was observed.

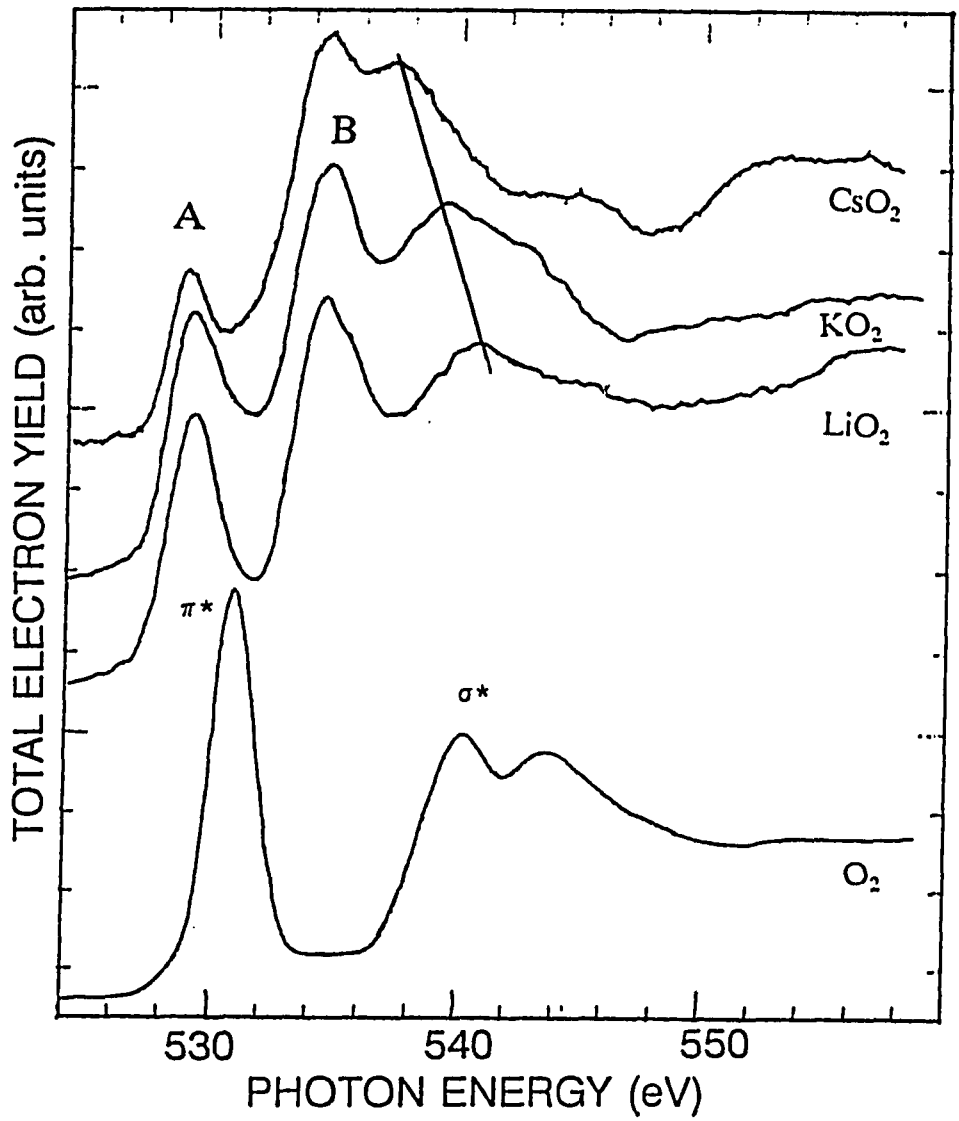

Figure 28. Oxygen K-edge NEXAFS spectra of LiO_2, KO_2 and CsO_2. For comparison, solid O_2 spectrum is also shown. Photon energy was calibrated by lining up the π^* peak with the gas phase O_2 π^* feature.[51]

A.) Assignment of Resonances

The assignment of the K-edge absorption structures in Fig. 28 is facilitated by comparing to the spectrum of solid O_2. Peaks A and B in alkali metal superoxide spectra are assigned to transitions of the O 1s electrons to the π^* and σ^* resonances, respectively. Compared with solid O_2 spectrum, both the π^* and σ^* resonances in the spectra of all three alkali metal superoxides shift to lower photon energy due to the transfer of one electron to the molecular oxygen. The intensity of π^* resonance (peak A) in the superoxides is much smaller than in O_2 because there are fewer unoccupied final states for the 1s - $1\pi_g$ transition in the superoxides. The σ^* resonance (peak B) appears at or near the same photon energy for all of the superoxides examined.

Closer examination of the data for the superoxides shows that the π^* level moves about 1.8 eV to lower photon energy. The shift of the σ^* resonance toward the π^* resonance is relatively large and can be accounted for by the increased occupation of the O_2 $1\pi_g$ (anti-bonding) orbital which weakens the intramolecular bonding. Reducing bond strength results in a longer O-O bond length and causes the $3\sigma_u$ to move closer to the $1\pi_g$ level. For superoxides, we find that the π^* feature is at 529 eV, the σ^* feature is at 534.5 eV and the relative separation of the two levels is 5.5 eV. These values are comparable to those reported by Wurth *et al.*[59] for O_2 on Pt(111) which were 530, 535 and 5.5 eV, respectively.

Fig. 28 also shows a third feature (peak C) further from the oxygen absorption edge which varies significantly in going from one alkali metal to another. This feature moves toward the σ^* peak as one goes from Li to Cs. This feature is not a shape resonance because the O-O bond length does not change much in going from LiO_2 to CsO_2 and the π^* and σ^* peaks do not move as would be expected if the O-O bond expanded or

contracted. We suggest these peaks are related to the electronic structure of the metal component of the superoxide, specifically the conduction band edge as is seen in other metal oxides.[111] If we assign this peak to the onset of transitions to the conduction band (sp band) of the alkali superoxides, the band gap is given by the distance of the π^* feature A to feature C: 12, 10, and 9.5 eV for Li, K, and Cs superoxide, respectively. These numbers are close to the band gaps of the corresponding alkali fluorides.[112] A study of the unoccupied states of NaO_2 and KO_2 by Bertel *et. al.* also shows states around 10 eV in the inverse photoemission spectra and in the alkali edges.[15] This leads to a natural explanation of why this peak is absent for O_2 on Pt(111).[59] This feature would not be seen because this feature would be near the Fermi level for a metal and overlap with the π^* resonance.

B.) Resonance Position and Molecular Bond Length

The similarity between the superoxide and solid O_2 spectra indicates that the superoxide spectra must be dominated by intramolecular excitations and that the molecule-metal interaction has little influence on the K-edge resonance structures, apart from changing the resonance energy position due to the change of the molecular bond length.

Compared with the neutral O_2 molecule, there is one more electron in the antibonding π_g orbit in the superoxide ion O_2^-, which has a $\sigma_g^2\pi_u^4\pi_g^3$ ground state configuration. One effect of the additional antibonding electron is an increase in the O-O bond length in the O_2^- ion relative to the O_2 molecule. Blyholder[109] first suggested that the metal $d\pi$ to adsorbate 2π charge transfer results in a strengthening of the metal-adsorbate bond but weakens the intramolecular bond. This is intuitively clear since the 2π orbital is an antibonding orbital for O_2 but is a bonding orbital for metal-O bond.

As mentioned earlier, the energy position of the final state shape resonance is directly sensitive to the intramolecular bond length. Experiments have been confirmed that

there is a simple linear correlation between the σ^* resonance position and the intramolecular bond length for gas phase molecules.[57] It was found that a 1 eV shift in the resonance energy corresponds to about 0.03 Å O-O bond length change.[113]

The energy of the σ^* resonance for all three alkali metal superoxides is at 534.5 eV, as shown in Fig. 28. Compared with the solid O_2 spectrum, the σ^* resonance shifts about 5.2 eV to lower photon energy. Using the relation $\Delta R = 0.03$ Å/eV and taking the O-O bond length in solid O_2 as 1.207 Å, we obtained an O-O bond length of 1.36 Å in these alkali metal superoxides. This value is in excellent agreement with the previously reported value of 1.35 Å for NaO_2 and KO_2.[14] This value is also in agreement with the recently published 1.37 Å O-O distance in Pt superoxide.[59] This result indicates that the O-O bond length in O_2^- species is relatively insensitive to the cation ions.

Figure 29 plots the result of the calculated energy shift ΔE verses the inverse of the O-O bond length in O_2^- species. The theoretical calculations for O_2^- were performed by Dunlap,[66] using the same method as described in Chapter 3 for O_2, except that one more electron is put into the π^* orbital. After using the same normalization procedure used for O_2 (Chap. 3), the calculated π^* energy level (528.9 eV) for O_2^- with a 1.34 Å O-O bond length is in very good agreement with the experimental value of 529.0 eV. Convergence problems hampered accurate computation of the position of the σ^* resonance for $R \leq 1.34$ Å and this value was extrapolated from longer internuclear distances (Fig. 29). After doing this, we predict the σ^* resonance should be at 533.5 eV, which is in agreement with the observed σ^* resonance energy at 534.5 eV.

There is also another way to judge the quality of the calculation, namely, using the experimental ΔE value and the plot (Fig. 29) to get the O-O bond length and comparing it with the experimental data. By doing this, we predict the O-O bond length should be 1.31

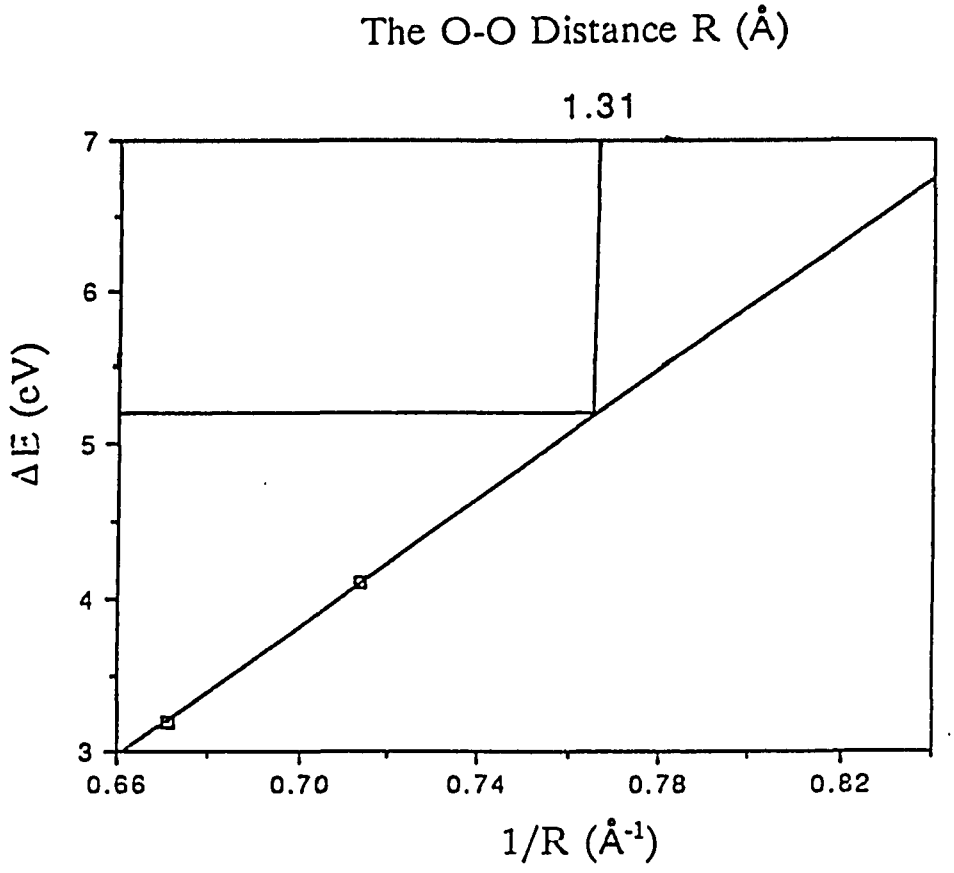

Figure 29. The correlation between the calculated energy separation ΔE and the inverse of the O-O bond lengths (1/R) for O_2^- ion.

Å for O_2^-, which is in good agreement with the previously reported value of 1.35 Å O-O bond length for NaO_2 and KO_2.[14]

It is worth pointing out that the observation that the energy difference between the π^* and the σ^* resonances is almost the same for all three alkali metal superoxides (Fig. 28), is surprising on the basis of our previous ionic character discussions. As mentioned before, one electron charge roughly corresponds to about 1 eV shift for the π^* peak and about 5 eV for the σ^* peak. Using this relation and previous ionic character results of LiO_2 (82%), KO_2 (95%) and CsO_2 (100%), we should see about 0.8 eV difference between the π^* and σ^* spacing in the lithium and cesium superoxide spectra. However, this is not observed in the experiments, as shown in Fig. 28. A possible explanation could be due to the different atomic size of the two atoms. For example, although a Li atom transfers less charge to the oxygen molecule than a Cs atom, because of the much smaller atomic size, the Li atom can get closer to oxygen and form a shorter metal-oxygen bond. This is found in the alkali halide crystals. For example, the bond length and cohesive energy in LiCl, NaCl, KCl, and RbCl are 2.570 (198.9), 2.820 (182.6), 3.147 (165.8), and 3.445 Å (159.3 kcal/mol), respectively.[114] This provides a situation where the O-O bond could be disturbed more in LiO_2 than in CsO_2, and thereby results in an addition to the O-O bond length in LiO_2 compared to CsO_2. , Since the σ^* resonance energy is inversely proportional to the intramolecular bond length, the longer O-O bond will shift the σ^* peak to lower energy, and thus could explain the 0.8 eV discrepancy. These results then suggest that there are some refinements to the conventional ideas relating the σ^* position to charge transfer in molecules.[113] We also mention that due to less charge transfer, the core hole screening is reduced in LiO_2 after photon excitation, and this can also shift the σ^* peak to lower energy.

In summary, alkali metal superoxides have been studied by x-ray absorption

spectroscopy. Three features are observed in NEXAFS spectra. The first two peaks in the spectra are due to intra-molecular transitions (1s to the π^* and σ^* transitions), the positions of these two peaks can be well described by a first principles calculation for the free O_2^- ion. The third peak is due to extra-molecular transitions (1s to the alkali sp band transitions). We see no evidence of magnetic effects in the spectra and argue they are too small to be seen in near edge data obtained using modest resolving power. The fact that the oxygen K edge spectra of alkali metal superoxides are in good agreement with theoretical calculations for the free O_2^- ion, indicates that previous core level O_2^- feature assignment is right.

4.3.3. NEXAFS Study of the Solid Oxygen on Cesium

We now describe our NEXAFS experimental results. In Fig. 30 we present the measured O K-edge NEXAFS spectra of O_2/Cs for different oxygen exposures. The number in Fig. 28 indicates the oxygen exposure in langmuirs.

For the clean Cs film, there is of course no feature in the O K-edge region. Small oxygen exposure (0.6 L) leads to an edge jump at about 530 eV photon energy, which is a common feature of metal oxides.[111] As explained from our photoemission results described before, the oxide feature is the dominant feature at the early oxidation stage.

As oxygen exposure increases (3.6 to 10 L), a new peak P appears at about 531 eV. We discuss several possibilities for this feature: one might think that this peak is the π^* resonance feature in molecular O_2 since this peak appears at almost the same energy. However, molecular O_2 should have two peaks at around 540 eV. Thus peak P is not the π^* resonance feature of molecular O_2. Next, we consider the possibility that peak P is due to superoxide. As mentioned before, there is one more electron in the antibonding π_g orbital in superoxide (O_2^-) than in neutral O_2, resulting in a $\sigma_g^2\pi_u^4\pi_g^3$ ground state configuration. Because the π_g orbital is still partially filled in O_2^-, we should see both π^* and σ^* resonance in the spectrum, and this is what we saw in superoxide spectra (Fig. 28). Comparing with Fig. 28, it is obvious that peak P is not the superoxide feature.

Finally, we consider the possibility that peak P is due to peroxide O_2^{2-}. In O_2^{2-} two electrons are transferred to one oxygen molecule, resulting in a filled π_g orbital. Hence, one expects to see only the σ^* resonance in the spectrum. Because there is one more electron in the antibonding π_g orbital in peroxide than in the O_2^- species, the O-O bond strength must be weaker in the former species than in the later, so that the peroxide should have a longer O-O distance. Consequently, the σ^* resonance should shift to lower photon energy

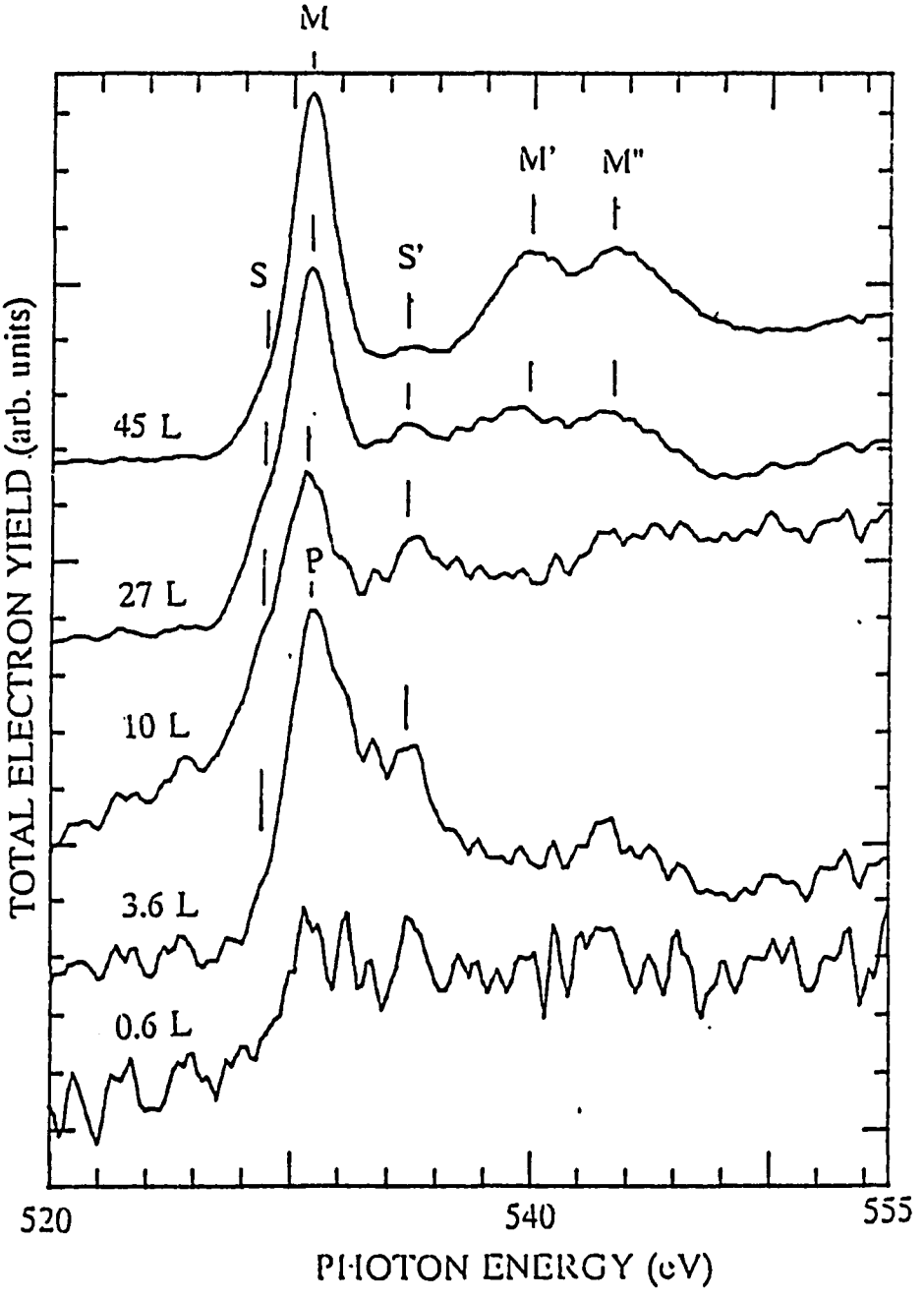

Figure 30. Total electron yield (TEY) oxygen K-edge NEXAFS spectra of solid O_2/Cs system for various oxygen exposures at 25 K.

relative to the superoxide.

All these features are reflected in peak P. In particular, the expanded bond length is clearly borne out by the shift of the σ^* resonance energy from 534.5 eV in O_2^- (Fig. 28) to 531 eV in O_2^{2-}. The 531 eV σ^* resonance energy is in good agreement with the published 532.6 eV σ^* resonance energy in the NEXAFS spectrum of O_2/Ag(110), in which this peak was assigned to a singly bonded peroxide species.[113] Especially, the fact that 1.46 Å O-O bond length obtained from this shift is in excellent agreement with the reported value of 1.47 Å in Ag peroxide,[113] makes us believe that peak P is the σ^* resonance. Thus we assign peak P to the transition from the O 1s to the σ orbital in O_2^{2-}.

As O_2 exposure increases, two shoulders appear at 529 and 534.5 eV. On the basis of our previous results on superoxides, we know that these two peaks are due to transitions to π^* and σ^* molecular orbitals in Cs superoxide (CsO_2). These superoxide features are indicated in Fig. 30 by letter S and S'. It is apparent that peaks S and S' increase in intensity relative to the peak P as the oxygen exposure is increased. This is expected since the sample surface becomes more oxygen-rich. The same phenomena has also been observed in photoemission measurements.

At high oxygen coverage (27 and 45 L), two new features (M' and M") appear at around 540 eV, which is characteristic of molecular O_2.[51] Although the underlying features can still be seen, we can unambiguously assign peaks M, M' and M" to transitions to the π^* and σ^* orbitals, and Rydberg states of molecular O_2, respectively. Notice that the superoxide features (S and S') decrease in intensity relative to the O_2 features when increasing O_2 exposure. Close examination of the data shows that the intensity ratio decreases by about a factor of 2 when the O_2 exposure is doubled, which is similar to our photoemission results.

It is difficult to observe what happens to the peroxide features because they coincide in energy with the O_2 π^* feature. However, from our photoemission study we know that the intensity of peroxide peak decreases when the molecular O_2 peak increases. Therefore, at high oxygen coverage, the 531 eV peak is prominently due to the π^* resonance of molecular O_2.

In conclusion, the interaction of solid oxygen with cesium has been studied using NEXAFS spectroscopy. Various oxygen ionic states were found during the oxidation process. The results obtained from the NEXAFS study are consistent with previous PES observations. The O-O bond length in the peroxide and in the superoxide complexes deduced from the position of the σ^* resonance are in good agreement with previously reported values.

4.3.4. EXAFS Measurement on Cesium Superoxide

In order to determine the bonding length in the superoxide complex, the total electron yield EXAFS spectrum at O K-edge in CsO_2 has been measured. The raw data is shown in Figure 31a, the monochromator output is shown in Fig. 31b, and the normalized spectrum is displayed in Fig. 31c.

The pre-edge and above edge background is approximated by fitting the pre-edge and above edge with two lines. After removing the background, the spectrum is then normalized to the edge jump and presented in Fig. 32a, where the smooth atomic absorption μ_0 is obtained by fitting the high energy part of the spectrum with a polynomial function. The fine structure oscillations $\chi(k)$ are given

$$\chi(k) = \frac{\mu(k) - \mu_0(k)}{\mu_0(k)}, \qquad (4.3.1)$$

The $\chi(k)$ is shown in Fig. 32b, where the $\chi(k)$ is multiplied by a factor of k^3.

The Fourier transform over a limited wave vector k range between 2 and 6 $Å^{-1}$ is plotted in Fig. 32c. In the CsO_2, the nearest neighbor of oxygen is O, and the second neighboring atoms are cesium cations. Two peaks appear at 1.3 and 2.7 Å in the transform corresponding to the intramolecular O-O bond length and O-Cs distance, respectively. Taking into account the limited wave vector k range and our limited knowledge about the phase, these results are in agreement with the measured 1.32-1.35 Å O-O bonding length, 2.71-2.92 Å O-Na and O-K distances in NaO_2 and KO_2 by x-ray diffraction.[115] The value of 1.3 Å O-O bond length is also in agreement with our NEXAFS result.

It can be seen that the amplitude of peak A is much smaller than peak B, which is expected from a simple theory. Since the backscattering amplitude $F(k)$ in Eq. (2.6.2) is proportional to the atomic number Z, the backscattering amplitude from Cs atoms (Z = 55)

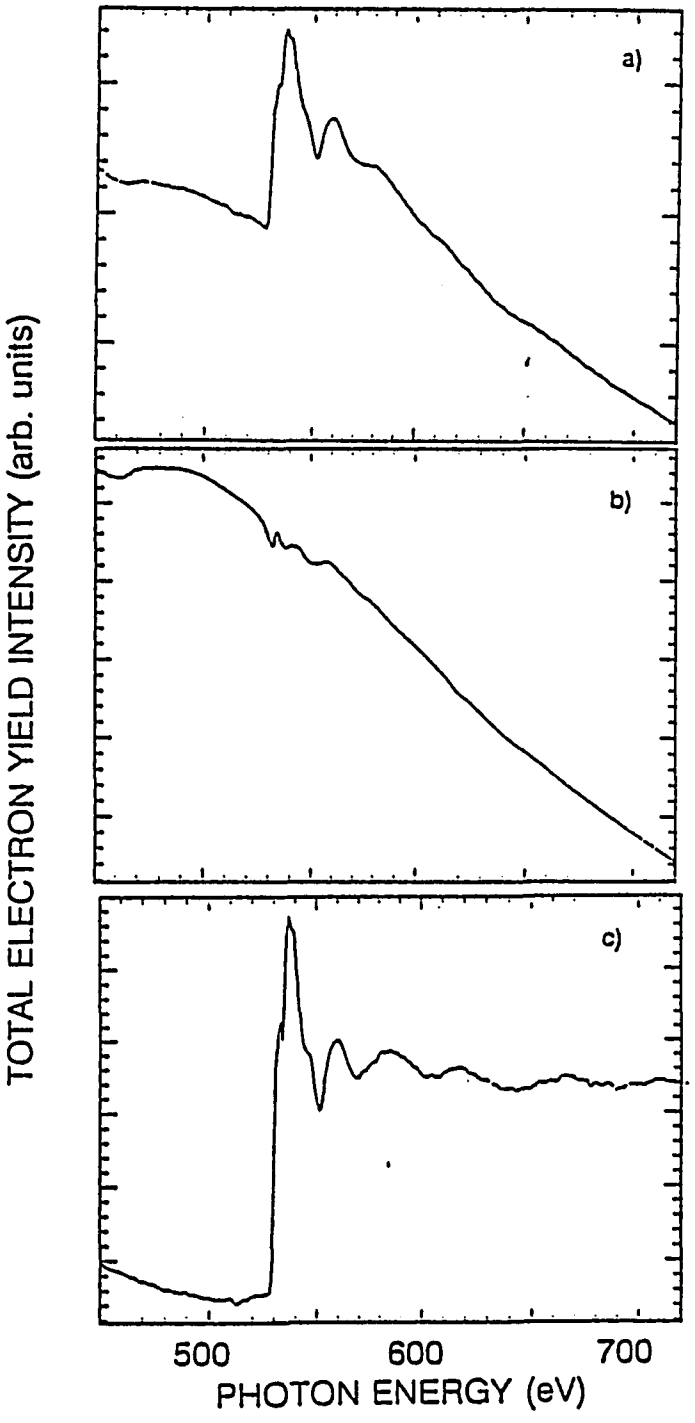

Figure 31. (a) The O K-edge EXAFS spectrum of CsO_2 measured at 20 K, (b) The monochromator output, and (c) The normalized EXAFS spectrum.

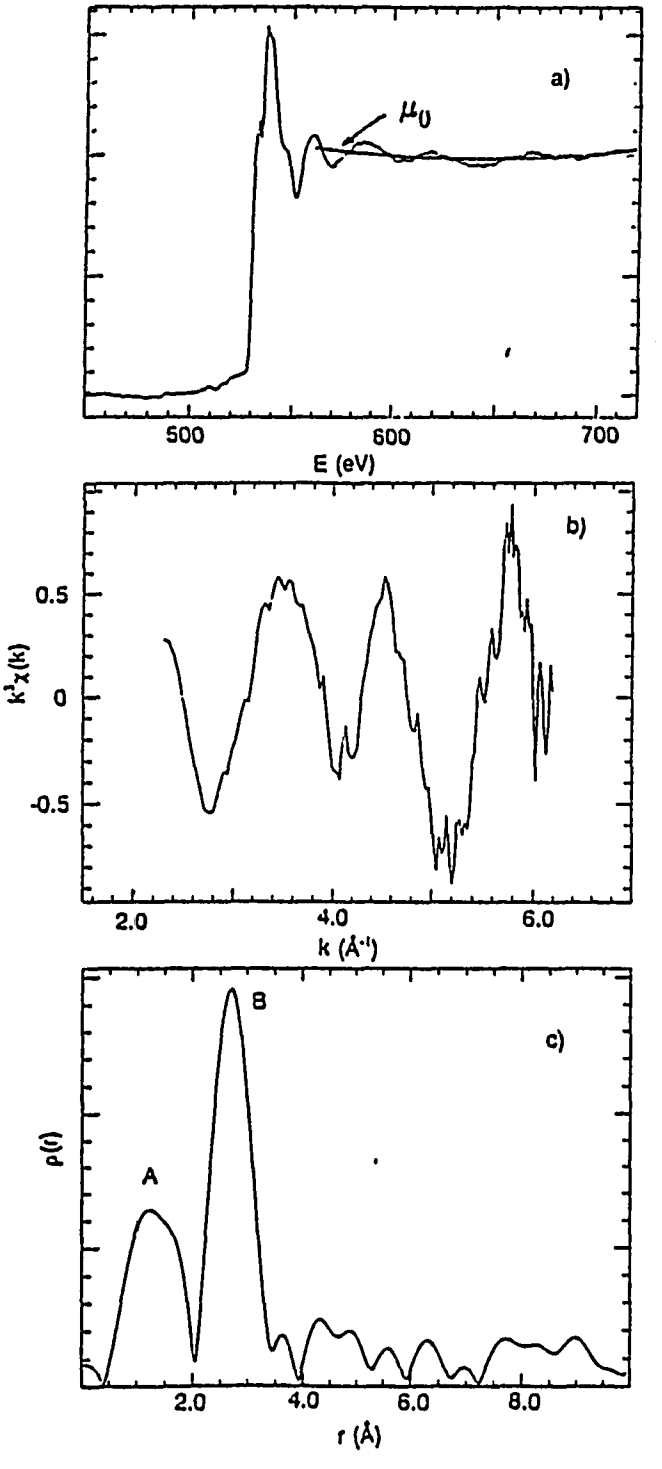

Figure 32. (a) Edge normalized spectrum, the curve $\mu_0(E)$ is the best fit to the experimental curve. (b) EXAFS ($k^3\chi(k)$) in k-space, where $\chi(k)$ is defined in equation (2.6.3). (c) the Fourier transformed experimental data in r-space.

should be much larger than that from O atoms (Z = 8).

In conclusion, the EXAFS study of CsO_2 has been carried out by total electron yield measurements. The computed O-O bonding length and O-Cs distance are in good agreement with previous x-ray measurements on alkali metal superoxides[115] and are also consistent with theoretical calculations.[66]

Chapter 5. Summary

In summary, the molecular bond, electronic structure, oxidation state, and ligand field of solid oxygen/alkali metal systems have been studied by several spectroscopic techniques: Extended X-ray Absorption Fine Structure (EXAFS) spectroscopy, Near-Edge X-ray Absorption Fine Structure (NEXAFS) spectroscopy, Auger Electron Spectroscopy (AES), X-ray Photoelectron Spectroscopy (XPS) and Ultraviolet Photoelectron Spectroscopy (UPS).

In the study of the K-edge NEXAFS spectrum of solid oxygen, three main features are assigned to the π^*, σ^* resonance, and the Rydberg states, respectively. This assignment is supported by Xα calculations and high resolution NEXAFS measurements on gas phase O_2. Compared with the gas phase spectrum, Rydberg states shift about 1.5 eV to a higher photon energy, which we argue is due to the increased dielectric constant in the solid. The Auger spectra of both ionized (2 hole final state) and excited (2 hole and 1 electron final state) molecules in solid O_2 shift to higher kinetic energy relative to the gas phase spectra. The shifts are 10 and 2 eV, respectively. These shifts are explained in terms of solid state final state screening effects. PES studies of the interaction between solid oxygen and alkali metal show that three different oxidation states can coexist at 35 K. Assignments of these features in both O 1s core level and valence band spectra have been made for O_2^-, O_2^{2-}, and O^{2-} species, which correspond to the formation of superoxide, peroxide and oxide, respectively. The Cs 3d and the O 1s cross-section ratio obtained from XPS measurements and this assignment quantitatively agree with the theoretical value.

We also studied LiO_2, KO_2, and CsO_2 superoxides using NEXAFS, PES, and EXAFS measurements. Compared with the solid O_2 NEXAFS spectrum, both π^* and σ^*

resonances in the NEXAFS spectra of all three alkali metal superoxides shift to a lower photon energy due to the transfer of one electron to the molecular oxygen. The shift are 1.8 eV and 5.5 eV, respectively. These shifts are in excellent agreement with the *ab initio* calculated results for free O_2^- ion. This indeed shows that the metal-oxygen bond in alkali superoxides is very ionic and our core level O_2^- feature assignment is right. The O-O bonding lengths in superoxides and peroxide deduced from the position of the σ^* resonance agree well with the previously reported O-O distance in NaO_2 and KO_2 superoxides and in Ag peroxide. In the EXAFS study of cesium superoxide (CsO_2), the computed O-O and O-Cs distances from the EXAFS spectra are also in good agreement with previous x-ray diffraction measurements on NaO_2 and KO_2.

Appendix A

Publications

1. X-Ray Absorption studies of $Nd_{2-x}Ce_xCuO_4$, Phys. Rev. B **42**, 4763 (1990), A. Krol, C.S. Lin, Z.H. Ming, C.J. Sher, Y.H. Kao, C.L. Lin, S.L. Qiu, J. Chen, J.M. Tranquada, M. Strongin, G.C. Smith, Y.K. Tao, R.L. Meng, P.H. Hor, C.W. Chu, Gang Cao and J.E. Crow.

2. Auger and X-ray Absorption Studies of Solid Molecular Oxygen, J. Vac. Sci. and Tech. **A8**, 2591 (1990), Jie Chen, C.L. Lin, S.L. Qiu, M. Strongin and M. denBoer.

3. The Formation of Metal-Oxygen Species at Low Temperatures, J. Vac. Sci. and Tech. **A8**, 2595 (1990), S.L. Qiu, C.L. Lin, Jie Chen and M. Strongin.

4. Photoemission Studies of the Low Temperature Reaction of Metals and Oxygen, Phys. Rev. B **41**, 7467 (1990), S.L. Qiu, C.L. Lin, Jie Chen and M. Strongin.

5. On the Question of Superoxide in La_2CuO_{4+x}, Phys. Rev. B **41**, 7238 (1990), M. Strongin, S.L. Qiu, J. Chen, C.L. Lin and E.M. McCarron.

6. Photoemission and Oxygen K-edge Absorption Studies of $Ba(Pb,Bi)O_3$, Phys. Rev. B **39**, 9607 (1989), C.L. Lin, S.L. Qiu, J. Chen, M. Strongin, G. Cao, C.S. Jee and J.E. Crow.

7. The Interaction of Li with Solid Oxygen, Phys. Rev. B **39**, 6194 (1989), S.L. Qiu, C.L. Lin, J. Chen and M. Strongin.

8. Photoemission Study of the Growth and Modification of the Al/Ta (110) Interface, Phys. Rev. B **39**, 5591 (1989), D.Di Marzio, M.W. Ruckman, S.L. Qiu, L. Jiang, J. Chen and M. Strongin.

9. Identification of Oxygen Related Species in the XPS and Near-edge and Studies of High T_c Superconductor, Physica **C162-164**, 1325 (1989), C.L. Lin, S.L. Qiu, Jie. Chen, J.M. Tranquada, M. Strongin, J.E. Crow and C.W. Chu.

10. Interaction of H_2O with a High Temperature Superconductor, Phys. Rev. B **37**, 3747 (1988), S.L. Qiu, M. Ruckman, N.B. Brooks, P.D. Johnson, J. Chen, C.L. Lin, M. Strongin, B. Sinkovic, J.E. Crow and C.S. Jee.

11. Interaction of CO, CO_2, and H_2O with Ba and $YBa_2Cu_3O_{6+x}$, AIP Proc. **No.82**, 83 (1988), S.L. Qiu, C.L. Lin, M. Ruckman, J. Chen, D.H. Chen, Y.W. Xu, A.R. Moodenbaugh, M. Strongin, D. Nichols and J.E. Crow.

12. The Electronic Structure of $YBa_2Cu_3O_{6+x}$ Above and Below T_c, AIP Conf. No.165, 245 (1988), S.L. Qiu, M. Ruckman, P.D. Johnson, J. Chen, L. Jiang, C.L. Lin, M. Strongin, B. Sinkovic and N. Brooks.

13. SEM Study of Interface in GaInP/GaAs, J. Chinese Electron Microscopy Society. Vol.3, No.4, 91 (1984), Jie Chen, G.Z. Lu and J.G. Liang.

14. to Photoemission and Oxygen K-edge Studies of Metals with Oxygen, Presented and be published in the Proc. of 36th Avs Conf. Oct. 23-27, 1989, Boston, C.L. Lin, J. Chen, S.L. Qiu and M. Strongin.

15. XPS and XAS Studies of $YBa_2Cu_3O_{6+x}$, $La_{2-x}Sr_xuO_4$ and $Nd_{2-x}Sr_xCuO_4$, Presented and to be published in the Proc. of 36th AVS Conf. Oct. 23-27, 1989, Boston, C.L. Lin, S.L. Qiu, J. Chen, M. Strongin, J.E. Crow and C.W. Chu.

16. Near-edge Study of Molecular Oxygen and Nitrogen on Solid Krypton, M.W. Ruckman, S.L. Qiu, J. Chen and Myron Strongin, (submitted to Phys. Rev.).

References

1. A.H. Sommer, *Photoemissive Materials*, (Wiley, New York, 1968).

2. N.-G. Vannerberg, Prog. Inorg. Chem. **4**, 125 (1962).

3. Neville V. Smith and William E. Spicer, Phys. Rev. **188**, 593 (1969).

4. Paul E. Gregory, Patrick Chye, Hideo Sunami and W.E. Spicer, J. Appl. Phys. **46**, 3525 (1975).

5. S.P. Bernardell, Ph.D. thesis (University of Rhode Island, 1971).

6. A. Simon, Naturwissenschaften **53**, 622 (1971).

7. Chung-Yi Su, I. Lindau and W.E. Spicer, Chem. Phys. Lett. **87**, 523 (1982).

8. G. Ebbinghus and A. Simon, Chem. Phys. **43**, 117 (1980).

9. C. Wijers, M.R. Adriaens and B. Feuerbacher, Surf. Sci. **80**, 317 (1979).

10. L.G. Petersson and S.E. Karlsson, Phys. Scr. **16**, 425 (1977).

11. M.L. Shek, Xiaohe Pan, Myron Strongin and M.W. Ruckman, Phys. Rev. B **34**, 3741 (1986).

12. S.L. Qiu, C.L. Lin, J. Chen and Myron Strongin, Phys. Rev. B **39**, 6194 (1989).

13. B. Woratschek, W. Sesselmann, J. Küppers, G. Ertl and H. Haberland, J. Chem. Phys. **86**, 2411 (1987).

14. E. Bertel, F.P. Netzer, G. Rosina and H. Saalfeld, Phys. Rev. B **39**, 6082 (1989).

15. E. Bertel, N. Memmel, W. Jacob, V. Dose, F.P. Netzer, G. Rosina, G. Rangelov, G. Astl, N. Rösch, P. Knappe, B. I. Dunlap and H. Saalfeld, Phys. Rev. B **39**, 6087 (1989).

16. S.L. Qiu, C.L. Lin, J. Chen and Myron Strongin, Phys. Rev. B **41**, 7467 (1990).

17. VSW Scientific Instruments Ltd. Warwick Road South, Old Trafford, Manchester M16 0JT, England.

18. K.D. Sevier, *Low Energy Electron Spectroscopy*, (Wiley-Interscience, New York, 1972).

19. D. Roy and J.D. Carette, *Electron Spectroscopy for Surface Analysis, Topics in Current Physics, Vol. 4*, (Springer, Berlin, Heidelberg, New York, 1977).

20. M.W. Ruckman, S.L. Qiu and Myron Strongin, Rev. Sci. Instrum. **62**, (1991).

21. John F. O'Hanlon, *A User's Guide to Vacuum Technology*, (John Wiley & Sons, 1980).

22. A. Roth, *Vacuum Technology*, (North-Holland, 1982).

23. Air Products and Chemicals Inc. Allentown, PA.

24. T.N. Rhodin and J.W. Gadzuk, in *The Nature of the Surface Chemical Bond*, (Amsterdam: North-Holland 1979).

25. D.R. Penn, Phys. Rev. B **13**, 5248 (1976).

26. A. Rosén and I. Lindgren, Phys. Rev. **176**, 114 (1968).

27. A. Barrie, Chem. Phys. Lett. **19**, 109 (1973).

28. P. Auger, Compt. Rend. **180**, 65 (1925).

29. L.E. Davis, N.C. MacDonald, P.W. Palmberg, G.E. Riach and R.E. Weber, *Handbook of Auger Electron Spectroscopy*, (Physical Electronics Inc. Eden Prarie, Minn, 1976).

30. J. Stöhr, Z. Phys. **B61**, 439 (1985).

31. B.K. Teo and D.C. Joy, *EXAFS Spectroscopy*, (Plenum, New York, 1981).
A. Bianconi *et al, EXAFS and Near Edge Structure*, (Springer-Verlag, Berlin, 1983).

32. P.A. Lee and G. Beni, Phys. Rev. B **15**, 2862 (1977).

33. C.A. Ashley and S. Doniach, Phys. Rev. B **11**, 1279 (1975).

34. E.A. Stern, D.E. Sayers, and F.W. Lytle, ibid. **11**, 4836 (1975).

35. A. Erbil, G.S. Cargill III, R. Frahm and R.F. Boehme, Phys Rev. B **37**, 2450 (1988).

36. J. Stöhr, C. Noguera and T. Kendelewicz, Phys. Rev. B **30**, 5571 (1984).

37. J. Stöhr, R. Jaeger, J. Feldhaus, S. Brennan, D. Norman and G. Apai, Appl. Opt. **19**, 3911 (1980).

38. D. Denley, P. Perfetti, R.S. Williams, D.A. Shirley and J. Stöhr, Phys. Rev. B **21**, 2267 (1980).

39. I. Lindau and W.E. Spicer, J. Electron Spectrosc. Relat. Phenom. **3**, 409 (1974).

40. J. Stöhr, K. Baberschke, R. Jaeger, R. Treichler and S. Brennani, Phys. Rev. Lett. **47**, 381 (1981).

41. J. Stöhr, D.A. Outka, K. Baberschke, D. Arvanitis and J.A. Horsley, Phys. Rev. B **36**, 2976 (1987).

42. J. Stöhr, F. Sette and A.L. Johnson, Phys. Rev. Lett. **53**, 1684 (1984).

43. F. Sette, J. Stöhr, and A.P. Hitchcock, Chem. Phys. Lett. **110**, 517 (1984).

44. J. Stöhr and R. Jaeger, Phys Rev. B **26**, 4111 (1985).

45. Herman Winik and S. Doniach, *Synchrotron Radiation Research*, (Plenum Press, New York and London, 1980).

46. C. Kunz, *Synchrotron Radiation*, (Springer-Verlag, Berlin Heidelberg New York, 1979).

47. H. Peterssen, Nucl. Instr. and Meth. **A246**, 260 (1986).

48. C.T. Chen, E.W. Plummer, and M.R. Howells, Nucl. Instrum. Meth. **222**, 103 (1984).

49. D.L. Ederer, Nucl. Instrum. Meth. **195**, 191 (1982).

50. G.R. Wight and C.E. Brion, J. Electron Spectrosc. and Relat. Phenom. **4**, 313 (1974).

51. A.P. Hitchcock and C.E. Brion, J. Electron Spectrosc. and Relat. Phenom. **18**, 1 (1980).

52. R. Rosenberg, P.J. Love, P.R. LaRoe, V. Rehn and C.C. Park, Phys. Rev. B **31**, 2634 (1985).

53. Chi-Chang Kao, Steven L. Hulbert and Erik D. Johnson, BNL-42689, Informal Report, 1989.

54. D.W. Turner *et al, Molecular Photoelectron Spectroscopy*, (Wiley, London, 1970).

55. F. Sette, J. Stöhr and A.P. Hitchcock, J. Chem. Phys. **81**, 4906 (1984).

56. J. Stöhr, J. L. Gland, W. Eberhardt, D. Outka, R. J. Madix, F. Sette, R. J. Koestner and U. Doebler, Phys. Rev. Lett. **51**, 2414 (1983).

57. J. Stöhr and D.A. Outka, Phys. Rev. B **36**, 7891 (1987).

58. R.A. Rosenberg, P.R. LaRoe, Victor Rehn, J. Stöhr, R. Jaeger and C.C. Parks, Phys. Rev. B **28**, 3026 (1983).

59. W. Wurth, J. Stöhr, P. Feuler, X. Pan. K.R. Bauchapiess, Y. Baba, E. Hudel, G. Racker and D. Menzel, Phys. Rev. Lett. **65**, 2426 (1990).

60. H. Petersen, A. Bianconi, F.C. Brown and R.Z. Bachrach. Chem. Phys. Lett. **58**, 263 (1978).

61. C. T. Chen, Y. Ma and F. Sette, Phys. Rev. A **40**, 6737 (1989).
Y. Ma, C.T. Chen, G. Meigs, K. Randall and F. Sette, to be published.

62. C.S. Barrett, L. Meyer and J. Wasserman, J. Chem. Phys. **47**, 592 (1967).

63. Roger L. Dekock and Harry B. Gray, *Chemical Structure and Bonding.*

64. V.N. Akimov, A.S. Vinogradov and T.M. Zimkina, Opt. Spectrosc. (USSR), **53**, 63 (1982).

65. M.W. Ruckman, S.L. Qiu, J. Chen and Myron Strongin, Phys. Rev. B **43**, 8603 (1991).

66. B.I. Dunlap, private communication.

67. B. I. Dunlap, P. A. Mills and D. E. Ramaker, J. Chem. Phys. **75**, 300 (1981).

68. J. Y. Roncin, J. Mol. Spectrosc., **26**, 105 (1968).

69. Jie Chen, C.L. Lin, S.L. Qiu, Myron strongin and M.L. denBoer, J. Vac. Sci. Technol. **A8**, 2591 (1990).

70. B.P. Tonner, C.M. Kao, E.W. Plummer, T.C. Caves, R.P. Messmer and W.R. Salaneck, Phys. Rev. Lett. **51**, 1378 (1983).

71. C.Y. Ng, P.W. Tiedemann, B.H. Mahan and Y.T. Lee, J. Chem. Phys. **66**, 3985 (1977).

72. J.L. Dehmer and Dan Dill, J. Chem. Phys. **65**, 5327 (1977).

73. Boon-Keng Teo and P.A. Lee, J. Am. Chem. Soc. **101**, 2815 (1979).

74. B.X. Yang, J. Kirz and T.K. Sham, Phys. Lett. **110A**, 301 (1985).

75. D.E. Cox, E.J. Samuelsen and K.H. Beckurts, Phys. Rev. B **7**, 3102 (1973).

76. G. Herzberg, *Spectra of Diatomic Molecules*, (Van Nostrand, Princeton, 1950), p.560.

77. H. Sambe and D.E. Ramaker, Chem. Phys. **104**, 331 (1986).

78. W. Eberhardt and E. W. Plummer, Phys. Rev. Lett. **47**, 1476 (1981).

79. K. Siegbahn *et al. ESCA Applied to Free Molecules*, (North-Holland, 1969).

80. W. Eberhardt, E.W. Plummer, C.T. Chen and W.K. Ford, Aust. J.Phys. **39**, 853 (1986).

81. D. Lapiano-Smith, K. Lee, C.I. Ma, K. Wu and D.M. Hanson, J. Electron Spectrosc. and Relat. Phenom. **51**, 221 (1990).

82. N. D. Lang and A. R. Williams, Phys. Rev. B **20**, 1369 (1979).

83. E. W. Plummer, W. R. Salaneck and J. S. Miller, Phys. Rev. B **18**, 1673 (1978).

84. G. Kaindl, T.C. Chiang, D.E. Eastman and F.J. Himpsel, Phys. Rev. Lett. **45**, 1808 (1980).

85. W.E. Moddeman, T.A. Carlson, M.O. Krause, B.P. Pullen, W.E. Bull, and G.K. Schweitzer, J. Chem. Phys. **55**, 2317 (1971).

86. W.E. Spicer, Appl. Phys. **12**, 115 (1979).

87. S.A. Lindgren and L. Wallden, Phys. Rev. B **22**, 5967 (1980).

88. G. Ebbinghaus, W. Braun, A. Simons and K. Berresheim, Phys. Rev. Lett. **37**, 1770 (1976).

89. M.L. Shek, J. Hurbek, T.K. Sham and G.-Q. Xu, Surf. Sci. **234**, 324 (1990).

90. Sheng-Jenn Yang and Clayton W. Bates, Appl. Phys. Lett. **36**, 675 (1980).

91. A. Simon, *Structure and Bonding*, Ser. **36**, (Springer, New York, 1979, p.81).

92. A. Simon, in *Crystal Structure and Chemical Bonding in Inorganic Chemistry*, (North-Holland, Amsterdam, 1975, p.47).

93. K. Prabhakaran, P. Pen and C.N. Rao, Surf. Sci. **177**. L971 (1986).

94. G. Ebbinghaus, Ph. D. Thesis, (1977).

95. M. Ayyoob and M.S. Hegde, Surf. Sci. **133**, 516 (1983).

96. M. Cardona and L. Ley, *Photoemission in Solid I*, (Springer-Verlag, Berlin),1978.

97. Atomic Data and Nuclear Data Table, **32**, 1 (1985).

98. W. Eberhardt, F.M. Hoffmann, R. dePaola, D. Heskett, I. Strathy, E.W. Plummer and H.R. Moser, Phys. Rev. Lett. **54**, 1856 (1985).

99. W.A. Hart and O.F. Beumel, in Comprehensive *Inorganic Chemistry, Vol. 1*, (Pergamon, Oxford, 1973) p. 331.

100. Myron Strongin, S.L. Qiu, J. Chen, C.L. Lin and E.M. McCarron, Phys. Rev. B **41**, 7238 (1990).

101. K.R. Zavadil and N.R. Armstrong, Surf. Sci. **230**, 47 (1990).

102. P. Hofmann, K. Horn, A.M. Bradshaw and K. Jacobi, Surf. Sci. **82**, L610 (1979).

103. Xiaohe Pan, S.L. Qiu, S. Raaen, M.I. Florit, M.L. Shek and Myron Strongin, Phys. Rev. B **35**, 3740 (1987).

104. J.C. Phillips, *Bonds and Bands in Semiconductors*, (Academic Press, 1973).

105. Audreyl L. Companion, *Chemical Bonding*, (McGraw-Hill Book Company, 2nd edition, 1979).

106. S.L. Qiu, X. Pan, Myron Strongin and P.H. Citrin, Phys. Rev. B **36**, 1292 (1987).

107. R.J. Smith, J. Anderson and G.J. Lapeyer, Phys. Rev. B **22**, 632 (1980).

108. J.W. Davenport, Chem. Phys. Lett. **77**, 45 (1981).

109. G. Blyholder, J. Phys. Chem. **68**, 2772 (1964); J. Vac. Sci. Technol. **11**, 865 (1974).

110. L.H. Little, *Infrared Spectra of Adsorbed Species*, (Academic, London, 1966).

111. F.M.F. de Groot, M. Grioni, J.C. Fuggle, J. Ghijsen, G.A. Sawatsky and H.Petersen, Phys. Rev. B **40**, 5715 (1989).

112. R.T. Poole, J.G. Jenkin, J. Liesegand and R.G.C. Leckey, Phys. Rev. B **11**, 5179 (1975).

113. D.A. Outka, J. Stöhr, W. Jark, P. Stevens, J. Solomon and R.J. Madix, Phys. Rev. B **35**, 4119 (1987).

114. M.P. Tosi, Solid State Phys. **16**, 1 (1964).

115. S.C. Abbahams and J. Kalnajs, Acta Cryst. **8**, 503 (1955).
F. Halverson, J. Phys. Chem. Solids, **23**, 207 (1962).